

FLUID DYNAMICS OF LITHIUM ION BATTERY VENTING FAILURES

by

FRANK AUSTIN MIER

Submitted in Partial Fulfillment
of the Requirements for the Degree of
Doctor of Philosophy in Mechanical Engineering
with Dissertation in Intelligent Energetic Systems



New Mexico Institute of Mining and Technology
Socorro, New Mexico
August, 2020

ABSTRACT

Lithium batteries have a well documented tendency to fail violently under abuse conditions which can result in venting of flammable and otherwise hazardous material. The 18650 format batteries of interest here have a perforated vent cap incorporated in the positive terminal which is designed to burst before full case rupture under pressure build up. Here, the fluid dynamics of vent-initiated failures is considered from pressure build up during thermal runaway to the subsequent pressure driven venting flow. The characterization of the failures leads to improved safety for identifying cell failures and the impact on the surrounding environment. Increasing the basic understanding of venting flows links internal battery hazards and the safety of the surrounding environment.

Battery case strain and temperature were measured on cells under thermal abuse which was used to calculate internal pressure via hoop and longitudinal stress relations. Strain measurement is a non-invasive approach with no impact on the chemical decomposition within batteries that leads to thermal runaway. The experimental methodology and test apparatus were developed and validated through predictable, representative test specimens of open cases and pressurized gas cylinders. Live battery experiments reliably captured the final pressure rise before venting onset. The pressure build up was observed to coincide with the beginning of thermal runaway.

Vented material leaves the battery cells as a complex multiphase, reactive flow. Experiments were performed to address droplet spray and interactions between nearby, steady gas jets representative of actual battery vents. Battery vents were pressurized until failure with carbon dioxide and sucrose solution to represent electrolyte. High speed schlieren imaging visualized the droplet spray and surrounding gas flow immediately after burst. The resulting droplet spray was found to vary in characteristics depending on the fluid dynamic properties of the liquid material. The resulting droplet flow spreads to angles wider than the gaseous portions of the jet and are projected into the atmosphere. Image processing methods were developed to extract droplet flow paths from the gas jets.

In the 18650 battery vent cap studied here, venting consists of four individual jets. Fundamental fluid dynamic experiments were developed to study the interaction between nearby gas jets, in a simplified geometry of two outwardly oriented gas jets issuing into a quiescent environment. Particle Image Velocimetry (PIV) measured the interaction between the jets which was quantified in terms of mean velocity and turbulence strength profiles. A semi-analytical model was developed to predict the combined jet velocity profiles and interactions. Jets of small offset angles and orifice spacings demonstrated greater interaction in the

combined flow field, and jets oriented outward at angles of more than 20° were observed to not interact. Results of the experiments identify the flow field created during vent failures which can be used to validate or enhance simulations of mixing during venting failures and the evolution of the potentially flammable environment created outside of the cell. The work presented here provides quantifications to the broad scenario of venting flows which assists the characterization of battery failures.

Keywords: Lithium ion battery; Safety; Venting failure; Internal pressure; Jet interaction

ACKNOWLEDGMENTS

I would like to thank research advisor Dr. Michael J. Hargather for his guidance and expertise throughout this and previous work. I am grateful for the research experiences I have had with the Shock and Gas Dynamics Laboratory since I joined the lab as an undergraduate student. The research in Dr. Hargather's lab from all students has been captivating, and I look forward to finishing my graduate studies here.

Funding from Dr. Summer Ferreira and Dr. Joshua Lamb at Sandia National Laboratories under PO 1989037, PO 1859922, and PO 1739875 has made this research possible over the past 4 years. Dr. Ferreira and Dr. Lamb have provided research guidance and collaboration on the experiments presented here. I appreciate the opportunity to collaborate and interact with everyone at Sandia and especially learning from Dr. Lamb about the battery abuse lab. Dr. Heather Barkholtz and Armando Fresquez have been instrumental in assisting the transfer of battery vent caps and state of charge established cells to New Mexico Tech which were used in these experiments.

My friends and lab mates have provided constant assistance from everyday tasks to operating the data acquisition system during the experiments presented here. James, Josh, Stewart, Jeff, Kyle W., Rudy, Cara, John, Raj, Kyle B., Sara, Calla, Veronica, Sivana, Sean, Dylan, Christian, and Simone, I am thankful for all of your help.

I am most grateful for the constant support of my parents, Frank and Naomi, and my sister, Mariah. My family has provided every opportunity possible and given me more support than I ever could have asked for, and I know that I am very fortunate to have them.

Julissa, you have been an incredible partner throughout this process. Your never ending patience and support has made an immeasurable difference to my progress. Thank you for always being here for me.

CONTENTS

LIST OF TABLES	vii
LIST OF FIGURES	viii
NOMENCLATURE	1
1. INTRODUCTION	5
1.1 Research motivation	5
1.2 Lithium ion battery technologies and abuse testing	6
1.3 Jet characteristics and multiphase droplet spray	10
1.4 Present research objectives	13
2. THEORY AND VALIDATION OF STRAIN-BASED INTERNAL PRESSURE MEASUREMENT	15
2.1 Theoretical basis of experiment	15
2.1.1 Thin walled method	15
2.1.2 Thick wall method	17
2.1.3 Comparison of the thin and thick wall methods	18
2.1.4 Considerations and anticipated limitations	20
2.2 Expected strain measurement range	21
2.3 Strain measurement corrections	22
2.4 Design of laboratory test setup	24
2.5 Heating rate calibration series	27
2.6 Uncertainty estimation for strain based pressure measurement	28
2.7 Validation experiments	30
2.7.1 Measurement of thermal response from 18650 battery case	30
2.7.2 Internal pressure rise from constant volume heating of a carbon dioxide cartridge	32

3. RESULTS FROM LIVE 18650 THERMAL ABUSE EXPERIMENTS IN THE INTERNAL PRESSURE MEASUREMENT CALORIMETER	37
3.1 Strain measurements from individual tests	40
3.2 Pressure build up versus time and temperature	43
3.3 Correlating pressure rise to self heating and thermal runaway . . .	44
4. SIMPLIFIED BATTERY VENTING MODEL FOR INFORMING FLOW BOUNDARY CONDITIONS	49
5. OPTICAL MEASUREMENT TECHNIQUES FOR TRANSIENT, MULTIPHASE VENTING FLOW	52
5.1 Principals of high speed schlieren and equipment used	52
5.2 Vent cap burst fixture with visualization capability	53
5.3 Sucrose solution as an electrolyte substitute	55
6. EXPERIMENTAL RESULTS AND DATA ANALYSIS OF SIMULATED VENTING EXPERIMENTS	57
7. PARTICLE IMAGE VELOCIMETRY (PIV) MEASUREMENT FOR STEADY MULTIPLE-JET VENTING FLOW	67
7.1 Steady state gas venting test apparatus	67
7.2 Modular orifice plate holder and series of two jet geometries	72
7.3 PIV imaging equipment and software	75
7.4 Stagnation pressure and temperature data acquisition	76
8. PREDICTING JET INTERACTION WITH A SEMI-ANALYTICAL MEAN VELOCITY FIELD MODEL	79
8.1 The single jet mean flow field	79
8.2 Particle Image Velocimetry (PIV) results from a single jet to inform scenario-specific model constants	81
8.3 Combining multiple single jet profiles to predict multiple jet flow .	82
8.4 Describing metrics to characterize the intensity of jet interaction in the mean velocity field	86
8.5 Outwardly oriented gas jet interaction predictions for fabricated orifice plates	89

9. EXPERIMENTAL RESULTS AND DATA ANALYSIS OF STEADY STATE TWO JET VELOCITY FIELDS	92
9.1 Steady state PIV test series	92
9.2 Mean velocity field measurements	95
9.2.1 Centerline velocity changes in the axial direction	102
9.2.2 Tracking local peak velocity in the mean flow field	107
9.3 Turbulence strength observations	109
9.4 Estimated mass flow entrainment from experimentally observed flow fields	114
9.4.1 Estimating three-dimensional flow field from two-dimensional PIV data	114
9.4.2 Mass flow entrainment observations for pairs of outwardly angled jet pairs	117
10. CONCLUSIONS	120
10.1 General remarks on non-invasive pressure monitoring and the subsequent venting dynamics	120
10.2 Findings specific to lithium ion battery safety	122
10.3 Future work	122
BIBLIOGRAPHY	124

LIST OF TABLES

2.1	Approximate tool steel properties used in battery case construction	21
2.2	Thermal output coefficients for Vishay WK-06-120WT-350 strain gauges	23
2.3	Volume (V) and mass (m) measurements of Crossman brand carbon dioxide cartridges to calculate carbon dioxide density (ρ) . . .	33
3.1	Indicated burst vent burst pressure	43
3.2	Battery surface temperature at venting onset	44
5.1	Properties of ethylene carbonate electrolyte and sucrose solutions .	55
7.1	Two jet orifice plate configurations	74
8.1	Experimentally determined constants used in Equation 8.1 [1] . . .	80
9.1	Exit velocities for PIV trials calculated from stagnation property measurements	93

LIST OF FIGURES

1.1	Schematic representation of the components in an 18650 format battery.	7
1.2	(a) Axial and (b) side view schlieren images of a LG MG1 (NMC) battery venting after being heated with two cartridge heaters placed adjacent to the outer battery case. These heaters were electrically powered at a rate of 75 W.	10
1.3	Schematic representation of an 18650 cell and the approximate location of the four radially grouped jets issuing from the vent cap as based in the locations of vent cap openings. Intact and open images show where the burst disk lifts allowing venting to occur. .	11
2.1	A schematic representing the arrangement of two stacked strain gauges mounted to a pressurized cylinder for measurement of hoop and longitudinal strain. The specific example of a cylindrical battery is presented.	16
2.2	The ratio of respective stress components calculated via thick and thin wall methods as a function of the ratio of case thickness to outer diameter.	20
2.3	Images of the test setup installed at New Mexico Tech including (a) the test chamber, (b) instrumentation end cap, (c) insulation structure, and (d) battery holder.	25
2.4	Micro-Measurements brand, model WK-06-120WT-350 strain gauges. Two strain gauges are incorporated into a single unit and are arranged at right angles to allow simultaneous measurement in the hoop and longitudinal directions.	27
2.5	(a) Gas temperature increase versus time and linear fits for the heating rate calibration test series, and (b) plotting the nominal heating rate versus electrical power input for these tests.	28
2.6	Open 18650 size battery case with strain gauge and data acquisition wiring attached.	31
2.7	Raw and corrected strain measurement values versus temperature for the first open battery case thermal expansion validation trial . .	32
2.8	Raw and corrected strain measurement values versus temperature for the second open battery case thermal expansion validation trial	33

2.9	Indicated pressure as a function of temperature for the open case validation trials	34
2.10	Internal pressure versus temperature for carbon dioxide with a constant density of 840 kg/m ³	35
2.11	Carbon dioxide cartridge with strain gauge mounted (a) before testing and (b-c) after burst from two perspectives.	35
2.12	Pressure versus temperature for pressurized and pierced carbon dioxide cartridges heated until failure or test fixture temperature limits.	36
3.1	Images of an 18650 battery (a) before abuse testing with strain gauge and electrical connections bonded to the surface and (b) the same cell after testing.	38
3.2	Battery surface temperature and test chamber pressure throughout the four live battery tests.	39
3.3	Hoop and longitudinal strain measurements and the corresponding indicated internal pressure for the first 4.8°C/min trial.	40
3.4	Hoop and longitudinal strain measurements and the corresponding indicated internal pressure for the repeated 4.8°C/min trial.	41
3.5	Hoop and longitudinal strain measurements and the corresponding indicated internal pressure for the 3.6°C/min trial.	41
3.6	Hoop and longitudinal strain measurements and the corresponding indicated internal pressure for the 2.4°C/min trial.	42
3.7	Comparing indicated internal battery pressure versus time between the four trials.	44
3.8	Comparing indicated internal battery pressure versus temperature between the four trials.	45
3.9	Battery surface temperature heating rate versus time. The beginning of self heating is annotated with colored stars.	46
3.10	The second time derivative of battery surface temperature versus time indicating the concavity of the surface temperature curve and allowing inference of the beginning of self heating which is annotated with colored stars.	47
3.11	Indicated internal pressure curves with the beginning of self heating indicated with colored stars. Pressure traces have been vertically shifted so the self heating onset moment lies at zero internal gauge pressure to demonstrate the comparable magnitude of the final pressure build up between all trials.	48
4.1	Battery internal pressure versus time after burst showing the regions in which the current vent burst and steady state PIV experiments are applicable.	51

5.1	(a) A schematic representation of the schlieren setup used, and (b) a representative image of the schlieren images recorded of simulated battery venting.	53
5.2	(a) The burst fixture installed in the laboratory, and (b) a schematic of the setup showing the construction of the vent holder and the field of view.	54
5.3	High speed schlieren images of (a) a NMC chemistry 18650 battery venting under thermal abuse, (b) atomization of 26% sucrose solution, and (c) wind-induced breakup of the 69% sucrose solution. The live cell failure image was taken 2,800 μ s after venting onset while the two simulated burst images were recorded 2,792 μ s after onset.	56
6.1	Schematic cross section showing the location of the sucrose solution within vent burst test apparatus prior to venting onset.	58
6.2	High speed schlieren images from gas-only burst trial showing the initial jet propagation into the environment.	58
6.3	High speed schlieren images from all three trials.	60
6.4	Liquid detection image processing steps including (a) raw steady-state schlieren images, (b) mean steady gas venting, (c) multiphase venting image with mean schlieren subtracted, and (d) liquid portions of the flow determined by thresholding (c) and highlighting in red. The raw droplet spray image processed in parts (c) and (d) is the low viscosity, $t = 5.0$ ms frame shown in Figure 6.3.	61
6.5	(a) Single high speed image of the flow identifying axial and radial locations where streak images are created, and (b) a radial streak image created from the column at $L_c = 10$	62
6.6	Streak images showing 12 ms of venting after burst for all three scenarios showing how the flow field evolves in the radial direction at distances of $2L_c$, $10L_c$, and $18L_c$	63
6.7	Droplet spray cone angle (θ_L) versus time for both high and low viscosity trials.	65
6.8	Flow front tracking image processing methodology.	65
6.9	Flow front propagation through time for three burst scenarios.	66
6.10	Time-of-arrival maps depicting when venting flow was first noted at a given location near the vent cap.	66
7.1	Annotated image of laboratory setup for steady state PIV measurement of venting flow.	68
7.2	Flow rate requirements for steady state venting as a function of normalized stagnation pressure.	69

7.3	Stagnation pressure versus time from the experiment measuring the steady state gas venting. After $t = 0$ the flow was steady.	70
7.4	(a) Acrylic PIV enclosure installed in the laboratory, and (b) model of the enclosure showing anticipated cones of venting flow (blue) and laser sheet (green).	72
7.5	Vent cap holder installed on steady state PIV test fixture.	73
7.6	Annotated images of (a) the orifice plate holder installed in the laboratory and (b) an orifice plate with two twist drills inserted into the plate's openings to show the jet spacing (D/a) and offset angle (θ).	74
7.7	A sample PIV image of two jets interacting with the computational region of interest showed as a white dashed line.	77
7.8	The National Instruments cDAQ 9188 installed in the laboratory.	78
8.1	(a) Streamwise velocity normalized by the local peak velocity as a function of the location parameter (η) as calculated from Equation 8.1, (b) local peak velocity decay downstream normalized by exit velocity as calculated with Equation 8.3, and (c) a schematic representation of geometry and specifically named velocities.	80
8.2	(a) Experimental velocity field PIV measurements for a single jet and (b) predicted velocity field for a single jet with optimized model constants.	82
8.3	A comparison of experimental versus predicted flow at various downstream distances.	83
8.4	Annotated two jet flow field schematic with coordinate systems and applicable velocities.	84
8.5	(a-c) Centerline velocity versus axial position in combined flow field at various spacings and angles.	88
8.6	Inward shift of peak velocity in combined flow field.	89
8.7	(a, c, e) Centerline to local peak velocity ratio versus axial position in combined flow field for various jet spacings and offset angles, and (b, d, f) local peak velocity location (solid lines) versus axial position compared to the streamwise axis trajectory (dashed lines) demonstrating inward peak shift and jet combination.	90
8.8	Jet interaction map depicting the location of first significant interaction and predicted jet combination region at various combinations of jet spacing and offset angle.	91
9.1	(a-d) Still frames recorded during a PIV trial which were processed to create (e, f) instantaneous velocity fields.	94

9.2	Contour plot comparison between (a and c) experimentally recorded and (b and d) predicted mean velocity fields for jets with an orifice spacing or $D/a = 3$ and offset angles of 0° and 10°	96
9.3	Contour plot comparison between (a and c) experimentally recorded and (b and d) predicted mean velocity fields for jets with an orifice spacing or $D/a = 3$ and offset angles of 20° and 30°	97
9.4	Contour plot comparison between (a and c) experimentally recorded and (b and d) predicted mean velocity fields for jets with an orifice spacing or $D/a = 6$ and offset angles of 0° and 10°	98
9.5	Contour plot comparison between (a and c) experimentally recorded and (b and d) predicted mean velocity fields for jets with an orifice spacing or $D/a = 6$ and offset angles of 20° and 30°	99
9.6	Contour plot comparison between (a, c, e, g) experimentally recorded and (b, d, f, h) predicted mean velocity fields for jets with an orifice spacing or $D/a = 12$ and offset angles of 0° , 10° , and 20°	100
9.7	Local mean axial velocity uncertainty contour for the $D/a = 6$, $\theta = 0^\circ$ trial which has the largest uncertainty value observed here.	102
9.8	Axial velocity profile comparison between PIV measurements and model predictions at various axial locations for jets with orifice spacing of $D/a = 3$	103
9.9	Axial velocity profile comparison between PIV measurements and model predictions at various axial locations for jets with orifice spacing of $D/a = 6$	104
9.10	Axial velocity profile comparison between PIV measurements and model predictions at various axial locations for jets with orifice spacing of $D/a = 12$	105
9.11	Measured and predicted centerline to local peak velocity ratio progression for spacings of (a) $D/a = 3$, (b) $D/a = 6$, and (c) $D/a = 12$.	106
9.12	Measured and predicted local peak velocity location progression for spacings of (a) $D/a = 3$, (b) $D/a = 6$, and (c) $D/a = 12$	108
9.13	(a, c, e, g) Turbulence strength contours and (b, d, f, h) profiles for PIV trials with orifice spacing of $D/a = 3$	111
9.14	(a, c, e, g) Turbulence strength contours and (b, d, f, h) profiles for PIV trials with orifice spacing of $D/a = 6$	112
9.15	(a, c, e) Turbulence strength contours and (b, d, f) profiles for PIV trials with orifice spacing of $D/a = 12$	113
9.16	Comparing predicted mass flow rate from the single jet velocity field model to approximations based on the measured PIV velocity field.	115

9.17	(a) Schematic representation demonstrating how two dimensional PIV data is used to reconstruct and approximate the full three dimensional flow field. (b) Velocity is approximated in the yz -plane at each axial (x/a) location using using PIV data at $z = 0$ in the plane and a (c) jet profile to approximate the velocity field variation in the z -direction	116
9.18	Mass flow rate versus axial position approximated from PIV measured velocity fields for the (a) $D/a = 3$ and (b) $D/a = 6$ test geometries. Mass flow rate is normalized by the flow rate at the jet orifices as determined from stagnation pressure and temperature. .	118
9.19	Mass flow rate versus axial position approximated from PIV measured velocity fields for the (a) $D/a = 3$ and (b) $D/a = 6$ test geometries. Mass flow rate is normalized by the flow rate at the $x/a = 10$ flow cross section to minimize vertical deviations between tests.	118

This thesis is accepted on behalf of the faculty of the Institute by the following committee:

Michael J. Hargather

Advisor

Summer R. Ferreira

Joshua Lamb

Tie Wei

Andrei Zagrai

I release this document to the New Mexico Institute of Mining and Technology.

Frank Austin Mier

August 13, 2020

NOMENCLATURE

List of symbols, subscripts, and modifiers

General symbols

Symbol	Description
m	Mass
P	Pressure
t	Time
T	Temperature
V	Volume
ρ	Density

Symbols specific to internal pressure measurement experiment

Symbol	Description
A	Thermal output correction polynomial constant
b	Case thickness
c	Circumference
d	Outer case diameter
E	Youngs Modulus
GF	Gauge factor
h	Thickness (for strain gauge application)
K_t	Transverse sensitivity
l	Case length
r	Case radius
R	Substrate radius of curvature
\mathbb{W}	Voltage
α	Thermal expansion coefficient
δ	Case shape factor
ϵ	Strain
ν	Poissons ratio
σ	Strain

ϕ Strain gauge rotation misalignment angle

Subscripts specific to internal pressure measurement experiment

Symbol	Description
<i>A</i>	Strain gauge adhesive
<i>B</i>	Strain gauge backing
<i>EX</i>	Excitation
<i>H</i>	Hoop direction, thin method
<i>H,t</i>	Hoop direction, thick method
<i>i</i>	Inner
<i>int</i>	Initial
<i>L</i>	Longitudinal direction, thin method
<i>L,t</i>	Longitudinal direction, thick method
<i>o</i>	Outer
<i>OUTPUT</i>	Strain gauge output
<i>t</i>	Thick method
<i>T/O</i>	Thermal output

Symbols specific to venting flow experiments

Symbol	Description
<i>a</i>	Orifice diameter
<i>A</i>	Jet velocity profile constant
<i>A_e</i>	Exit area
<i>B</i>	Velocity decay constant
<i>C</i>	Jet velocity profile constant
<i>C_d</i>	Discharge coefficient
<i>D</i>	Orifice spacing
<i>d_p</i>	Seeding particle diameter
<i>k</i>	Gladstone-Dale constant
<i>L</i>	Stokes number characteristic length
<i>L_c</i>	Droplet spray characteristic length
<i>M</i>	Mach number
<i>n</i>	Index of refraction
<i>N</i>	Number of frame pairs in data set
<i>n_{jets}</i>	Number of jets from vent cap
<i>R</i>	Gas constant

r	Spanwise coordinate
s	Streamwise coordinate
s_0	Virtual origin location
Stk	Stokes number
U	Axial exit velocity
u	Mean local axial velocity
u_j	Mean local streamwise velocity
\bar{U}_j	Streamwise exit velocity
U_u	Mean velocity uncertainty
u'	Turbulent velocity
$u(t)$	Instantaneous axial velocity
v	Mean local radial velocity
x	Axial coordinate
y	Radial coordinate
γ	Ratio of specific heats
θ	Jet offset angle
θ_L	Liquid droplet spray angle
μ	Dynamic viscosity
ρ_p	Seeding particle density
$\sigma_{u(t)}$	Instantaneous velocity standard deviation

Subscripts specific to venting flow experiments

Symbol	Description
0	Stagnation property
1	Referring to jet 1
2	Referring to jet 2
η	Jet location parameter
<i>atm</i>	Atmospheric
<i>c</i>	Flow centerline
<i>e</i>	Exit property
<i>j</i>	Jet centric coordinates
<i>out</i>	Out of control volume
<i>p</i>	Local peak
<i>rms</i>	Root-mean-square

Modifiers

Modifier of property x	Description
dx	Differential quantity
Δx	Finite change
\dot{x}	Time rate of change
$x(t)$	Instantaneous property value at time t
x'	Turbulent value (instantaneous value less mean value)

List of abbreviations

Abbreviation	Abbreviated text
BMS	Battery management system
CID	Current interrupt device
CO ₂	Carbon dioxide
CT	Computer tomography
FTIR	Fourier Transform-Infrared Spectroscopy
LCO	Lithium cobalt oxide
LDA	Laser Doppler Anemometry
LFP	Lithium iron phosphate
MTI	Material Technology International Corporation
NCA	Nickel-cobalt-aluminum
Nd:YAG	neodymium-doped yttrium aluminum garnet
NI	National Instruments
NIST	National Institute of Standards and Technology
NMC	Nickel-manganese-cobalt
NPT	National pipe taper
PEEK	Polyether ether ketone
PIV	Particle Image Velocimetry
PTC	Positive temperature coefficient
PTV	Particle Tracking Velocimetry
SMD	Sauter Mean Diameter
SOC	State of charge
STP	Spray tip penetration
TSI	Thermo-Systems Engineering Co.
UNC	Unified National Coarse Thread

CHAPTER 1

INTRODUCTION

1.1 Research motivation

Energy storage in electrochemical batteries is integral to most systems in the modern world. Batteries are used on widely ranging scales from personal electronics and vehicles to large grid-scale applications. Worldwide lithium ion battery production for portable electronics and vehicles has been consistently increasing over time [2]. Gaining popularity, battery-based energy storage systems for power grid applications are generally tasked with duties such as resiliency, peak-shaving, frequency regulation, and arbitrage [3]. Similar to small scale battery use, total capacity of energy storage systems on the power grid in the United States has been increasing exponentially over recent years [4].

While lithium ion batteries have favorable performance characteristics in many applications, these cells have the tendency to fail violently under various abuse conditions which necessitates research into processes involved in these failures. Of the concerns surrounding the often explosion-like failure of lithium ion batteries, flammability of the vented material is of high importance. Examples of highly publicized battery fires include popular cellular telephones and onboard equipment of commercial aircraft [5, 6]. The persistent and ongoing need to mitigate the risks of lithium ion batteries is well documented in timelines of real-world failures, and the overall number of incidents is increasing as individual devices become more popular [7, 8]. Eventhough the size and application of batteries varies greatly, the unifying factor between failures is that the mechanism linking a fault within a cell to the safety of the surrounding environment is the fluid dynamics of the vented material.

While aspects of battery technology are multidiscipline in nature, characterizing the external fluid dynamics of individual cell failures can be systematically approached by describing the physics in three unique processes: internal pressure buildup from gas generation, vent mechanism burst, and external venting. Internal gas generation is driven by the breakdown of internal cell components which has been extensively studied with calorimetry experiments, but quantification of the internal pressure has not been achieved and would provide a novel ability to describe the chemical processes involved in thermal runaway as the reactions could be described as both functions of temperature and pressure. Buildup of internal pressure leads to vent burst which becomes the motive force

and a boundary condition of the subsequent transient venting flow. The internal state of the cell at the moment when the vent mechanism bursts is the initial condition, and certain measurable flow parameters of the battery vent provide the remaining information for a simple description of the flow [9]. The external fluid dynamics of the venting flow is further complicated by being multiphase, and commercial battery vents have a unique orifice design. As such, experimental measurements of battery venting are also necessary to fully describe the fluid dynamics. Of specific interest here is the 18650 format battery because it is the most widely used and produced size lithium ion battery [10].

1.2 Lithium ion battery technologies and abuse testing

Conditions which can lead to battery failures include overcharge, over-discharge, high temperature, low temperature, over-current, internal defects, mechanical loading (shock, crush, and penetration), and age [11]. Abuse conditions generally initiate a rise in temperature which drives exothermic reactions within the cell. If these reactions become self sustaining, the battery is said to be in thermal runaway [12]. Experiments have shown that the onset of thermal runaway generally occurs below 125 °C [13]. These conditions can become a safety concern when the failure is not able to be contained within the cell and a venting event occurs. The primary driver behind cell venting is the generation of gases internal to the cell. Oxygen gas is generated at the cathode of common cell chemistries including lithium-cobalt-oxide (LCO), nickel-cobalt-aluminum (NCA), and nickel-manganese-cobalt (NMC) [14]. Reactions within the electrolyte can lead to generation of hydrocarbons which are flammable and further increase pressure within the cell [12]. The combination of oxygen and hydrocarbons creates a scenario where combustion is possible regardless of the external atmosphere composition.

In typical lithium ion battery construction, an anode, cathode, and separator are tightly wound and placed inside the battery case along with a liquid electrolyte. As shown in Figure 1.1, the positive terminal of the cell is crimped in place at the end of the cell. Safety features located at this terminal include the burst disk and vent, positive temperature coefficient (PTC) element, and current interrupt device (CID) which is connected to the cathode via a foil tab [15]. The foil tab is connected to the vent cap at a perforated plate which generally has varied geometry based on the manufacturer of the cell. Aside from being referred to as a vent cap in this study, this assembly is sometimes called an "Anti-Explosive Cap" [16]. While designed with safety measures to combat the effects of abuse conditions, thermal runaway can still occur in some instances. If the pressure within the cell becomes too great, these vent caps are the components intended to fail in order to prevent complete case rupture or explosions. Vent caps have been tested separately from the battery to create a more controlled experiment [9].

Safety mechanisms are designed and fabricated into lithium ion batteries to mitigate the potential for catastrophic failures at the cell level. CIDs electrically

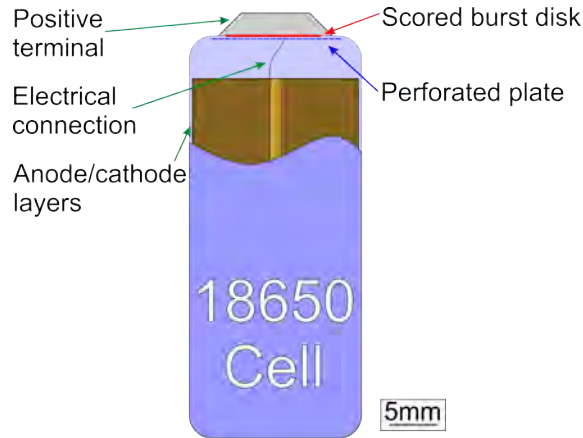


Figure 1.1: Schematic representation of the components in an 18650 format battery.

disconnect the electrochemical components of a battery from external circuitry if conditions within the cell present high venting failure risk [17]. Cylindrical batteries usually have a current interrupt device which physically breaks an electrical connection when significant pressure is applied to an internal diaphragm, rendering the battery permanently disconnected from external circuits [15]. PTC elements are components which increase in electrical resistance at elevated temperatures. Generally located at a terminal, a PTC can effectively prevent current flow into or out of a battery, and thus provides good protection from electrical abuse conditions. Similar to the PTC, thermal fuses can be used to permanently disconnect a battery from external circuits at elevated temperatures. The phenomena of separator shutdown, which is technically a material failure within the battery, can act as a passive safety element to protect against high internal cell temperatures. Separator shutdown blocks ion transport when the temperature becomes higher than the melting point of the polymer separator, causing it to melt and effectively stopping additional charging or discharge. However, if temperature continues to rise, large holes in the separator can form and lead to energetic failures as an internal short circuit is created [18].

General testing procedures have been created to provide abuse testing guidelines for lithium ion battery abuse testing under the United States Advanced Battery Consortium [19]. These guidelines provide comparison between cells, and a baseline for more specialized tests. Abuse testing addresses the potentially dangerous conditions batteries may be exposed to, but thermal and mechanical abuse are prevalent and uniquely difficult to prevent.

Thermal abuse occurs whenever a battery is exposed to temperatures outside of its specified operating range and is typically related to environmental conditions. Thermal abuse testing is performed when evaluating the thermal runaway process, chemical composition of vented material, or flammability risk of a given cell. The 18650 format cell is frequently used in laboratory scale calorime-

try where the relations between state of charge (SOC), calorimeter pressure, peak temperature, and test duration are compared. In general, experiments have shown increased calorimeter pressures, peak temperature, and decreased time before thermal runaway as SOC is increased [20]. Calorimetry experiments have been used to subject cells to extreme conditions with failure modes such as “jelly roll” ejection where the vent completely fails and the electrochemical components of the battery exit the case [21]. Cone calorimetry tests on LCO 18650 cells have been used for sampling of vented material throughout thermal abuse testing which showed increased concentrations of vented carbon monoxide and carbon dioxide for cells at higher initial SOC [22]. Imaging within cells during thermal abuse testing has been achieved by real time computer tomography (CT) scanning. When coupled with infrared imaging of the surface of an 18650 cell, the internal failure location was noted to correspond with a hot spot on the outside of the battery case [23].

Electrochemical components in battery are kept in very close proximity for maximized capacity and performance but are carefully separated to avoid internal short circuits which easily trigger thermal runaway. Battery cases are intended to keep these components safe, but mechanical abuse may overcome this protection. In mechanical abuse tests, initial failures are highly localized via an internal short within the battery. CT imaging has been used after testing on 18650 cells subjected to blunt rod and nail penetration tests to visualize internal shorts [24]. Mechanical abuse testing on larger cells has suggested that torsion is a weakness within cell construction beyond the traditional penetration tests [25].

The cell chemistry plays a large role in the relative safety and response of different cell to various abuse conditions. With the interest in developing safer cathode chemistries, lithium-iron-phosphate (LFP) cell chemistries have been extensively evaluated. LFP cells are more thermally stable than metal oxide chemistries and have a flatter discharge voltage curve, but they have a lower nominal voltage which is a challenge to accommodate in portable power applications [26]. In thermal abuse testing of LFP cells, there was less heat generation measured when compared to LCO [27]. Other thermal runaway experiments showed that like LCO and NMC cells, LFP battery venting contained hydrogen gas [28]. Lithium iron phosphate (LFP) cells have been tested at various SOC values where the venting of hydrocarbons was measured. In the presence of an ignition source, this vented material had a high likelihood of combusting [29]. In other experiments, thermal abuse tests on LFP have implemented Fourier Transform-Infrared Spectroscopy (FTIR) which measured potentially dangerous levels of hydrogen fluoride gas [30]. While LFP cells are generally considered more safe than metal oxide based batteries, there are still serious flammability risks involved. Some research has gone into moving towards a sodium based chemistry ($\text{Na}_x\text{FePO}_4\text{F}$) which has been demonstrated as cost effective and less hazardous than current chemistries [31].

Most applications of lithium batteries require multiple individual cells to be arranged into a larger pack based on voltage, current, and capacity demands. Experiments performed on battery packs have generally been similar to those performed on single cells. Examples include thermal abuse via fire testing which

led to venting and combustion of vented material [32]. Additional research has included chemical analysis of vented material via FTIR [33]. Experiments have also been performed to demonstrate the propagation of failure from one cell to others in a battery pack. These cascading battery failures occur as a cell in thermal runaway can be the source of thermal abuse to adjacent cells in the pack [34]. In these tests, cylindrical cells have shown reduced risk of failure propagation than pouch cells because of less efficient heat transfer between cells [35]. To mitigate risks in battery packs, recent research and development has focused on thermal management, evaluating air cooling, liquid cooling, and inclusion of a phase change material between cells [36, 37, 38].

Another key aspect of battery safety focuses on ensuring the safe operation of batteries by avoiding abuse conditions all together. Incorporated within battery powered systems, a battery management system (BMS) is generally tasked with preventing overcharge, overdischarge, and over temperature conditions [39]. Modern BMS also use various methods to quantify state-of-health (SOH) and SOC [40]. Under circumstances with high power demands, thermal management is key in allowing cells to operate efficiently, safely, and responsibly for the long-term preservation of battery performance [41]. These thermal management systems may incorporate basic lumped capacitance heat transfer models to ignore conduction within cells and focus on external convective cooling [42, 43]. However, increased accuracy may be achieved by considering the anisotropic thermal conductivity within cylindrical cells [44]. By considering the health of batteries while they are in use, steps can be taken to avoid hazardous conditions with the potential to lead to cell failures.

High-speed schlieren imaging was used to observe the external dynamics of lithium ion battery venting under thermal abuse and overcharge from multiple cell formats and chemistries as shown in Figure 1.2 [45]. Battery voltage, current, and case temperature were recorded simultaneously with high speed imaging. This previous work demonstrated the complex fluid dynamics of battery failures and provides the foundation for investigating external multiphase venting characteristics.

While extensive work has been performed on understanding and managing the relative risks of different cell chemistries and how broadly different battery pack configurations respond to abuse, a detailed analysis of how individual features in the construction of the ubiquitous 18650 format battery relate to battery failure characteristics has not yet been performed. Constraints have been applied when analyzing battery venting including a stated burst pressure of 3,448 kPa [46]. However, more recent experimental work has measured burst pressures between 1,829 kPa and 2,364 kPa [9]. This has been further applied to model the venting process from 18650 cells using isentropic flow equations and an initially choked flow [47]. However, expanding the level to which venting parameters are quantified will assist the evaluation of battery failures regardless of abuse condition or cell chemistry.

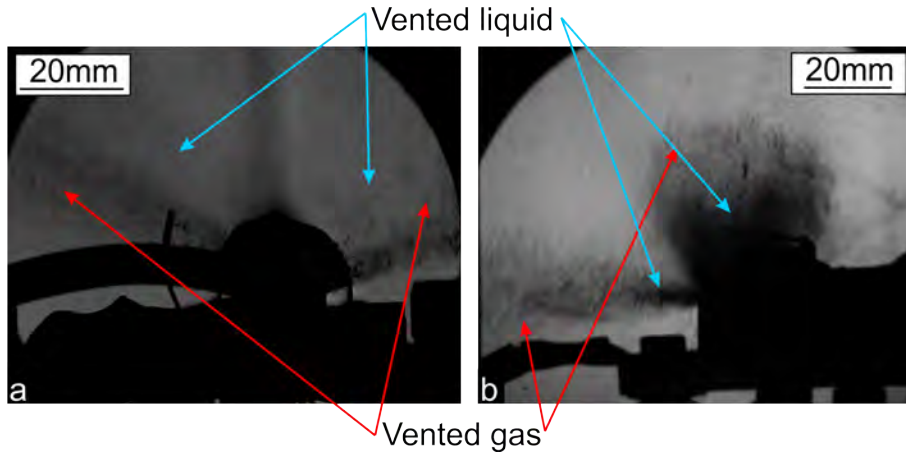


Figure 1.2: (a) Axial and (b) side view schlieren images of a LG MG1 (NMC) battery venting after being heated with two cartridge heaters placed adjacent to the outer battery case. These heaters were electrically powered at a rate of 75 W.

1.3 Jet characteristics and multiphase droplet spray

The venting flow from an 18650 format lithium ion battery should be governed by the vent geometry, internal pressure, and fluid properties. The vent on 18650 batteries is not a single opening, but rather four individual openings within the positive terminal. This results in the production of four radially arranged turbulent jets with roughly equal orifice shapes and sizes as shown in Figure 1.3. The jet phenomena may be first approximated as a simple, single-phase free shear flow entering a quiescent environment. A simple jet flow may be described within three distinct regions as the axial velocity profile evolves from a top-hat shape at the nozzle or orifice, to a transitional region with some remaining plateaued core velocity, and finally to a Gaussian distribution in the far field [48].

Identifying the outer boundary of a jet is important to understand propagation and mixing into the ambient environment. The spreading is generally conical with a given spreading angle measured as the half-angle of the cone. To establish the outer boundary of the jet, multiple early experimental studies demonstrated a linear expansion within a cone shaped jet with spreading angles ranging from 7° to 20° [49]. Tollmien provided an analytical solution based on the work by Prandtl which gave a spreading angle of 12° [50]. More recent experimental works implementing Particle Image Velocimetry (PIV) and Laser Doppler Anemometry (LDA) have demonstrated an ambiguity in determining the outermost boundary of the flow with demonstrated spreading angle differences for circular and annular jets [51].

By measuring the Gaussian velocity distribution in the far field, the evolution of the jet half width, the radius where local mean velocity is half the centerline velocity, may be used as a more consistent spreading metric. Spreading

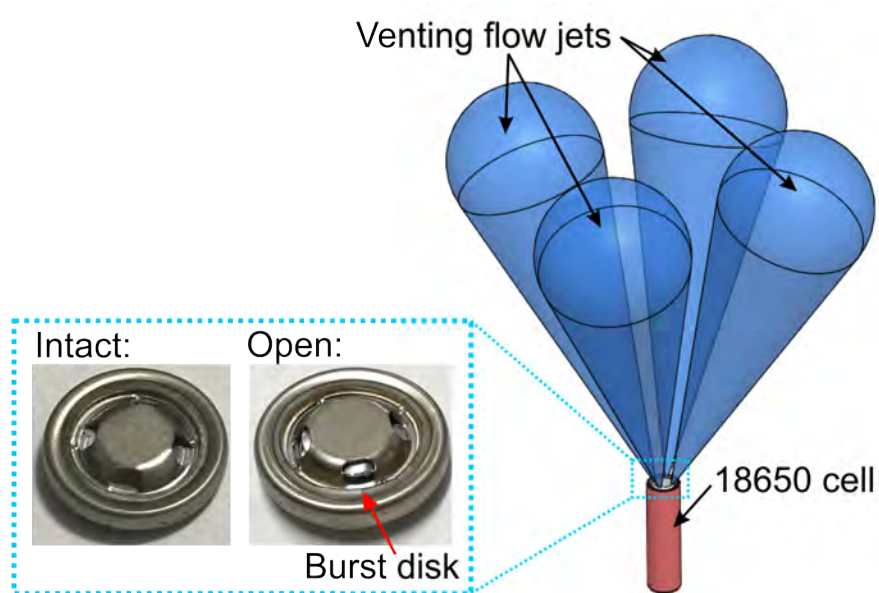


Figure 1.3: Schematic representation of an 18650 cell and the approximate location of the four radially grouped jets issuing from the vent cap as based in the locations of vent cap openings. Intact and open images show where the burst disk lifts allowing venting to occur.

rate at the jet half width as well as the centerline velocity decay constant are both consistent values regardless of the jet Reynolds number [52]. Commonly used values for the spreading rate and centerline decay constant are 0.102 and 5.9 respectively [1]. Additionally, experimental results have demonstrated that, like velocity profiles, pressure and root-mean-square turbulent velocity profiles are also self-similar [53]. Experimental and analytical conclusions on free shear jets from a simple nozzle are generally consistent with other flow configurations such as orifice plates and wall bounded jets with minor adjustment to spreading rate and velocity decay [54, 55]. Parallel rows of jets also show self-similarity with notably decreased velocity decay than single jets due to entrainment [56].

However, the multiphase nature of battery venting must not be ignored as liquid electrolyte spray occurs simultaneously with the gas jets. Liquid breakup in multiphase flow is generally driven by shear and rupturing instabilities characterized by Reynolds number, Weber number, and velocity differences between phases [57]. Further, droplet breakup may be divided into four distinct regimes: Rayleigh, first wind-induced, second-wind induced, and atomization where each respective regime has progressively smaller droplets when compared to the overall scale of the flow [58]. These regimes may also be characterized by comparing droplet breakup length to velocity. Within the Rayleigh regime, breakup length increases with velocity until a transition point where wind-induced breakup leads to shorter breakup lengths with further increases in velocity. Beyond the first

wind-induced regime, the second wind-induced regime shows breakup downstream or the orifice while atomization occurs at the orifice itself [59].

In the case of battery failures, previous work has visualized the high velocity flow resulting in droplet atomization [45], and the bulk geometry of such a spray is of importance. Within the atomization regime, spray angle is a function of fluid densities, nozzle or orifice geometry, and Taylor parameter which itself is a function of Reynolds and Weber numbers [60]. The geometric parameter for determining the spray angle shows some trends within similar designs, but generally is determined for each unique nozzle or orifice design [61]. The spray angle is not greatly affected by the gas momentum within the flow [62]. The velocity profile of droplets within a spray follows similar trends to that of a free shear jet, but increases in the droplet Stokes number have been demonstrated to increase the potential core velocity profile and significantly delay spreading [63].

Combustible spray systems pose additional challenges and parameters to be characterized. Characterization of relative performance between combustible sprays often relies on experimental characterization of spray tip penetration (STP), Sauter Mean Diameter (SMD), and mean velocity distributions [64]. High-speed schlieren imaging with digital image post-processing have effectively visualized droplet spray characteristics including STP, cone angle, and projected area [65].

Experimental measurement of the particle and velocity fields can be performed using various techniques, but PIV has become nearly an industry standard. This experimental method provides full field velocity measurements by correlating groups of particles between time-resolved image pairs and quantifying their displacement within the field of view [66]. Stokes number is used to describe whether a particle closely follows the surrounding flow and is defined as the ratio of the relaxation time of the particle to a characteristic timescale of the flow. In PIV applications, a Stokes number much smaller than unity is desired. Using the Stokes flow approximation, the relaxation time of the particle is a function of diameter, particle density, and surrounding fluid viscosity [67]. Depending on the flow conditions, illumination hardware, and camera specifications, various solid or liquid particles with different sizes and densities may be chosen for different PIV applications. Experimental work has determined the accuracy of tracing in terms of maximum relative slip velocity between the particle and flow as a function of Stokes number [68]. In general, it is desirable to have tracing particle diameters on the order of $1\ \mu\text{m}$ in turbulent and high speed flows, but porous or hollow particles with low density may also be used [69]. Oil droplets on this diameter scale have been successfully used for PIV measurement of the velocity profile of Mach 1.5 impinging jets within 1% of the velocity predicted by isentropic flow relations [70]. Other applications with high speed flows measured by PIV include flow over wings in supersonic wind tunnels and shock boundary layer interactions [71, 72]. The related technique of Particle Tracking Velocimetry (PTV) technique can be used in a similar way to PIV with more sparse particle seeding by tracking individual particles [73]. While seeding particles may be added to follow a transparent, gaseous flow, PIV can also be used to visualize droplets within a spray. In this way, PIV techniques are especially well suited for

characterization of lithium ion battery venting.

1.4 Present research objectives

This research is motivated to advance understanding of the battery venting process under abuse conditions by developing a new technique for pre-burst pressure measurement and characterizing the subsequent venting. The goal of the complementary experiments and predictive models developed here is to broadly describe the fluid dynamics and associated physical processes of venting flows issuing from a pressurized volume. Specifically this work will:

- Develop the theory for, and apply a non-invasive, strain based methodology to measure internal pressure changes within a sealed volume with compensation for thermal expansion.
- Provide velocity field and turbulence quantification for steady-state gas venting flow from multiple outwardly directed gas jets.
- Determine how the introduction of a liquid phase affects the velocity, flow front penetration, and spreading rate of transient venting flow of multiple interacting jets.
- Characterize the fundamental transient, multiphase fluid dynamics of the flow field created by multiple jets issuing from a finite volume, pressurized reservoir.

Although the applications described here are for a particular size of battery case, the research will develop a fundamental understanding of the failure dynamics of pressurized cylinders. The measurement methodology can be applied to any pressurized cylinder under thermal and pressure loading. The internal pressure measurement approach developed here allows for a non-invasive quantification of cell pressure under varying abuse conditions. This method will correlate case strain measurements in the hoop and longitudinal directions of the battery case to internal pressure with a compensation for thermal expansion. This will allow measurement of the internal pressure of a battery leading up to the onset of venting, which will also define the initial condition for the resulting venting flow.

A systematic approach will be implemented to experimentally quantify the venting process from 18650 format batteries. Experiments will simulate the venting flow under controlled conditions with different flow visualization techniques: high-speed schlieren imaging and PIV. Multiphase venting upon vent burst will be simulated to quantify spray tip penetration, jet projection angles, and droplet spray angle with an emphasis on differentiation between gas and liquid components of the flow. Gas venting under steady conditions will provide full-field velocity quantification, and interactions between outwardly projected

jets will be described in terms of parameterized spreading rates and velocity decay constants. Additional analysis of steady state venting will include turbulence statistics and description of jet interactions in the velocity fields. The fluid dynamic investigations here ultimately develop a fundamental understanding of how multiple transient turbulent jets interact and how multiphase flow alters the jet behavior and transient development.

Optical flow measurements provide a more thorough characterization of the fluid dynamics of a battery failure than previously attained. Primarily, a greater scientific knowledge of lithium ion battery safety will be developed as the physical mechanism contributing to their greatest hazards will be uniquely understood.

CHAPTER 2

THEORY AND VALIDATION OF STRAIN-BASED INTERNAL PRESSURE MEASUREMENT

Under abuse conditions, batteries exhibit a contained build up of pressure until the moment of vent mechanism burst. Pressure build up is the result of the thermal runaway process. The ability to measure this pressure rise is important to understand the onset of venting and the processes that lead up to it. Tightly wound, delicate electrochemical components within the cell make accessing the inside of the battery case for direct pressure measurement virtually impossible without damaging the battery or affecting how it responds to abuse. Here, measurement of the cylindrical case's mechanical response to the build up of internal pressure avoids these limitations. Experiments were performed to demonstrate how strain gauges may be used to perform noninvasive pressure measurement of batteries under thermal abuse conditions. Further, this experimental methodology may be applied to any pressurized cylinder.

2.1 Theoretical basis of experiment

Pressure contained within an enclosed cylinder will cause mechanical stress along its length and around its circumference in what are referred to as longitudinal and hoop components, respectively. To measure these stress components, two strain gauges are adhesively bonded to the outside of the cylinder wall. Each strain gauge has a resistive grid which is oriented in the direction of the stress component it measures as shown in Figure 2.1.

2.1.1 Thin walled method

Typical 18650 battery cases have a wall thickness that is much smaller than their diameter. Analysis of thin walled cylinders treats stress within a small finite region of the outer case of a cylindrical, pressurized vessel as two dimensional and planar with stress components around the circumference (hoop) and along the length (longitudinal) of the cylinder. For a thin walled cylinder, analytic expressions relate hoop (σ_H) and longitudinal (σ_L) stress to the internal pressure (P) within the cell as described by:

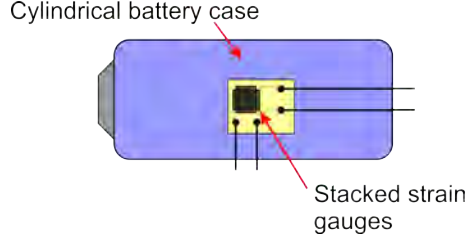


Figure 2.1: A schematic representing the arrangement of two stacked strain gauges mounted to a pressurized cylinder for measurement of hoop and longitudinal strain. The specific example of a cylindrical battery is presented.

$$\sigma_H = \frac{Pd}{2b} \quad (2.1)$$

$$\sigma_L = \frac{Pd}{4b} \quad (2.2)$$

These equations contain geometric constants for the cylindrical battery diameter (d) and case thickness (b). These two stress parameters are converted to strain via the Young's Modulus (E) for the given case material. Since perpendicular stress components (hoop and longitudinal stresses) are acting on the battery case, the Poisson effect must be considered. Hooke's Law considering two perpendicular, in-plane, stresses, may be used to predict the associated strains in the hoop (ϵ_H) and longitudinal (ϵ_L) directions:

$$\epsilon_H = \frac{\sigma_H}{E} - \frac{\nu\sigma_L}{E} \quad (2.3)$$

$$\epsilon_L = \frac{\sigma_L}{E} - \frac{\nu\sigma_H}{E} \quad (2.4)$$

where ν is Poisson's ratio and the case material is assumed to be isotropic. By measuring total strain of a battery case, the internal pressure is thus inferred.

Thermal expansion must be considered for the temperature ranges observed in thermal runaway events. The strain measured in experiments can be assumed to be the sum of the components due to changes in internal pressure and temperature [74]. Expansion along the length and circumference increases the longitudinal and hoop strain measurements respectively. Changes to the length (dl) and circumference (dc) to the battery case as a result of a finite temperature increase (dT) are both forms of linear thermal expansion as described by [75]:

$$dc = \alpha\pi d_{int}dT \quad (2.5)$$

$$dl = \alpha l_{int}dT \quad (2.6)$$

The subscript *int* denotes the initial battery length and diameter. The coefficient of thermal expansion (α) is a material property and assumed constant over the temperature changes expected. By noting that engineering strain (ϵ) is defined as the change in length to the original length of an object, Equations 2.5 and 2.6 may be rearranged to show that the component of case strain due to changes in temperature may be expressed as the product of the thermal expansion coefficient and the finite temperature change.

Summing the components of strain due to internal pressure and temperature increases gives [76]:

$$\epsilon_H = \frac{\sigma_H}{E} - \frac{\nu\sigma_L}{E} + \alpha dT \quad (2.7)$$

$$\epsilon_L = \frac{\sigma_L}{E} - \frac{\nu\sigma_H}{E} + \alpha dT \quad (2.8)$$

Equations 2.7 and 2.8 represent the measurements that would be recorded by strain gauges mounted to a battery in the hoop and longitudinal directions as it undergoes thermal abuse. These two equations may be subtracted from one another to eliminate the effects of thermal expansion giving:

$$\epsilon_H - \epsilon_L = \frac{1 + \nu}{E} (\sigma_H - \sigma_L) \quad (2.9)$$

Substituting the expressions for hoop and longitudinal stress from Equations 2.1 and 2.2 gives:

$$\epsilon_H - \epsilon_L = \frac{1 + \nu}{E} \left(\frac{Pd}{2b} - \frac{Pd}{4b} \right) \quad (2.10)$$

Solving the above equation for internal pressure gives:

$$P = \frac{4Eb}{d(1 + \nu)} (\epsilon_H - \epsilon_L) \quad (2.11)$$

This expression states that the internal pressure is proportional to the difference of the two strain measurements.

2.1.2 Thick wall method

As the assumption of a thin cylindrical shell becomes less applicable as wall thickness increases, additional analytical expressions exist for a thick wall scenario [77]. In particular, the hoop (subscript H, t) and longitudinal (subscript L, t) stress relationships for a thick wall on the outer surface are:

$$\sigma_{H,t} = \frac{2Pr_i^2}{r_o^2 - r_i^2} \quad (2.12)$$

$$\sigma_{L,t} = \frac{Pr_i^2}{r_o^2 - r_i^2} \quad (2.13)$$

where r_o and r_i are the outer and inner cylinder radii respectively. For clarity the geometric relationships $d = 2r_o$ and $b = r_o - r_i$ hold true, but expressing thick wall hoop and longitudinal stress in terms of diameter (d) and case thickness (b) in a manner similar to the thin wall equations is cumbersome.

Noting that the relationship in Equation 2.9 is determined from plane stress and linear thermal expansion relationships and not the thin wall method itself, a similar equation can be written by replacing σ_H and σ_L with $\sigma_{H,t}$ and $\sigma_{L,t}$ respectively:

$$\epsilon_{H,t} - \epsilon_{L,t} = \frac{1 + \nu}{E} (\sigma_{H,t} - \sigma_{L,t}) \quad (2.14)$$

Substituting Equations 2.12 and 2.13 into Equation 2.14 gives:

$$\epsilon_{H,t} - \epsilon_{L,t} = \frac{1 + \nu}{E} \left(\frac{2Pr_i^2}{r_o^2 - r_i^2} - \frac{Pr_i^2}{r_o^2 - r_i^2} \right) \quad (2.15)$$

which may be solved for a pressure relationship similar to Equation 2.11 for the thick wall method as:

$$P_t = \frac{E}{1 + \nu} \left(\frac{r_o^2 - r_i^2}{r_i^2} \right) (\epsilon_{H,t} - \epsilon_{L,t}) \quad (2.16)$$

where pressure (P_t for thick wall method) is again proportional to the difference in the strain measurements, but the coefficient has changed from the thin wall method.

2.1.3 Comparison of the thin and thick wall methods

It can be noted from Equations 2.1, 2.2, 2.12, and 2.13, that hoop stress is always twice the longitudinal stress within both analytical models. The only difference between the relationships is how the parameters related to cylinder geometry are treated. The cylinder geometry in the thin wall case affects strain components via the parameter:

$$\frac{d}{b} \quad (2.17)$$

whereas the geometry affects thick wall case stress via:

$$\frac{r_i^2}{r_o^2 - r_i^2} \quad (2.18)$$

Through substitution of the geometric relationships between radius (inner and outer), diameter, and thickness, it can be shown that:

$$\frac{r_i^2}{r_o^2 - r_i^2} = \frac{d}{b} \left(\frac{d^2/4 - db + b^2}{d^2 - db} \right) \quad (2.19)$$

Since the term within the parenthesis in Equation 2.19 defines the relationship between thin and thick wall stress relationships, this parameter may be called a relative shape factor and given the symbol δ . Accordingly:

$$\frac{r_i^2}{r_o^2 - r_i^2} = \frac{d}{b} (\delta) \quad (2.20)$$

with:

$$\delta = \frac{d^2/4 - db + b^2}{d^2 - db} \quad (2.21)$$

Using this relative shape factor, the hoop and longitudinal stress relationships for the thick wall method can be rewritten in terms of their respective components from the thin wall method as (by letting $P = P_t$):

$$\sigma_{H,t} = 2P \left(\frac{d}{b} \delta \right) = 4\delta \frac{Pd}{2b} = 4\delta \sigma_H \quad (2.22)$$

$$\sigma_{L,t} = P \left(\frac{d}{b} \delta \right) = 4\delta \frac{Pd}{4b} = 4\delta \sigma_L \quad (2.23)$$

In both of the above equations, the ratio of corresponding stress components from the two analysis methods is consistently 4δ . Symbolically:

$$\frac{\sigma_{H,t}}{\sigma_H} = \frac{\sigma_{L,t}}{\sigma_L} = 4\delta \quad (2.24)$$

Examining the shape factor δ at a case thickness of zero:

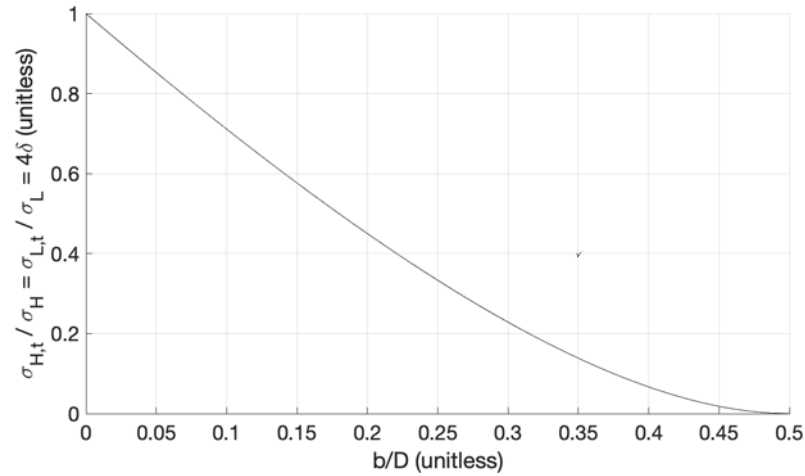


Figure 2.2: The ratio of respective stress components calculated via thick and thin wall methods as a function of the ratio of case thickness to outer diameter.

$$\frac{d^2/4 - d(0) + (0)^2}{d^2 - d(0)} = \frac{1}{4} \quad (2.25)$$

demonstrates that Equations 2.22 and 2.23 reduce to $\sigma_{H,t} = \sigma_H$ and $\sigma_{L,t} = \sigma_L$ respectively. Thus, the thick and thin wall stress methods are equivalent when case thickness is zero. As the case thickness increases towards $b/d = 0.5$, a solid cylinder, the ratio between thick method stress and thin method stress approaches zero as shown in Figure 2.2

For completeness, the ratio of internal pressures calculated from Equations 2.11 and 2.16 yields:

$$\frac{P_{\text{thin method}}}{P_{\text{thick method}}} = \frac{P}{P_t} = 4\delta \quad (2.26)$$

The thin wall method will thus underrepresent the internal pressure contained within a cylinder as the thickness increases. In most scenarios, including 18650 format batteries, the thin wall stress method is acceptable and results in a discrepancy of approximately 2%. Selection of thin versus thick method for individual tests is discussed further in Section 2.7.

2.1.4 Considerations and anticipated limitations

Values for cell diameter, case thickness, Poisson's Ratio, and Young's Modulus can be measured directly with material testing. However, these parameters

may be estimated if experimental strain data can be fixed to a known pressure state of the cell. This could be the battery state at the moment of venting onset where strain is expected to reach a maximum value which can be related to the expected burst pressure as reported in the literature [78]. Variability in this estimation between pressure and strain states would be influenced by the results of direct vent pressurization testing.

Limitations of this approach include localized failures within the cell. This could include deformations of interior battery components associated with events such as an internal short. Gas generation can also be localized within the cell prior to failure (e.g. trapped between anode and cathode layers), leading to nonuniform pressure distribution. To address this, initial tests were performed with multiple sets of strain gauges on a single cell.

Variable case thickness or other geometric irregularities leading to strain concentrations will have an effect on the accuracy of Equation 2.11. Hoop and longitudinal strain relations are derived for an even internal pressure. Thus, inconsistent internal pressure or the presence of other force loading on the cylindrical shell will decrease the accuracy of pressure calculations. To address this, initial tests will be performed with multiple sets of strain gauges on a single cell.

2.2 Expected strain measurement range

Using Equation 2.11 for internal pressure and Equations 2.7 and 2.8 for strain, approximations can be made to identify the range of strain measurements anticipated. This informed data acquisition techniques and equipment used. Previous work determined that 18650 format cells generally begin venting before an internal pressure of 3 MPa and temperature of 200 °C [9, 47, 13]. Battery cases are often constructed from tool steels such as A3 which has properties listed in Table 2.1 [16, 79, 80]. Typical empty battery cases sold as components have diameters of 18 mm with a thickness of 0.25 mm.

Table 2.1: Approximate tool steel properties used in battery case construction

Property	Symbol	Value
Young's Modulus	E	200 GPa
Poisson's Ratio	ν	0.285
Thermal expansion coefficient	α	$10.7 \cdot 10^{-6} \text{ 1/}^\circ\text{C}$

From Equation 2.9, hoop strain must always be larger than longitudinal strain. By substituting a pressure of 3 MPa and temperature of 200 °C into Equation 2.7, the maximum reasonable hoop strain measurement is 2,600 $\mu\epsilon$. At this same temperature and pressure, Equation 2.8 provides a maximum reasonable longitudinal strain measurement of 2,260 $\mu\epsilon$. For both of these strain measurements the portion of strain due to thermal loading is 2,140 $\mu\epsilon$.

For clarity, microstrain ($\mu\epsilon$) is used here to specify engineering strain (ϵ) without repeatedly noting multiplication by 10^{-6} . Engineering strain in the longitudinal direction (ϵ_L) is:

$$\epsilon_L = \frac{\Delta l}{l_{int}} \quad (2.27)$$

where Δl is elongation due to internal pressure build up and l_{int} original length. Similarly in the hoop direction, engineering strain is:

$$\epsilon_H = \frac{\Delta c}{c_{int}} = \frac{\Delta d}{d_{int}} \quad (2.28)$$

where c_{int} original circumference and Δc is the change in circumference after internal pressure has increased. Hoop strain is thought of as a change in circumference for consistency with the planar stress assumptions of the thin wall method, but hoop strain may also be considered in terms of original diameter (d_{int}) and diameter change (Δd).

2.3 Strain measurement corrections

While ideal strain gauges and experimental conditions would provide strain data which are immediately able to be used for internal pressure measurement, real limitations exist regarding thermal output, substrate curvature, transverse sensitivity, and gauge misalignment. To fully correct for these errors, the raw data is initially corrected for thermal output and the incremental thermal output associated with substrate curvature which occurs in the hoop direction. These two thermal outputs are mainly related to relative thermal expansion between the gauge and test specimen. This step is done initially because these errors are a function of the gauge and test specimen combination and are not affected by the experimental stress state. The second correction for transverse sensitivity removes any numerical dependence between the hoop and longitudinal strain values. Last, gauge misalignment is accounted for via a simple coordinate rotation.

Thermal output is caused by a relative thermal expansion mismatch between the strain gauge and the substrate along with electrical material property changes at elevated temperatures. While care was taken in selection of strain gauges to match the steel substrates used throughout testing, this factor cannot be eliminated entirely at the temperatures associated with battery abuse testing. As such, a thermal output correction function was used as provided by the manufacturer in the form: [81]

$$\epsilon_{T/O} = A_0 + A_1T + A_2T^2 + A_3T^3 + A_4T^4 + A_5T^5 \quad (2.29)$$

where A_0 through A_5 are constants provided with each gauge design and T is the temperature in degrees Celsius. For the strain gauges used in these experiments, the thermal output correction coefficients are listed in Table 2.2.

Table 2.2: Thermal output coefficients for Vishay WK-06-120WT-350 strain gauges

Coefficient	Value
A_0	$-4.63 \times 10^1 \mu\epsilon$
A_1	$2.38 \times 10^0 \mu\epsilon/^\circ\text{C}$
A_2	$-1.80 \times 10^{-2} \mu\epsilon/^\circ\text{C}^2$
A_3	$2.84 \times 10^{-5} \mu\epsilon/^\circ\text{C}^3$
A_4	$1.15 \times 10^{-7} \mu\epsilon/^\circ\text{C}^4$
A_5	$-3.70 \times 10^{-10} \mu\epsilon/^\circ\text{C}^5$

The thermal output ($\epsilon_{T/O}$) is given as a strain to be subtracted from the measured strain such that:

$$\epsilon_{\text{thermal corrected}} = \epsilon_{\text{measured}} - \epsilon_{T/O} \quad (2.30)$$

In the hoop direction specifically, the cylindrical substrate is sufficiently curved such that an additional thermal output correction is needed. This incremental thermal output ($\Delta\epsilon_{T/O}$) is calculated from the equation:

$$\Delta\epsilon_{T/O} = \frac{1}{R} [(1 + 2\nu_{A-B}) (h_A\alpha_A + h_B\alpha_B) - 2\nu_{A-B}\alpha_S (h_A + h_B)] \Delta T \quad (2.31)$$

where R is the radius of curvature of the substrate (here the radius of curvature of the battery case is used), ν_{A-B} is the average Poisson's ratio of the adhesive and backing, h_A is adhesive thickness, h_B is gauge backing thickness, α_A is the thermal expansion coefficient of the adhesive, α_B is the thermal expansion coefficient of the gauge backing, α_S is the thermal expansion coefficient of the substrate, and ΔT is the change in temperature from reference temperature [82]. All of these coefficients are provided by the strain gauge manufacturer [81].

In the configuration of interest here with perpendicular measurements of hoop and longitudinal strain, the thermal output corrected values are corrected for transverse sensitivity via Equations 2.32 and 2.33 [83]. Transverse sensitivity arises because foil grid style gauges (as used here) change resistance when strained in any direction. While the grid is designed to maximize sensitivity in the desired measurement axis, the electrical connections at the ends of these runs display small resistive changes under strain in the perpendicular direction. Of note, ν_0 is the substrate's Poisson's ratio, and K_t is the manufacturer provided transverse sensitivity factor.

$$\epsilon_{H, \text{ transverse, thermal corrected}} = \frac{(1 - \nu_0 K_t) (\epsilon_{H, \text{ thermal corrected}} - K_t \epsilon_{L, \text{ thermal corrected}})}{1 - K_t^2} \quad (2.32)$$

$$\epsilon_{L, \text{ transverse, thermal corrected}} = \frac{(1 - \nu_0 K_t) (\epsilon_{L, \text{ thermal corrected}} - K_t \epsilon_{H, \text{ thermal corrected}})}{1 - K_t^2} \quad (2.33)$$

The last correction performed is an in-plane rotation through angle θ to correct for any misalignment of the gauges which may occur during the bonding or adhesive curing phases of gauge mounting. The angle ϕ is measured after the gauge mounting process where the rotation is observed as a misalignment between alignment markings on the strain gauge and a burnished layout line along the length of the test specimen. The equations below are used to arrive at final corrected strain values from the transverse/thermal corrected strains:

$$\begin{aligned} \epsilon_{H, \text{ final}} &= \epsilon_{H, \text{ transverse, thermal corrected}} \cos^2 \phi \\ &+ \epsilon_{L, \text{ transverse, thermal corrected}} \sin^2 \phi + 2\tau_{HL} \sin \theta \cos \phi \end{aligned} \quad (2.34)$$

$$\begin{aligned} \epsilon_{L, \text{ final}} &= \epsilon_{L, \text{ transverse, thermal corrected}} \cos^2 \phi \\ &+ \epsilon_{H, \text{ transverse, thermal corrected}} \sin^2 \phi + 2\tau_{HL} \sin \phi \cos \phi \end{aligned} \quad (2.35)$$

where the shear term τ_{HL} is given by:

$$\tau_{HL} = \frac{1}{2} \tan(2\phi) (\epsilon_{H, \text{ transverse/thermal corrected}} - \epsilon_{L, \text{ transverse/thermal corrected}}) \quad (2.36)$$

2.4 Design of laboratory test setup

A test facility was designed and constructed to measure the external case strain of 18650 format batteries under thermal abuse conditions. The test setup consists of a heated cylindrical chamber with ports for instrumentation and a viewing window shown in Figure 2.3(a). A 4-NPT-size, Schedule 160, steel pipe section is used to create the body of the chamber, and standard pipe flanges are threaded to the ends to provide rigid mounting points for removable end caps. The chamber interior space is 87 mm in diameter by 305 mm long. End caps incorporate instrumentation pass-throughs on one side of the chamber and a battery

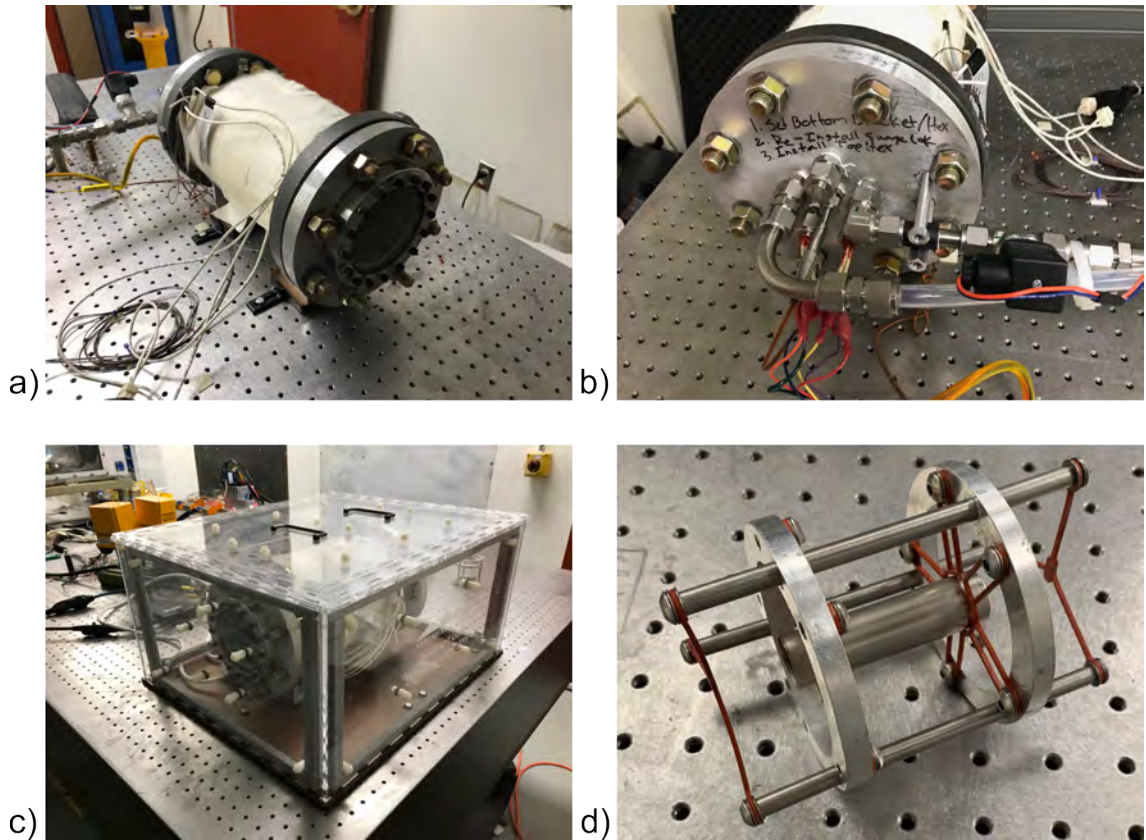


Figure 2.3: Images of the test setup installed at New Mexico Tech including (a) the test chamber, (b) instrumentation end cap, (c) insulation structure, and (d) battery holder.

viewing window on the other. Figure 2.3(b) shows the completed instrumentation end cap which has ports for a thermocouple probe to measure chamber gas temperature, three reconfigurable passthroughs for thermocouples and strain gauge leads, and an inlet and outlet for a remote purge system. Thermocouples are embedded into the main body of the test chamber to measure the temperature gradient within the steel, thus allowing calculation of heat flux into the chamber.

The chamber body is evenly wrapped with three electrical rope heaters (Hotwatt brand, model: GR30-120/960w120v/sf1-6) each capable of outputting 960 W (2,880 W total) to create even heating within the chamber interior. Achieving high heating rates in the chamber is important to be able to subject batteries to different abuse scenarios. A flexible insulation wrap made of fiberglass, ceramic fiber, and Nomex is placed around the test chamber body immediately outside of the rope heaters and secured with stainless steel pipe clamps. The test chamber itself is placed inside of a rigid insulation structure shown in Figure 2.3(c). This structure is fabricated from laser cut acrylic sheeting and has a modular design of double-pane panels. A final step taken in improving heat transfer to batteries

is the use of a helium environment inside the chamber. This improves heat transfer significantly as helium has a high thermal conductivity value of 0.142 W/mK compared to a value of 0.024 W/mK for air.

During an initial heating test there was an unpredicted cascading failure of the rope heaters at a chamber temperature of 275 °C. All subsequent tests were limited to a maximum chamber temperature of 225 °C while the heaters were on to provide a safety margin for the resiliency of the test apparatus.

A battery holder was designed and fabricated to securely hold a cell prior to and during venting within the center of the test chamber. Shown in Figure 2.3(d), the holder uses laser cut, high temperature silicone rubber cradles with a series of aluminum rings and standoffs. This holder fits within the inner diameter of the test chamber with minimal movement. The cradle shape of the silicone is designed to allow the battery to expand freely throughout testing and to not cause any stress concentrations which would negatively affect strain measurements. Two small silicone rubber rings are laser cut and placed on one side of the battery case adjacent to the two sides of a silicone holder to minimize movement during positioning. The strain these rings places near the end of the battery case are negligible.

Data acquisition is performed with a National Instruments (NI) cDAQ system and controlled through LabVIEW. The system is configured to record temperature, strain, and pressure data as well as control the operation of inlet and exit valves used for remote purge of the gas within the chamber after a test. Four J-type thermocouples are embedded in pairs on opposite sides of the chamber wall. Each pair has a thermocouple at a depth of 3.3 mm and 10.1 mm which correspond to roughly 25% and 75% of the wall thickness, respectively. K-type thermocouples are used to measure interior chamber gas temperature and surface temperature of the battery on the side of the case and on the positive terminal at the end of the vent cap. Chamber static pressure is also recorded and monitored throughout testing.

Micro-Measurements brand perpendicularly oriented, stacked strain gauges, shown in Figure 2.4, are bonded to the outer surface of the test specimens with a high temperature, two part epoxy which cures at room temperature (HBM brand, X280 adhesive). Mounted at 90° to each other, the stacked gauge configuration allows mounting over a single location on the cylinder. These gauges have a nominal gauge factor (GF) of 2.02. Each strain gauge is wired in a three-wire, quarter bridge configuration with 350 Ω resistors using RJ50 style circuit completion breakouts from a NI 9237 strain gauge measurement card. The quarter bridge arrangement provides adequate thermal compensation as hoop and longitudinal strain values are to be subtracted from each other as previously discussed. This measurement card has an input range of ± 25 mV/V in terms of the ratio of measurement voltage to excitation voltage with a 24-bit resolution. This corresponds to a measurement precision of $3.0 \cdot 10^{-6}$ mV/V. To complete the quarter bridge wiring configuration, solder pads are bonded to the test specimen surface similarly to the strain gauge. These solder pads provide a secure electrical connection and strain relief to prevent damage to gauges while being installed into the test

chamber.

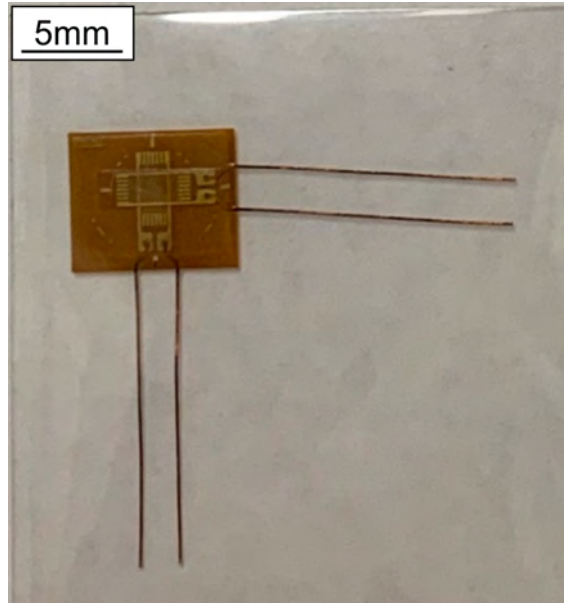


Figure 2.4: Micro-Measurements brand, model WK-06-120WT-350 strain gauges. Two strain gauges are incorporated into a single unit and are arranged at right angles to allow simultaneous measurement in the hoop and longitudinal directions.

The ratio of measurement voltage (V_{OUTPUT}) to excitation voltage (V_{EX}) for a quarter bridge configuration is [84]:

$$\frac{V_{OUTPUT}}{V_{EX}} = -\frac{GF \cdot \epsilon}{4} \left(\frac{1}{1 + GF \cdot \frac{\epsilon}{2}} \right) \quad (2.37)$$

With the previously calculated maximum anticipated strain values of $2,600 \mu\epsilon$ in the hoop direction and $2,260 \mu\epsilon$ in the longitudinal direction, the largest voltage ratio measurements will be -1.31 mV/V and -1.14 mV/V respectively. By substituting the precision of the voltage ratio measurement into Equation 2.37, the strain measurement precision is $5.9 \cdot 10^{-3} \mu\epsilon$.

2.5 Heating rate calibration series

A necessary step in the validation of the test setup was calibrating the system to have predictable interior heating rates as a function of the electrical power output of the heaters. Calibration tests were performed on the test chamber at electrical power values ranging from 576 W to 2,308 W by varying the input voltage to the electrical heaters with a variable autotransformer. Three tests

were conducted at power settings corresponding to 20%, 50%, and 80%. Each test heated the chamber for 60 min or until a chamber gas temperature measurement of 225 °C was reached. All tests started with zero gauge pressure and the chamber at room temperature. Temperature and pressure data were recorded throughout. Interior gas temperature increases and associated linear fits for this calibration testing are shown in Figure 2.5(a). Temperature increases were approximated as linear to provide a nominal heating rate useful in comparison to other calorimetry testing. Linear fits are calculated as regressions of chamber temperature from a time of 5 min to the end of the test. The nominal heating rates for the calibration tests follow a linear relationship with the heater setting as shown in Figure 2.5(b). Extrapolation of the data yields a maximum possible rate of 9.57 °C/min at the maximum heater setting of 2,880 W. However, tests were kept below this rate to minimize the risk of heater failures.

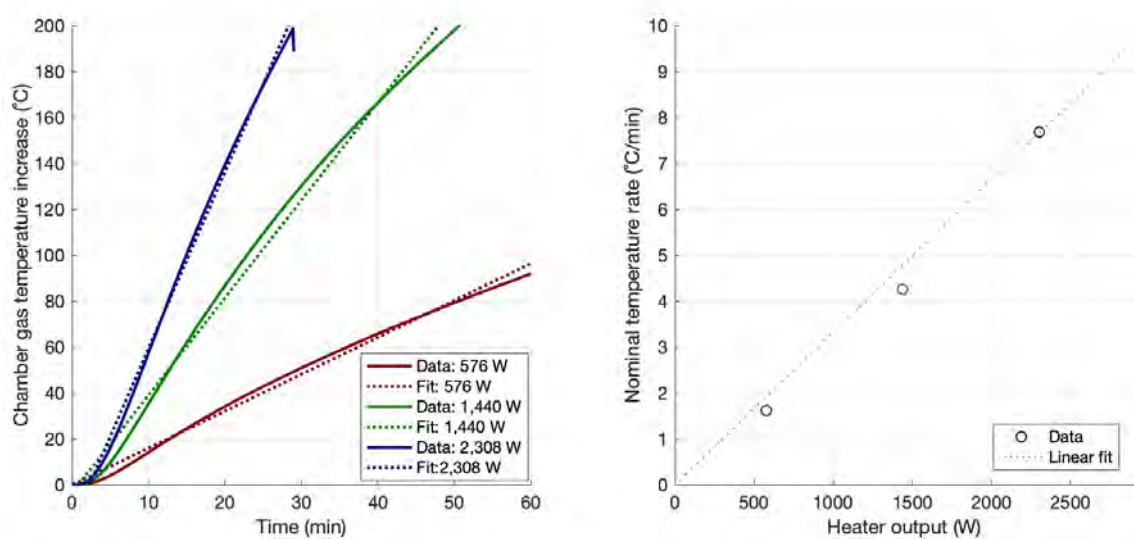


Figure 2.5: (a) Gas temperature increase versus time and linear fits for the heating rate calibration test series, and (b) plotting the nominal heating rate versus electrical power input for these tests.

2.6 Uncertainty estimation for strain based pressure measurement

Uncertainty propagation calculations were performed on the final internal pressure measurement equations developed for thin and thick wall cylinders to account for uncertainty in strain measurements, geometry, and material properties. Uncertainty for the thin and thick wall internal pressure measurements were respectively calculated as [85]:

$$\Delta P = \left(\left(\frac{\partial P}{\partial E} \Delta E \right)^2 + \left(\frac{\partial P}{\partial \nu} \Delta \nu \right)^2 + \left(\frac{\partial P}{\partial b} \Delta b \right)^2 + \left(\frac{\partial P}{\partial d} \Delta d \right)^2 + \left(\frac{\partial P}{\partial \epsilon_H} \Delta \epsilon_H \right)^2 + \left(\frac{\partial P}{\partial \epsilon_L} \Delta \epsilon_L \right)^2 \right)^{1/2} \quad (2.38)$$

and

$$\Delta P_t = \left(\left(\frac{\partial P_t}{\partial E} \Delta E \right)^2 + \left(\frac{\partial P_t}{\partial \nu} \Delta \nu \right)^2 + \left(\frac{\partial P_t}{\partial b} \Delta b \right)^2 + \left(\frac{\partial P_t}{\partial d} \Delta d \right)^2 + \left(\frac{\partial P_t}{\partial \epsilon_H} \Delta \epsilon_H \right)^2 + \left(\frac{\partial P_t}{\partial \epsilon_L} \Delta \epsilon_L \right)^2 \right)^{1/2} \quad (2.39)$$

where the partial differential terms are easily calculated from Equations 2.11 and 2.16. Since both strain measurements varied throughout each experiment, many of the partial differential terms varied accordingly, and uncertainty was calculated continuously throughout each experiment. In general, as strain measurements increased throughout experiments exhibiting a pressure build up, the uncertainty also increased.

Individual parameter uncertainty values in Equations 2.38 and 2.39 were approximated for each of the parameters used to calculate internal pressure uncertainty (ΔP or ΔP_t). Uncertainty in case thickness (b), diameter (d), outer radius (r_o), and inner radius (r_i) are all approximated to be equivalent to the 0.01 mm degree of measurement of the digital calipers used to perform these measurements. Strain measurement uncertainty in both directions was calculated as 2.8 $\mu\epsilon$. This value corresponds to twice the standard deviation of strain measurement noise bands recorded on static, unheated test samples. Material properties were not expected to vary significantly between similar samples in both validation and live cell tests, and were estimated at 5% for incorporation in uncertainty propagation. These uncertainty calculations were used to apply error bars on internal pressure measurement traces for both validation experiments and live battery abuse tests as reported in Figures 2.9, 2.12, and 3.8.

While material properties including Young's Modulus and Poisson's Ratio were not expected to vary significantly between similar samples, these properties demonstrated the largest potential source of systematic error in the measurements which is attributed to a lack of precise manufacturer specified properties. Thin steel specimens of various grades demonstrated variances of up to approximately 20% from typical, approximately 200 GPa Young's Modulus values [86]. Similarly, Poissons Ratio is approximated to vary up to 0.015 (unitless) [87]. These

variances from typical values were not included in this uncertainty approximation because they represented a systematic error causing a change in the slope of entire pressure trends rather than a continually varying, random uncertainty associated with the recorded measurements.

2.7 Validation experiments

2.7.1 Measurement of thermal response from 18650 battery case

Two validation experiments were conducted to demonstrate the strain based internal pressure measurement approach. The first experiment involved heating an empty 18650 battery case to demonstrate the thermal expansion component within the strain measurements. The empty 18650 battery case was purchased as an unassembled cell component and was simply a thin-walled cylinder with one end closed and the other end open. There were no electrochemical components installed, and there was no vent cap crimped into place. Since the cylinder was open, no pressure built up. As such, hoop and longitudinal strain measurements as described in Equations 2.7 and 2.8 reduce to the thermal expansion term. The hoop and longitudinal strain measurements were thus expected to be identical in this scenario.

The thermal expansion validation was performed at a heater power of 50% which corresponds to a nominal heating rate of $4.8^{\circ}\text{C}/\text{min}$ until a maximum surface temperature of 180°C was observed. The trial was run in duplicate to address repeatability. Shown in Figure 2.6, the strain gauge was mounted to the center of the battery case, and no de-lamination was noted during or after testing. Slight darkening of the epoxy adhesive and a hazing of the PEEK plastic insulation on the strain gauge lead wires were noted, but were not correlated to any lack in measurement performance.

Shown in Figures 2.7 and 2.8 hoop and longitudinal strain were measured throughout the heating process. The dashed lines represent the raw data as recorded in LabVIEW while the solid lines have been corrected for thermal, curvature, transverse sensitivity, and misalignment effects as described in Section 2.3. In both trials, the corrected values report strain values closer to zero than the raw data. While thermal output correction attempts to remove most erroneous measurement, strain typically increases with some notable non-linear trends throughout the heating of the battery case. Strain values in both trials, in hoop and longitudinal directions, show an initial linear increase in strain as temperature increases prior to a broad peak between 60°C and 100°C followed by subsequent fluctuations. Since hoop and longitudinal strain measurements follow somewhat similar, even if highly non-linear, trends, pressure measurements retain a degree of confidence because it is calculated from the more consistent difference between the two measured values.



Figure 2.6: Open 18650 size battery case with strain gauge and data acquisition wiring attached.

Both trials show trends on the same order of magnitude, but the measured thermal effects were greatest in the first trial (Figure 2.7). This is attributed to unknown residual stresses within the battery case which were a result of the cold-worked fabrication method of the steel. As metal was heated, there may have been some internal stress relief in the battery case which resulted in lower effects observed in the second thermal expansion trial which was performed with the same case. Another uncertainty which was systematically minimized in subsequent tests was the screw connections between the soldered in place strain gauge wires and the permanent data acquisition wires. Since these wires are connected via a screw connection, the compression of the crimped wire ferrules on the strain gauge leads may have a slightly variable contact resistance. This is further compounded with the compression of the ferrules potentially changing as differential thermal expansion may have occurred between dissimilar metals in the electrical junctions. In the second trial, the screw connections were tightened until the ferrules completely crushed and the screws were unable to be tightened further. This should provide more consistent contact resistance between tests.

The raw and corrected strain measurements from Figures 2.7 and 2.8 were used to calculate an indicated pressure in both open case trials. As shown in Figure 2.9, the data show a nonzero internal pressure. Since the case is open, this indicated pressure is clearly nonphysical and is presented to demonstrate an upper bound of the measurement uncertainty. Corrected strain values from both trials demonstrate a range of pressure uncertainty of approximately 400 kPa where the indicated pressure increases during the first trial and fluctuated around zero for the second. The open 18650 battery case trials demonstrate the ability to improve measurement uncertainty via the corrections described in Section 2.3, and provide a means to bound the certainty of measurements taken in live cell tests.

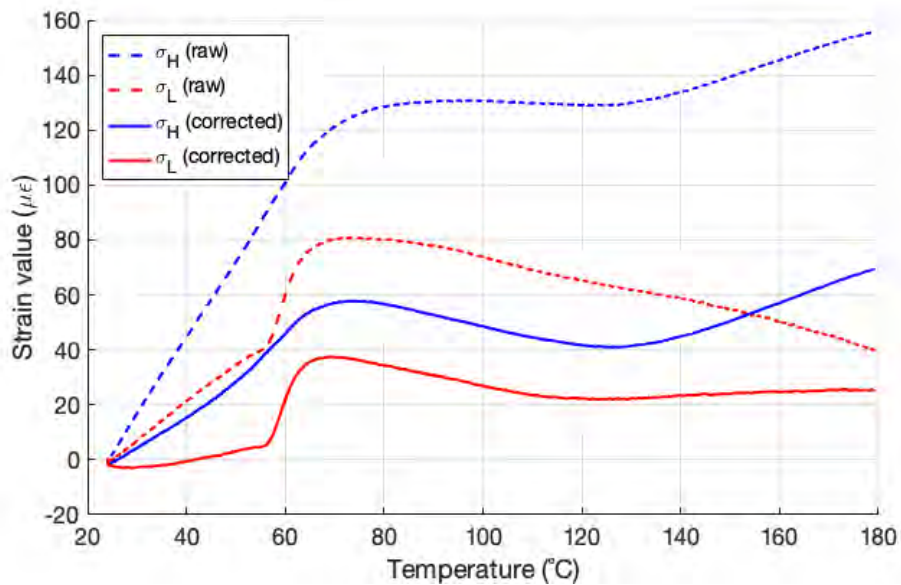


Figure 2.7: Raw and corrected strain measurement values versus temperature for the first open battery case thermal expansion validation trial

2.7.2 Internal pressure rise from constant volume heating of a carbon dioxide cartridge

A second more rigorous demonstration of the system capabilities was performed in which a carbon dioxide cartridge was heated until failure. These cartridges are small, pressurized cylinders containing nominally 12 g of carbon dioxide common in bicycle tire inflators and compressed gas pellet guns. The deformation of these cartridges is governed by the same hoop and longitudinal stress relations as a cylindrical battery. Under increased temperature, the pressure within the cartridge must increase predictably according to the Ideal Gas Law as plotted in Figure 2.10. The pressure increase as a function of temperature is calculated here as a constant volume heating from the National Institute of Standards and Technology (NIST) REFPROP database [88]. Throughout this process, the contained volume of carbon dioxide is at a constant density, because there is a fixed mass at fixed volume, which must be known to define the pressure-temperature curve.

In addition to the internal pressure measurement technique validation, this experiment is designed demonstrate the containment capability of the calorimeter fixture and cradle, as the carbon dioxide cartridge is likely to fail and vent at temperatures lower than the venting onset point for many 18650 format batteries.

Density within a Crossman brand carbon dioxide cartridge was calculated to an average value of 840 kg/m^3 . This was calculated by measuring the volume of the cartridges via water displacement then measuring mass before and after

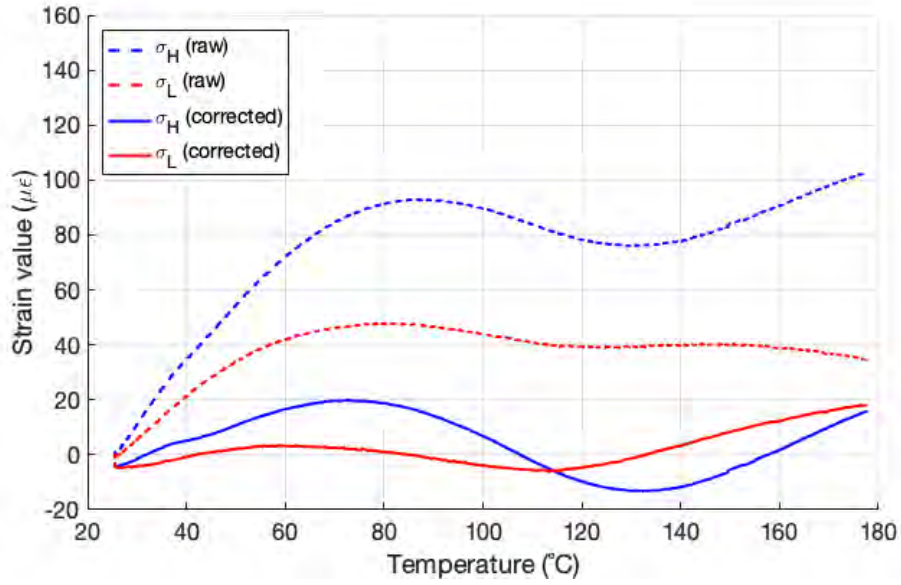


Figure 2.8: Raw and corrected strain measurement values versus temperature for the second open battery case thermal expansion validation trial

piercing the case and venting the carbon dioxide. Using a density of $7,860 \text{ kg/m}^3$, the volume of the steel case was calculated. The volume difference between the total cartridge and the steel case is the carbon dioxide volume, and the difference in the two mass measurements is the amount of carbon dioxide originally contained within the cartridge. Five samples were tested and are reported in Table 2.3.

Table 2.3: Volume (V) and mass (m) measurements of Crossman brand carbon dioxide cartridges to calculate carbon dioxide density (ρ)

Sample	Cartridge V (mL)	Cartridge m (g)	Steel case V (mL)	Steel case m (g)	CO ₂ V (mL)	CO ₂ m (g)	CO ₂ ρ (kg/m ³)
1	19.0	43.71	3.90	30.69	15.1	13.02	863
2	19.5	43.47	3.91	30.72	15.6	12.75	818
3	19.0	42.79	3.84	30.21	15.2	12.58	830
4	19.0	43.65	3.92	30.83	15.1	12.82	850
5	19.0	43.20	3.88	30.53	15.1	12.67	838
Mean	19.1	43.36	3.89	30.59	15.2	12.77	840

After determining the carbon dioxide density contained within one of the cartridges, strain gauges were bonded to four samples from the same production batch as shown in Figure 2.11(a). Three of the sample cartridges were tested as purchased while another was pierced at the reduced diameter end to relieve pres-

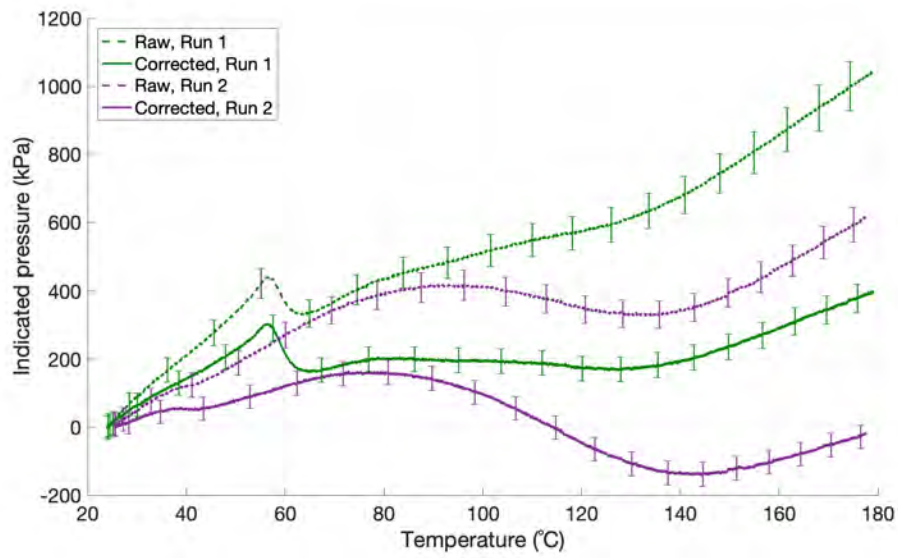


Figure 2.9: Indicated pressure as a function of temperature for the open case validation trials

sure and create an unpressurized baseline reference. Each cartridge was heated until failure or a surface temperature of 180°C at a rate of 4.8°C/min. Failure of the pressurized cartridges occurred at temperatures between 80°C and 100°C for all three full cartridges. The failures all manifested as longitudinal splits running along the length of the main cylindrical body of the sample as shown in Figure 2.11(b) and (c). These splits appeared to begin at the spherically domed end of the cartridge. During each failure, the strain gauge was torn and delaminated from the cartridge.

Internal pressure build up was then calculated for each of these four validation trials. The thick wall pressure equations were used because the case thickness (b) of 0.83 mm and outer diameter (d) of 18.6 mm would lead to the thin wall pressure calculation method underreporting the internal pressure by 13% as determined from Equation 2.26. Since the manufacturer of the cartridges did not disclose specific material composition or properties for the steel case, the same material properties listed in Table 2.1 which correspond to the battery case material were used. Since the strain measurements are only capable of capturing pressure build up from when they were mounted, each of the pressurized trials was fixed to the NIST database pressure value of CO₂ at 30°C. This also avoids complications due to initial erratic behavior as seen in the second pressurized cartridge trial associated with potential residual stresses in the cartridge walls. Figure 2.12 shows the measured internal pressure build up for each of the three pressurized cartridges, the unpressurized baseline, and the NIST reference data for a constant volume heating of carbon dioxide.

Throughout the majority of the heating process, both pierced and pressur-

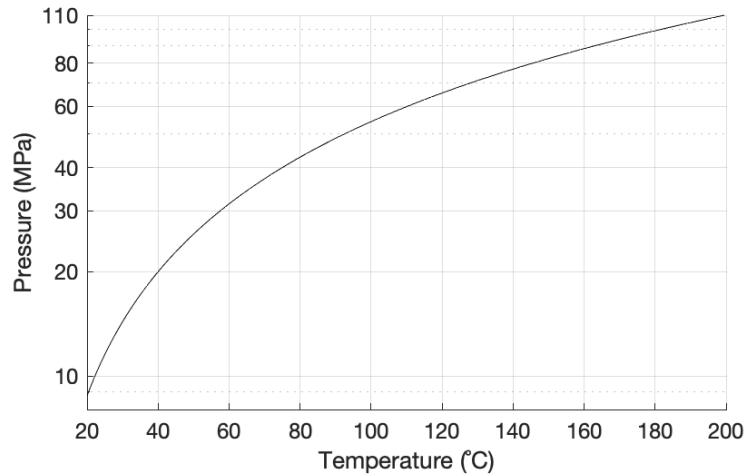


Figure 2.10: Internal pressure versus temperature for carbon dioxide with a constant density of 840 kg/m^3 .



Figure 2.11: Carbon dioxide cartridge with strain gauge mounted (a) before testing and (b-c) after burst from two perspectives.

ized carbon dioxide cartridges demonstrated pressure measurements similar to expectations. The pierced, and therefore unpressurized, cartridge showed no appreciable pressure response when compared to the pressurized samples. Aside from minimal initial transience on the second pressurized cartridge (green line in Figure 2.12), pressure increased nearly linearly with temperature as was predicted by the thermodynamics for a constant volume heating. On all three pressurized test specimens, the curves began to steadily curve upwards which is associated with the yielding of the steel cartridge prior to burst. Yielding behavior was not captured in the internal pressure estimation because the hoop and longitudinal stress model is built on an assumption of elastic material behavior. The measured pressure traces are ended between temperatures of 80°C and 100°C and correspond to the moment when the cartridge burst. The difference in slope between the reference data and the measured internal pressure traces was associated with the estimated values for Young's Modulus and Poisson's Ratio used because the exact material properties and composition of the steel alloy used for the carbon dioxide cartridge were not given by the manufacturer. These

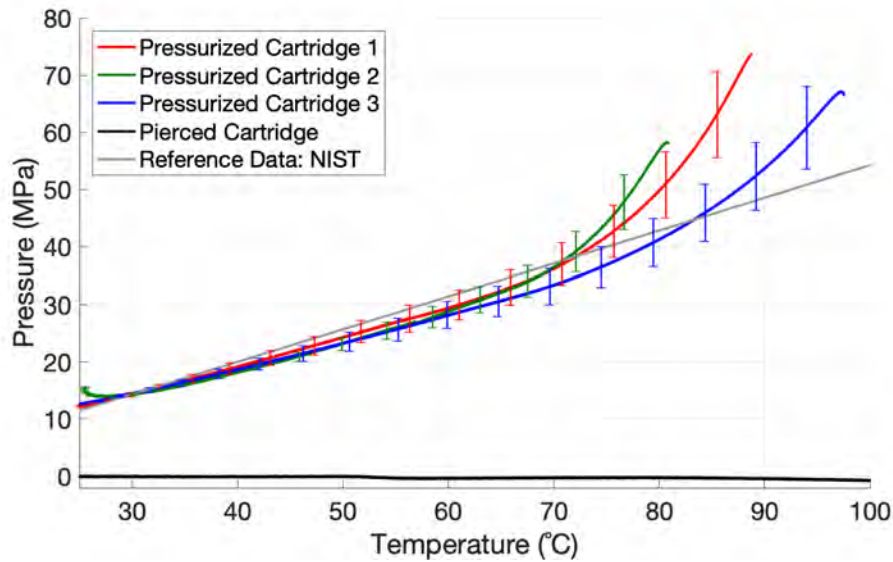


Figure 2.12: Pressure versus temperature for pressurized and pierced carbon dioxide cartridges heated until failure or test fixture temperature limits.

two material properties define a constant coefficient $E/(1 + \nu)$ which proportionally relates internal pressure to the strain measurements. Differences in this term caused a change in slope between the NIST reference and measured pressure traces. The majority of the material property uncertainty was attributed to the potential Young's Modulus variation which has been reported up to 20% for thin samples of steels of various grades [86]. The slope difference between predicted and measured pressure trends is smaller than this possible 20% variance in material property. In spite of this uncertainty, the general trends between internal pressure and temperature measurements compare well to what would be expected from a constant volume heating.

The carbon dioxide cartridge validation experiments were significantly less susceptible to measurement uncertainty than live battery tests. The previously described validation experiment with empty 18650 cases demonstrated an uncertainty band of approximately 0.4 MPa for an unpressurized specimen. In the compressed carbon dioxide cartridge validation, the material yielded at an internal pressure near 40 MPa, but live cells are expected to begin venting near 2 MPa. Given the much higher pressure responses from the carbon dioxide cartridge validation experiments, the results presented here represent a more ideal example of the capabilities of this measurement methodology.

CHAPTER 3

RESULTS FROM LIVE 18650 THERMAL ABUSE EXPERIMENTS IN THE INTERNAL PRESSURE MEASUREMENT CALORIMETER

Live battery abuse tests focused on determining the ability to implement the internal pressure measurement methodology during thermal abuse testing and quantitatively describing the trends of the internal pressure build up prior to venting onset. LG brand, model HE2 batteries were tested because the lithium cobalt oxide cathode chemistry has well documented and demonstrated venting failures under thermal abuse [13]. LG branded vent caps, generic across multiple cell chemistries, have an experimentally determined burst pressure of 1.906 MPa [9]. The known burst pressure is a reference to evaluate the accuracy of the strain-based internal pressure measurement. State of charge was established at 100% and confirmed prior to testing by collaborators at Sandia National Laboratories, and all cells tested were from the same manufacturing lot for consistency between trials. Measuring when and how gas generation occurred prior to venting onset provides a deeper understanding of how a battery fails under thermal abuse.

The same stacked strain gauges used in validation trials were bonded to the four live battery test samples using the same X280 room temperature curing epoxy adhesive along with solder pads for circuit protection and strain relief as shown in Figure 3.1(a). Trials were performed at nominal heating rates of 2.4°C/min, 3.6°C/min, and 4.8°C/min. The highest heating rate test, which was the same rate that validation experiments were performed at, was tested in duplicate. Tests began at room temperature and were performed until battery failure. Venting onset occurred between 138°C and 151°C for all four live cell tests, but the vents quickly became clogged and heating was applied until a second, much larger failure occurred. Strain data was unable to be recorded after the initial venting because the strain gauges, and particularly the soldered circuit completion joints, typically failed during the first venting event. Heating was applied until the second venting event to ensure that battery decomposition was as complete as possible to minimize the risk to test operators after the experiment. Batteries vented gas along with a significant amount of solid particulate likely associated with the second failure event which typically melted holes through the end of the cell opposite the vent mechanism. After each test, the strain gauge and electrical connections were completely delaminated from the battery surface, shown in Figure 3.1(b). Due to the destructive nature of these

tests, thermocouples and strain gauge wiring and terminal blocks were regularly replaced between tests.

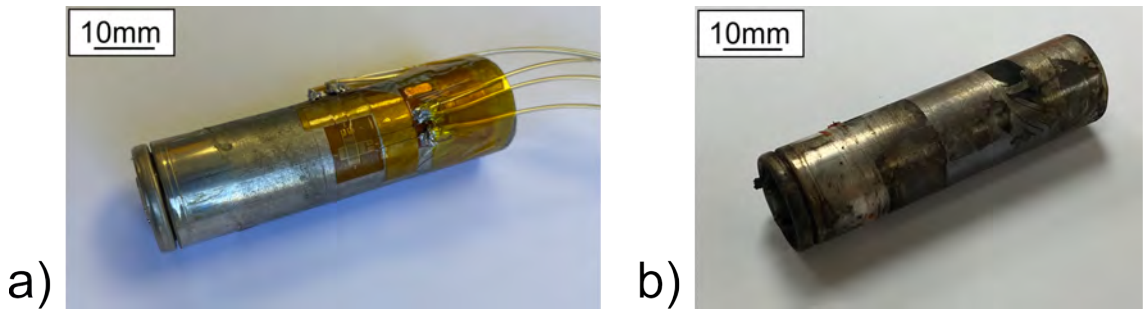


Figure 3.1: Images of an 18650 battery (a) before abuse testing with strain gauge and electrical connections bonded to the surface and (b) the same cell after testing.

Battery surface temperature and test chamber pressure were recorded throughout the individual live battery trials as shown in Figure 3.2 and provided useful information about how the experiments progressed towards a venting failure. Test chamber pressure provided information confirming when venting began. Venting onset is observed as the large, nearly instantaneous pressure jumps. Battery surface temperature was observed to rise roughly linearly after some initial transience as was the case in the validation trials. A short time before and after venting onset, the battery surface temperature began increasing at a higher rate which is associated with thermal runaway. The surface temperature and chamber pressure data compare well between the two repeated $4.8^{\circ}\text{C}/\text{min}$ trials. The test duration increases with lower heating rates while failure temperatures are similar between all trials.

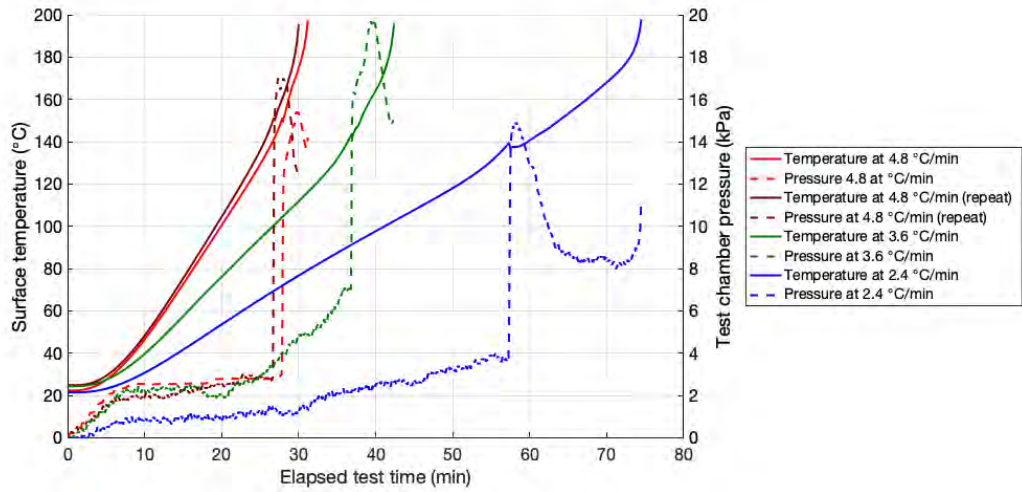


Figure 3.2: Battery surface temperature and test chamber pressure throughout the four live battery tests.

3.1 Strain measurements from individual tests

Hoop and longitudinal strain measurements were recorded during all four live battery thermal abuse tests. Shown in Figures 3.3 through 3.6 hoop and longitudinal strain values varied widely between individual trials and demonstrate some initial unpredictable behavior before an ultimate rise before failure. All data traces shown have a restricted domain to the moment venting was first noted via chamber pressure measurement. After first venting, the strain measurement tended to jump between the maximum and minimum of the potential measurement range as determined by the NI cDAQ measurement card. This is indicative of failing electrical connections in the strain gauge circuit completion which would coincide with strain gauge delimitation as was observed after all four live battery tests. Reported internal pressure values were calculated via the thin wall method given the 0.12 mm measured case thickness of the LG brand batteries and the outer diameter of 18.0 mm.

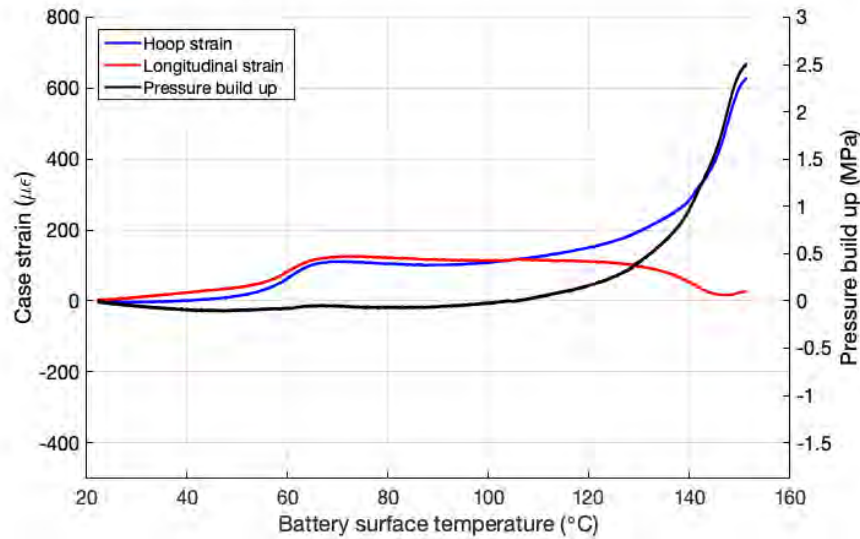


Figure 3.3: Hoop and longitudinal strain measurements and the corresponding indicated internal pressure for the first 4.8°C/min trial.

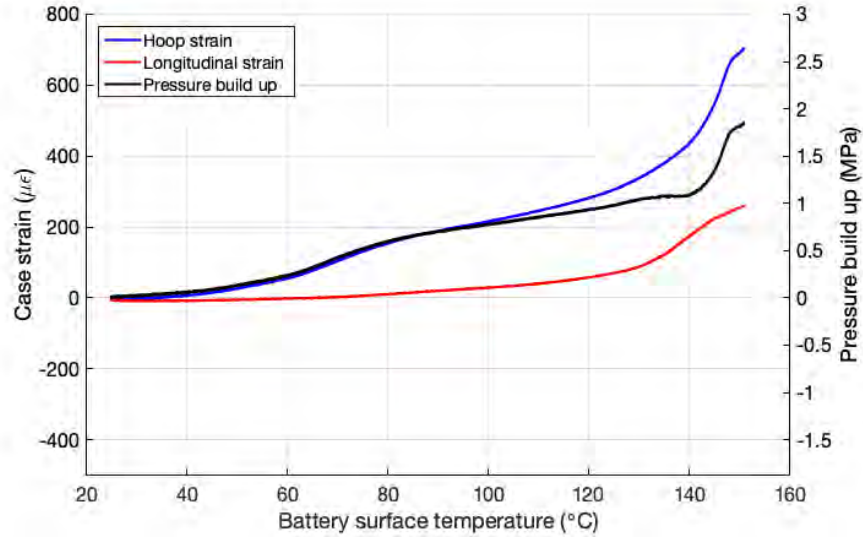


Figure 3.4: Hoop and longitudinal strain measurements and the corresponding indicated internal pressure for the repeated 4.8°C/min trial.

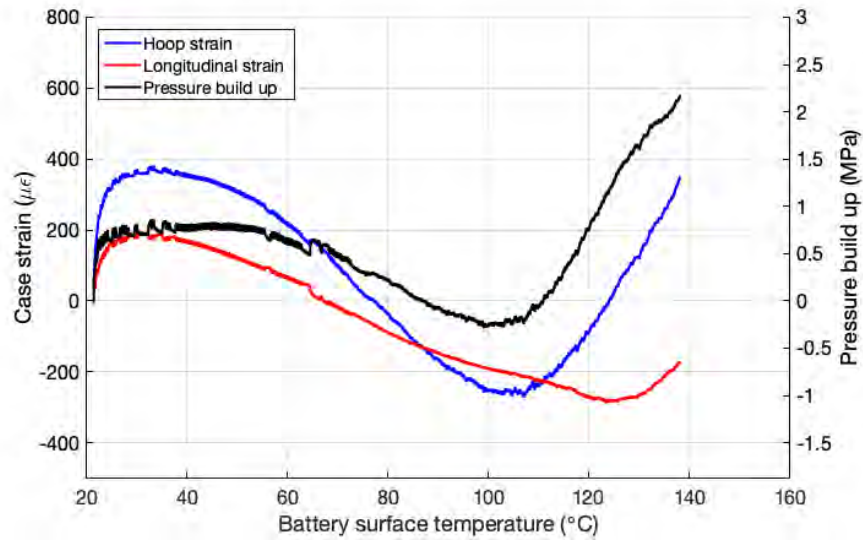


Figure 3.5: Hoop and longitudinal strain measurements and the corresponding indicated internal pressure for the 3.6°C/min trial.

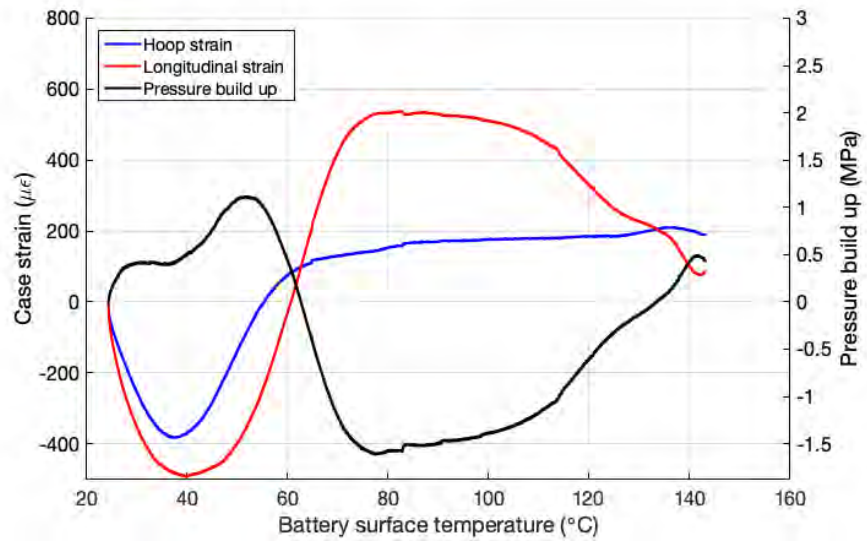


Figure 3.6: Hoop and longitudinal strain measurements and the corresponding indicated internal pressure for the 2.4°C/min trial.

All four tests demonstrated some erratic behavior in early strain measurements (typically below 100°C). This behavior manifested as an apparent or indicated internal pressure build up. Much of these early indicated pressures are clearly non-physical as they reached negative values multiple times larger than atmospheric pressure. This phenomena is attributed to potential interactions between internal battery components and the case along with relief of residual stresses from the forming process of the battery case. In the higher heating rate of both 4.8°C/min tests, these affects appear to have been minimized. While initial strain measurement trends appeared unpredictable, the difference between the two measurements provided the information needed to calculate internal pressure and was typically more consistent than individual measurements.

In all tests, a final rise in strain measurements and a growing difference between hoop and longitudinal values was noticed. This manifested as a rising internal battery pressure immediately prior to venting onset. The onset of this pre-venting pressure build up began at different moments for each trial, but all cells showed an accelerating rate of pressure build up until the battery vent ultimately opened. The final indicated burst pressure for each trail is listed in Table 3.1. Vents from LG branded batteries have an experimentally determined mean burst pressure of 1.906 MPa [9] which is comparable to these final pressures in all but the 3.6°C/min trial. The uncharacteristically low value for the strain based burst pressure measurement on this trial is attributed to the large negative indicated internal pressure before the final pressure build up. When considering the 2.06 MPa difference between the minimum (−1.63 MPa) and final indicated internal pressures for this trial, the pressure built up at the end of this trial is comparable to the burst pressure of an LG brand battery vent. Of note, the spread of these measured burst pressures can be accounted for by variability in vent mechanism burst pressure and the roughly 0.4 MPa measurement uncertainty range demonstrated in empty battery case validation experiments.

Table 3.1: Indicated burst vent burst pressure

Heating rate	Pressure (MPa)
4.8°C/min	2.50
4.8°C/min (repeat)	1.84
3.6°C/min	0.435
2.4°C/min	2.16

3.2 Pressure build up versus time and temperature

Due to the wide range of heating rates, the total test duration varied significantly between trials as shown in Figure 3.7. The final pressure build up time duration was also longer for lower heating rate tests. Time to failure and

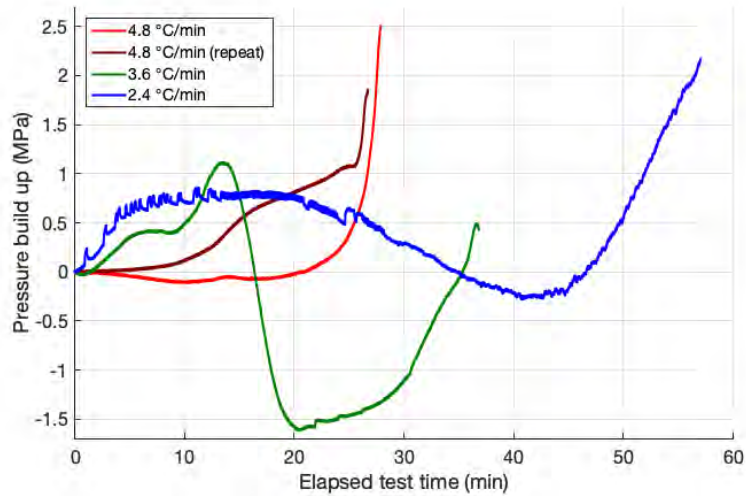


Figure 3.7: Comparing indicated internal battery pressure versus time between the four trials.

the beginning of accelerated pressure build up are similar between the repeated 4.8°C/min trials.

To demonstrate similarities between the trials in the internal pressure progression leading up to venting, measured pressure build up was plotted against battery surface temperature as shown in Figure 3.8. Here, it is clear that all batteries began venting at similar temperatures as tabulated in Table 3.2. Additionally, the final pressure rise began in all trials between 80°C and 110 °C. As such, rate of final pressure build up with respect to temperature was similar between all four trials. In all trials, the pressure build up appeared to accelerate somewhat before venting onset.

Table 3.2: Battery surface temperature at venting onset

Heating rate	Temperature (°C)
4.8°C/min	151.3
4.8°C/min (repeat)	150.8
3.6°C/min	143.2
2.4°C/min	138.2

3.3 Correlating pressure rise to self heating and thermal runaway

From the battery surface temperature traces first reported above in Figure 3.2, careful observation shows a slight upwards concavity to these trends which

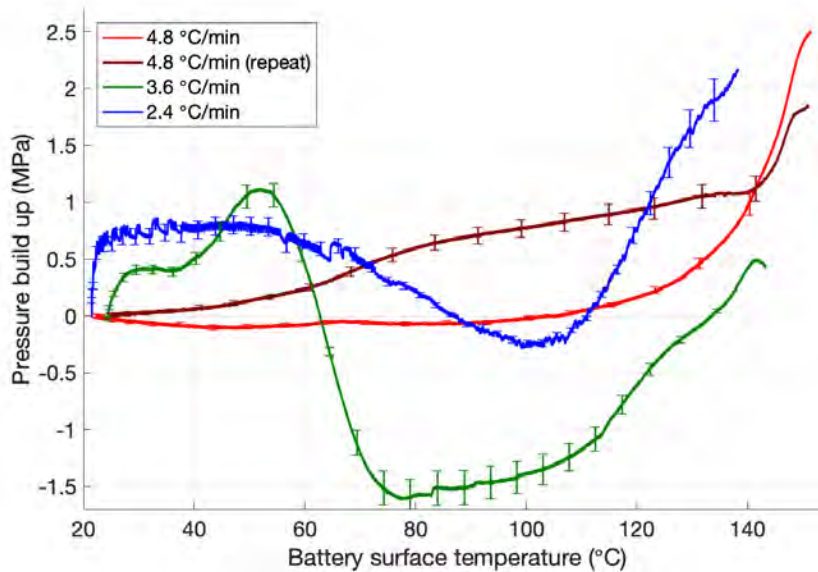


Figure 3.8: Comparing indicated internal battery pressure versus temperature between the four trials.

leads to an inference that reactions within batteries were generating heat in addition to the external heating from the battery calorimeter itself. Self heating is a characteristic of the thermal runaway phenomenon present in a battery failure which is ultimately associated to gas generation.

Shown in Figure 3.9, the battery surface heating rate is plotted against time for the four live cell tests. After an initial transience phase, the heating rates reached a nearly constant value close to the nominal desired heating rate for each trial. Venting onset was noted via the rapidly fluctuating then very rapidly increasing surface temperature rate which also corresponded to the measured chamber pressure response mentioned in the discussion of Figure 3.2. Immediately prior to venting, surface temperature heating rates can be seen to increase above the rate which would have been provided by the test apparatus which clearly indicates that self heating a thermal runaway was occurring.

To provide a consistent metric to determine when self heating begins, the second time derivative of battery surface temperature was calculated as shown in Figure 3.10. The initial large upwards concavity, before approximately 15 min, was associated with transience in the start up of the battery calorimeter. In the 2.4°C/min and 3.6°C/min heating rate tests, the test duration was sufficiently long that the battery surface temperature rate became slightly concave down which would be expected given the simplistic constant power operation of the calorimeter heaters would reach some steady state temperature eventually. However, the occurrence of self heating caused the surface temperature rate to once again become concave up, and the beginning of self heating was denoted as the

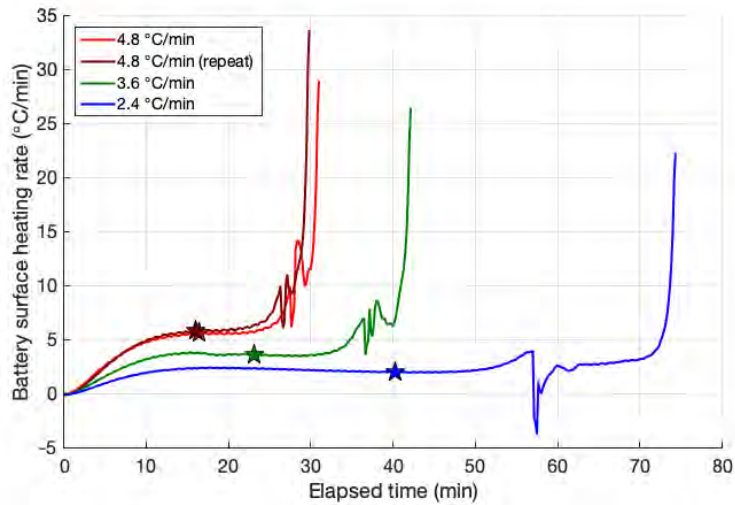


Figure 3.9: Battery surface temperature heating rate versus time. The beginning of self heating is annotated with colored stars.

second x-intercept of the the battery surface temperature second time derivative. In the two 4.8°C/min trials, the battery began self heating and vented before the second derivative of temperature plot could become steady and slightly negative. For these trials, the self heating was noted as beginning at the local minimum after initial calorimeter transience. The beginning of self heating is marked for each test with a colored star in Figures 3.9 and 3.10. Self heating began multiple minutes before venting in all four trials. Initially self heating had a small contribution to the overall heating of the battery but ultimately became the dominant factor in how the battery temperature progressed during failure.

To draw a connection between the observation of self heating and the noted final pressure build up before venting onset, the self heating beginning points were noted on the calculated internal pressure traces from Figure 3.8. Additionally, the self heating beginning point was vertically shifted to an internal pressure of zero to offset any residual effects of initial transience. Shown in Figure 3.11, the self heating point lies near the beginning of accelerated pressure build up in most trials. Prior to self heating, indicated internal pressures were unpredictable. After the battery itself began decomposing and generating heat, internal pressure measurements reliably show a significant increase ultimately leading to venting. Using self heating to approximate when thermal runaway occurred, the large increases in internal pressure during this period indicate gas generation from decomposition within the cell mainly occurred towards the end of these thermal abuse experiments. Prior to these self heating points, it is unlikely that a significant amount of gas would have been generated within the cells to cause a significant strain response to internal pressure.

Four 18650 format lithium ion batteries were heated until the point of fail-

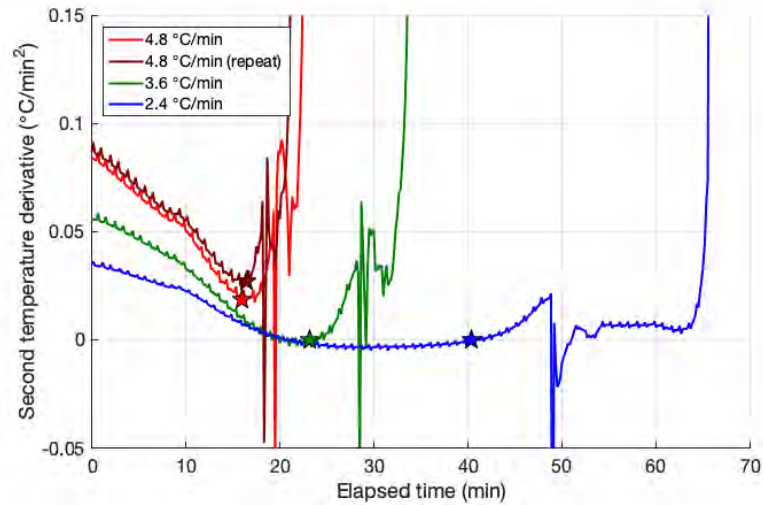


Figure 3.10: The second time derivative of battery surface temperature versus time indicating the concavity of the surface temperature curve and allowing inference of the beginning of self heating which is annotated with colored stars.

ure, and strain measurements were taken throughout this destructive test to attempt internal pressure measurement. Measurements were limited at lower temperatures due to residual strain and potential for interactions with tightly wound internal battery components. However, the strain based internal pressure measurement was ultimately able to capture the final pressure build up before venting onset. This final rise aligns well with the onset of thermal runaway which is inferred through the beginning of battery self heating. Additionally, since the final pressure rise is similar to the burst pressure of the vent mechanism, the majority of pressure build up and therefore gas generation only occurs after thermal runaway begins. However, battery self heating was also observed through simple temperature measurement as an indicator of imminent venting failure. Strain based internal pressure measurement was effective for observing thermal runaway and gas generation prior to venting onset, but this method should not be considered a replacement for temperature measurement as a means of state-of-health monitoring.

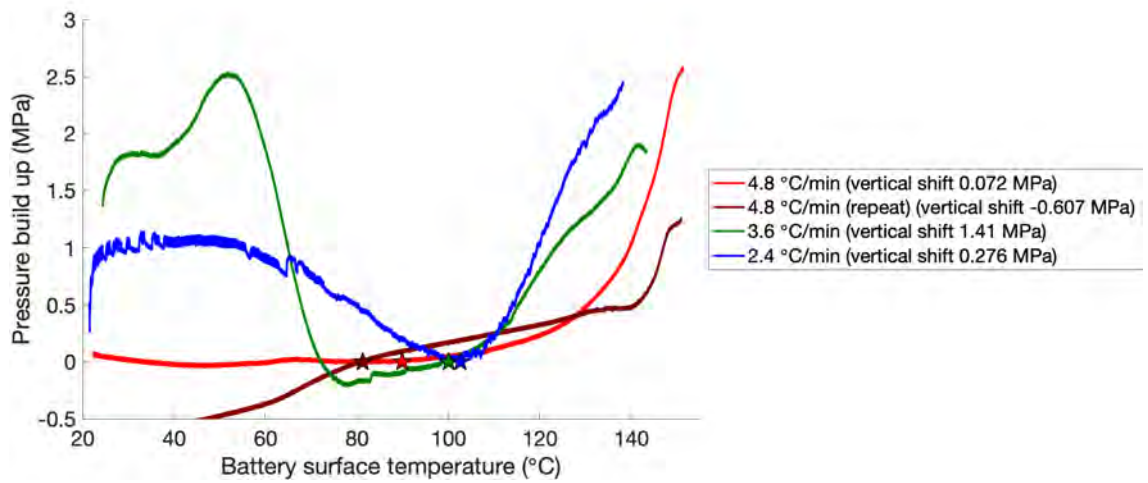


Figure 3.11: Indicated internal pressure curves with the beginning of self heating indicated with colored stars. Pressure traces have been vertically shifted so the self heating onset moment lies at zero internal gauge pressure to demonstrate the comparable magnitude of the final pressure build up between all trials.

CHAPTER 4

SIMPLIFIED BATTERY VENTING MODEL FOR INFORMING FLOW BOUNDARY CONDITIONS

A simplified, one-dimensional venting model is defined here to demonstrate the relation between pressure build up within a finite volume and vent mechanism parameters to describe how pressure varies with time. By predicting cell pressure as a function of time throughout venting, the applicability of the PIV and high speed schlieren experiments may be described.

Previous experimental work at New Mexico Tech by the author has experimentally determined the boundary and initial conditions for a simplified transient venting model able to describe the battery internal pressure after burst along with mass flow rate [78]. Mean values the statistical distribution of burst pressure (P_b), opening area (A_e), and discharge coefficient (C_d) were measured for vent caps including the MTI brand vents used here [9]. This model is intended to inform under what circumstances simulated venting flows may be representative of actual live cells venting under abuse conditions.

Beginning with conservation of mass within a control volume surrounding a hypothetical venting 18650 format cell, the rate of change of mass contained within the battery ($\frac{dm}{dt}$) is equivalent to the negative of the mass flow rate out of the cell (\dot{m}_{out}):

$$\frac{dm}{dt} = -\dot{m}_{out} \quad (4.1)$$

Assuming constant properties within the cell and using the Ideal Gas Law, the mass within the cell is:

$$m = \frac{P_0}{RT_0} V \quad (4.2)$$

where P_0 and T_0 are the stagnation pressure and temperature, respectively. The pressurized volume of fluid is V which is approximated as $1.52 \cdot 10^{-6} \text{ m}^3$ [47]. Taking the time derivative allows rewriting of the left hand side of Equation 4.1:

$$\frac{dm}{dt} = \frac{V}{RT_0} \frac{dP_0}{dt} \quad (4.3)$$

Further, the actual mass flow rate out of the cell is equal to the product of discharge coefficient and the maximum theoretically possible flow rate which occurs under isentropic conditions. The right hand side of Equation 4.1 can be written as:

$$\dot{m}_{\text{out}} = C_d \cdot \frac{P_0}{\sqrt{RT_0}} A_e \sqrt{\gamma} M_e \left(1 + \frac{\gamma - 1}{2} M_e^2 \right)^{\frac{\gamma+1}{2-2\gamma}} \quad (4.4)$$

where M_e is the Mach number at the vent cap exit. If the ratio of stagnation pressure to atmospheric pressure (P_0/P_{atm}) is greater than 1.892, the flow is choked, the Mach number at the vent cap exit is fixed at unity. In this circumstance, the exit pressure is greater than atmospheric, so the flow is described as under expanded. At $P_0/P_{atm} = 1.892$, the exit pressure will reach atmospheric pressure and this choked flow is said to be perfectly expanded. Once P_0/P_{atm} drops below 1.892, exit pressure will be assumed to be equal to atmospheric pressure and the flow will be un-choked. To calculate the exit Mach number of an un-choked flow the equation:

$$\frac{P_0}{P_{atm}} = \left(1 + \frac{\gamma - 1}{2} M_e^2 \right)^{\frac{\gamma}{\gamma-1}} \quad (4.5)$$

will be solved for M_e .

By substituting Equations 4.3 and 4.4 into Equation 4.1 and simplifying, a differential equation for pressure as a function of time is achieved:

$$\frac{dP_0}{dt} = -C_d \cdot \frac{P_0 \sqrt{RT_0}}{V} A_e \sqrt{\gamma} M_e \left(1 + \frac{\gamma - 1}{2} M_e^2 \right)^{\frac{\gamma+1}{2-2\gamma}} \quad (4.6)$$

The initial condition $P_0(t = 0) = P_b$ is applied to determine the single constant of integration necessary. Solving this equation as an exponential decay would be trivial under constant parameters, but previous testing has demonstrated that discharge coefficient is a function of stagnation pressure and the exit Mach number clearly changes as the flow becomes un-choked [78, 47]. In practice, Equation 4.6 is solved numerically with a fourth-order Runge-Kutta differential equation solver in MATLAB (“ode45” function). The mean burst pressure and opening area of MTI brand vent caps are 2.158 MPa and 8.967 mm² respectively. The mean discharge coefficient profile versus pressure is approximated as a constant value of $C_d = 0.75$ below a normalized stagnation pressure of $P_0/P_{atm} = 2.2$ and $C_d = 0.95$ above $P_0/P_{atm} = 3.2$ with a linearly varying section in the middle. To accommodate for discharge coefficient and Mach number both being piecewise functions of stagnation pressure, an intermediate function recalculates values for both parameters every time the Runge-Kutta solver calculates dP_0/dt . To avoid complex valued exit Mach number values, Mach number is automatically set to zero when stagnation pressure reaches atmospheric pressure. The volume

of the pressure reservoir within the battery was approximated as 1.52 cm^3 [28]. Venting calculations are made with $\gamma = 1.4$ representing air and a constant stagnation temperature of 293 K to represent the steady state gas venting described in Chapter 7.

Figure 4.1 shows stagnation pressure as a function of time after venting onset. The region of interest immediately after burst is experimentally simulated with the test apparatus described in Chapters 5 and 6. However, as time progresses, the experimental flow no longer accurately represents an actual battery failure because gas is still supplied from an upstream pressurized cylinder. Venting at stagnation pressures lower than 345 MPa is simulated by trials at discrete stagnation pressure set points. While the burst trials with simulated electrolyte are transient and multiphase in nature, these steady, fixed point gas venting experiments provide accurate velocity distributions without the flow field. By testing under steady conditions, trial length can be as long as desired which allows enough data to be recorded to accurately quantify the mean velocity field and turbulence strength.

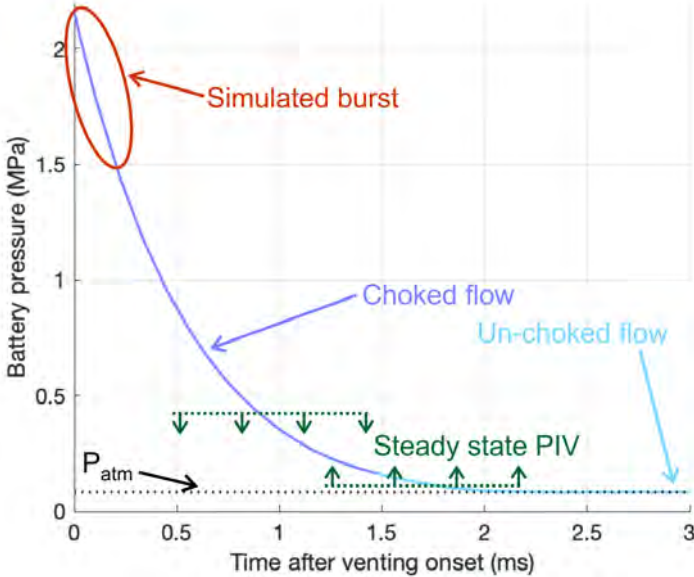


Figure 4.1: Battery internal pressure versus time after burst showing the regions in which the current vent burst and steady state PIV experiments are applicable.

CHAPTER 5

OPTICAL MEASUREMENT TECHNIQUES FOR TRANSIENT, MULTIPHASE VENTING FLOW

5.1 Principals of high speed schlieren and equipment used

Schlieren imaging is a technique within a family of flow visualization methods including shadowgraphy and background oriented schlieren which allow the visualization of changes in refractive index within a transparent media [89]. In the case of gaseous flows, index of refraction disturbances are generally caused by variable density or multiple gas species. As such, schlieren and the other refractive imaging techniques are able to visualize flow features such as shock waves and compressible turbulence with density gradients or mixing between multiple gas species. For a gas, refractive index varies linearly with density via the Gladstone-Dale Law:

$$n = k\rho + 1 \quad (5.1)$$

where n is the index of refraction, k is a material constant which varies by chemical species, and ρ is density.

A parallel-light schlieren system was implemented here for visualizing gas venting from battery cells, as depicted in Figure 5.1(a). Light from a point source placed at the focal length of a convex lens was collimated into a test section where the simulated battery venting test fixture was placed. Beyond the collimated test section, a second convex lens collects the light and refocuses it to a point. At this point, a knife edge is carefully placed to block approximately half of the light before it enters the high-speed camera's lens. Since the knife edge cutoff is placed at the focus of the light, it does not distort the image the camera collects but rather provides an even darkening effect throughout the field of view. When a schlieren object (a feature which refracts light) is introduced to the test section, the refracted light rays will focus to a different location. Light which focuses on the knife edge creates dark regions within images while the refracted light which now misses the cutoff creates light regions. This leads to the light-to-dark gradients across flow structures which is characteristic to schlieren images as shown in Figure 5.1(b). Of note, opaque regions within the test section block light and appear black within schlieren images. Schlieren imaging can be performed without the need for a specialized camera and provides intuitively-understandable flow visualizations which allow various measurements and insights into flow features.

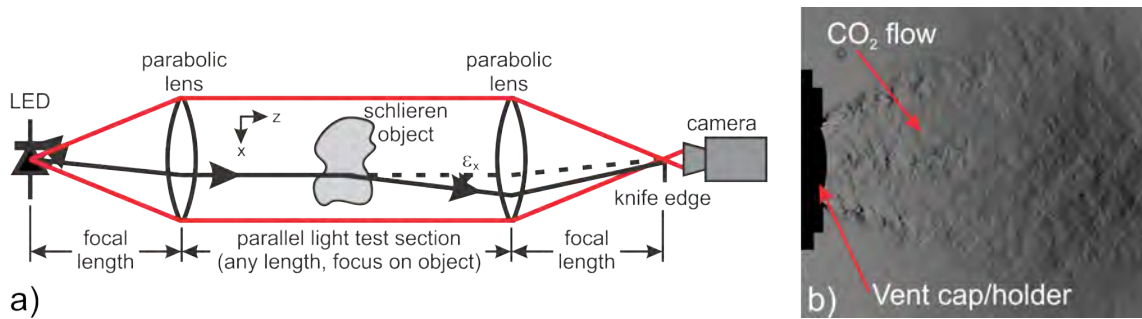


Figure 5.1: (a) A schematic representation of the schlieren setup used, and (b) a representative image of the schlieren images recorded of simulated battery venting.

All schlieren images recorded in this work were taken with a Photron SA-X2 high speed digital camera. Camera resolution was set to 384 by 584 pixels (px) with a spatial calibration between 0.1 mm/px and 0.15 mm/px depending on the individual trial and camera lens focal length. Images were generally recorded at a frame rate of 48 kHz with an exposure of 0.29 μ s, but this was changed as needed. The lenses used to collimate and collect light were a matched pair of 127-mm-diameter parabolic telescope objectives with an aperture of $f/5$. Point source illumination was provided by a SugarCUBE brand light emitting diode (LED) illuminator with adjustable intensity output.

Here, carbon dioxide was chosen as a substitute for the mixture of gases present in battery venting as it is generally the most prevalent species within these flows without being combustible or highly toxic. Depending on cell chemistry, carbon dioxide has been measured to account for between 24.9% and 53.0% of vented gas material [28]. The other significant components of gas venting are hydrogen and carbon monoxide. Carbon dioxide also has the added benefit of having relatively high visibility in schlieren imaging in an air atmosphere.

5.2 Vent cap burst fixture with visualization capability

Intact vent caps, sourced as components, are placed within the vent burst pressure test fixture shown installed in the laboratory in Figure 5.2(a). The fixture was designed and fabricated predominantly from commercially available off-the-shelf components for simplicity. The vent cap is placed within a parallel light schlieren system for visualization of both gas and liquid components of the flow.

Brass and steel pipe fittings were used to construct the vent cap holding fixture without needing complicated machining. Carbon dioxide is supplied from a siphon-less compressed gas cylinder via a 12.7 mm outer diameter tube which is connected to the fixture with a stainless steel Swagelok tube fitting. The gas supply was then directed through a ball valve to the main fixture body.

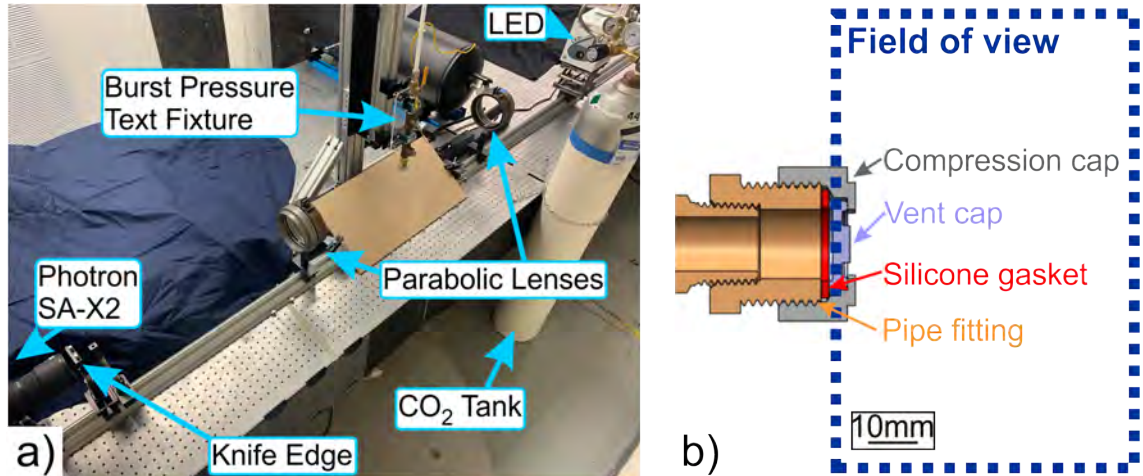


Figure 5.2: (a) The burst fixture installed in the laboratory, and (b) a schematic of the setup showing the construction of the vent holder and the field of view.

This main structure was constructed from galvanized steel pipe nipples and Tees which allow for pressure measurement ports. The ball valve was used to stop the flow of gas once the vent cap opened to end the test, but it is left open during testing. All pipe fittings used either tapered NPT threads or Swagelok style compression fittings, up to the main body of the fixture, after which straight threads were used to allow variability in vent cap thickness.

A brass 3/8 NPT to 1-8 UNC straight thread fitting with a custom designed aluminum cap was used to secure the battery vent cap. A silicone gasket and laser cut acrylic gasket retaining ring are placed adjacent to the vent cap to create a seal for the pressurized gas prior to burst. A cutaway model view of the test apparatus is shown in Figure 5.2(b). The aluminum cap was machined to hold the vent cap in place while minimizing obstructions within the field of view adjacent to the vent openings. The only obstructions within the field of view are the two cantilevered tabs on the holding ring which keep the vent cap sealed against the silicone gasket. These tabs also provide a spatial calibration as their outer corners are 25.4 mm apart. The front of the vent cap sits 0.5 mm past the front of the compression nut to ensure that the test apparatus is minimally obstructing the field of view.

The vent cap holding fixture was mounted to an acrylic plate which is supported by four posts on an optical table. A length of high-pressure rated nylon tubing connects the vent cap holder to the compressed air supply which can be regulated between 0 MPa and 3.45 MPa. The pressure regulator was operated manually to increase pressure to failure during testing, and a dial type pressure gauge was used on the outlet of the regulator to confirm the reading from the pressure transducer installed on the vent cap holder. A follower-hand on the downstream pressure gauge showed the maximum pressure in each test, corresponding to the vent burst pressure. A compressed air cylinder was used for vent

testing as it could supply sufficiently high pressures.

5.3 Sucrose solution as an electrolyte substitute

Common liquid electrolytes in lithium ion batteries contain mixtures of organic hydrocarbons such as ethylene carbonate, dimethyl carbonate, and propylene carbonate [33]. To avoid flammability concerns with using these compounds, sucrose solutions were tailored to match individual properties of ethylene carbonate. Exact electrolyte formulations are generally proprietary and differing between different cell chemistries and manufacturers, so the simulated electrolyte is formulated to roughly approximate electrolyte spray characteristics while measurement techniques are being developed. Table 5.1 compares the applicable fluid dynamic properties of ethylene carbonate to the two sucrose solution mixtures [90, 91, 92]. Both sucrose solutions were created in warmed, distilled water with a small amount of food coloring to promote differentiation from gas venting in schlieren images and sucrose.

Table 5.1: Properties of ethylene carbonate electrolyte and sucrose solutions

Sample	Density (g/cm ³)	Viscosity (cP)
Ethylene carbonate	1.34	2.56
26% sucrose/water	1.11	2.57
69% sucrose/water	1.34	329

While no sucrose solution will provide perfect similarity to hydrocarbon electrolytes, the different mixtures were compared to evaluate which parameter was most critical for matching the results in previous schlieren imaging of live battery failures. Figure 5.3 shows schlieren images of simulated vent burst compared to a live cell failure at approximately 2.8 ms after burst. Both the 26% sucrose solution and the live cell failure show a similar spray with clear atomization while the 69% sucrose solution shows droplet breakup characteristics of the second wind-induced regime. The main visually observable differences between these two flow regimes is the different droplet sizes where atomized particles were significantly smaller than those in the second wind-induced regime [58]. The wind-blown particles in Figure 5.3(c) also demonstrated breakup outside of the vent orifice and at downstream locations in the flow [59]. Atomized flow broke apart at the orifice itself [59].

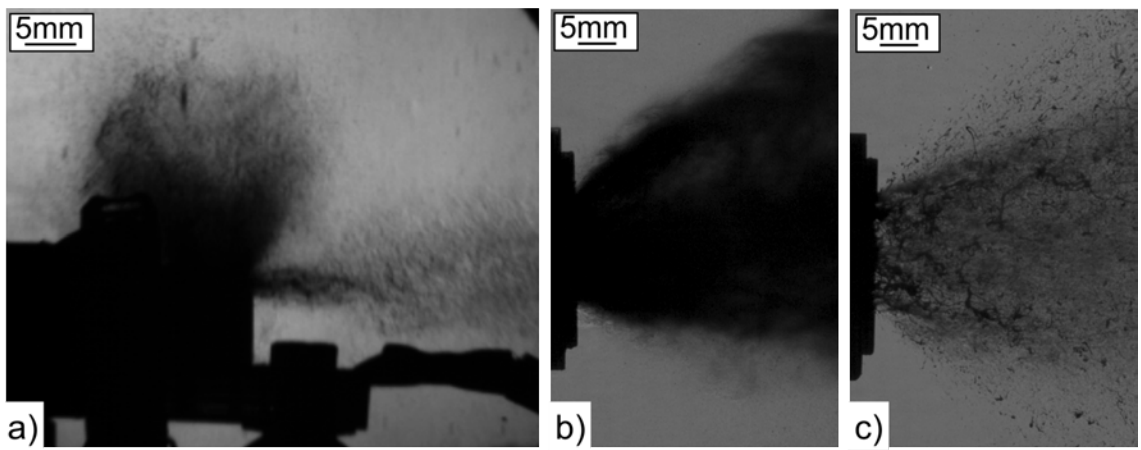


Figure 5.3: High speed schlieren images of (a) a NMC chemistry 18650 battery venting under thermal abuse, (b) atomization of 26% sucrose solution, and (c) wind-induced breakup of the 69% sucrose solution. The live cell failure image was taken $2,800 \mu\text{s}$ after venting onset while the two simulated burst images were recorded $2,792 \mu\text{s}$ after onset.

CHAPTER 6

EXPERIMENTAL RESULTS AND DATA ANALYSIS OF SIMULATED VENTING EXPERIMENTS

Using the previously described vent burst testing fixture and high speed schlieren imaging technique, experiments were conducted to:

- Determine how the introduction of a liquid phase affects the velocity, flow front penetration, and spreading rate of transient venting flow.
- Characterize the fundamental transient, multiphase fluid dynamics of the flow field created by multiple jets issuing from a finite volume, pressurized reservoir.

Three trials were performed to evaluate the role of the liquid component in venting flow immediately after vent mechanism burst: a baseline gas venting case and two trials with sucrose solutions which simulate the electrolyte portion of venting. In these experiments, carbon dioxide was used as the gas component of the venting flow for improved visibility in the schlieren imaging and to replicate the properties of gases vented from batteries. The initial portion of the venting flow represents the transience associated vent burst, but, unlike venting from a finite volume, experiments reach a steady state venting condition once gas flow becomes choked within the upstream pressure regulator. As such, these experiments are only representative of battery venting in early time scales.

All trials were performed with the vent cap in a vertical orientation to allow even spread of the 1 mL of simulated electrolyte against the burst disk. The schematic representation of the test fixture seen in Figure 5.2(b) shows how the schlieren field of view is reported in data throughout this chapter, but Figure 6.1 shows how the fixture was oriented in the lab and the location of the sucrose solution before vent burst. Care was taken to pipette the sucrose solution directly onto the burst disk rather than the inner surface of the test fixture, and the initial depth of the liquid was 6.1 mm.

The baseline trial, with a series of recorded schlieren imaging frames in Figures 6.2 and 6.3, had clearly identifiable individual jets correlated to the location of each of the openings in the vent's electrical terminal. Imaged with a collimated light schlieren setup, this image is the path integrated refraction of light passing through the test section. The image appears to show three individual jets, one directed upward, downward, and horizontally. The horizontal jet is

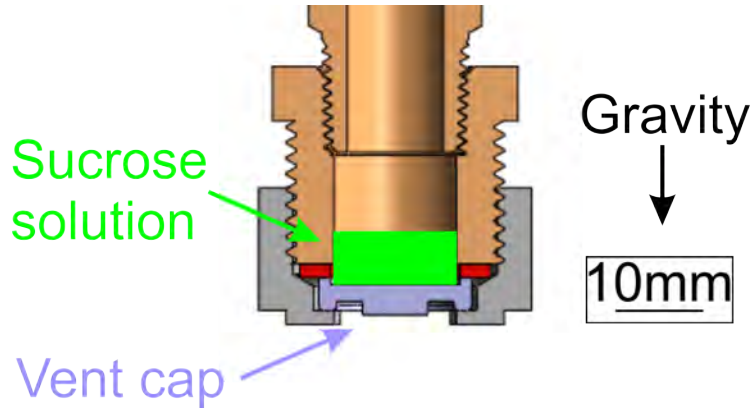


Figure 6.1: Schematic cross section showing the location of the sucrose solution within vent burst test apparatus prior to venting onset.

actually the projection of the two separate jets which are aligned in this viewing orientation. The parallel light schlieren system precludes any depth resolution in the image so the jets appear as one combined jet. The initial image series in Figure 6.2 shows the initial formation of the individual jets along with a weak shock wave associated with the opening of the burst disk. In the later timescales shown in Figure 6.3, jetting appears to have consistent projection and spreading angles once the flow has established.

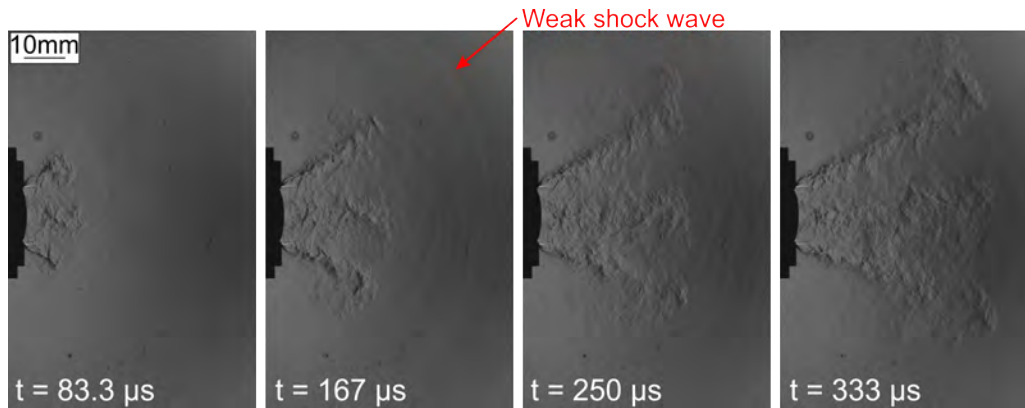
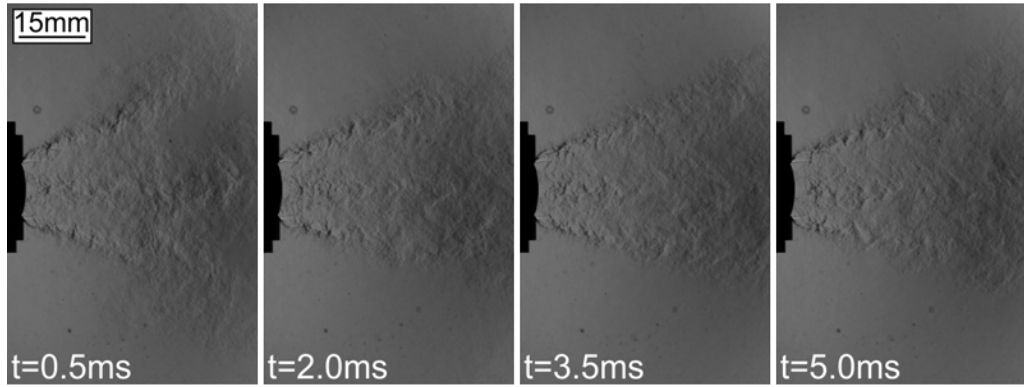


Figure 6.2: High speed schlieren images from gas-only burst trial showing the initial jet propagation into the environment.

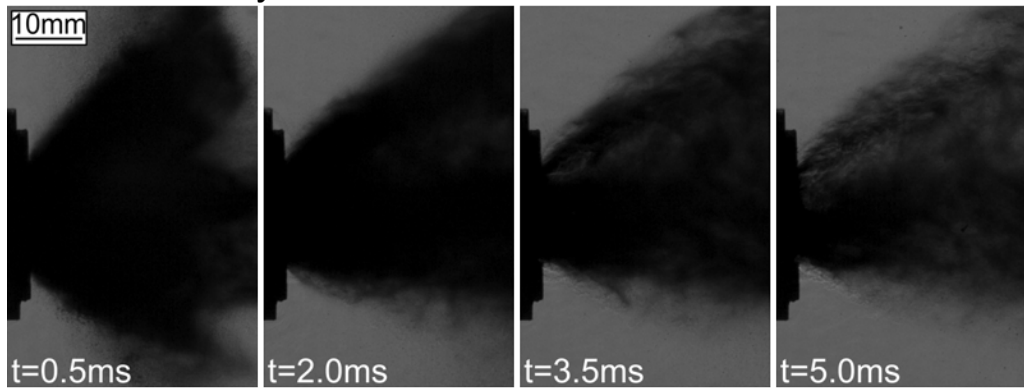
The other two tests vented the sucrose solutions described in Section 5.3 along with gaseous carbon dioxide. Shown in Figure 6.3, the low viscosity sucrose solution formed an atomized spray while the larger droplets of the high viscosity solution with ligament formation is characteristic of the second wind-induced breakup regime [58]. Both flows showed a droplet spray that was initially wider in the radial direction than gas venting alone, but the droplet spray was continually narrowing as the liquid within each cap was vented. After the

sucrose solutions were vented, the gas venting established with steady projection and spreading angles similar to the gas-only trial. Unevenness, as noted in the bottom jet from the low viscosity solution trial, is attributed to the burst disk remaining attached within the vent mechanism at a single point which blocked a portion of the corresponding opening in the vent's electrical terminal. The individual droplets in the atomized spray were too small to be resolved individually, but these particles were densely populated and darkened the schlieren images. The atomized flow blocked schlieren visibility until most of the liquid within the vent had been exhausted. The high viscosity wind-induced flow performed similarly, but larger gaps between particles allowed more visibility for the gas component of the flow.

Gas only:



Low viscosity solution:



High viscosity solution:

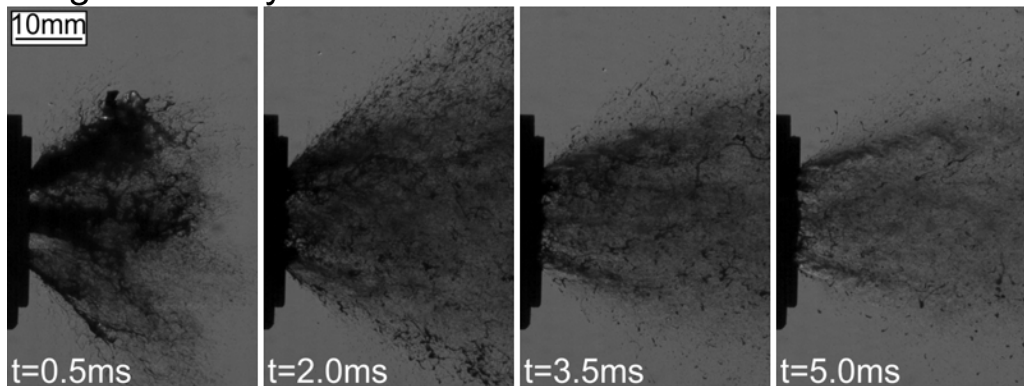


Figure 6.3: High speed schlieren images from all three trials.

An image processing routine was written in MATLAB to isolate the liquid venting components from the gas within the high speed schlieren images. The ability to distinguish between liquid and gas portions of the flow is necessary to understand the fluid dynamics of multiphase venting. Liquid droplets will interact with the flow and carry momentum in different ways based on the spray regime and the corresponding particle sizes. From a battery safety perspective, flammable electrolyte droplets also contain significant chemical potential energy and may coat surfaces near venting cells.

A mean gas flow image was created from the steady venting portion of the high speed schlieren image sets after the carbon dioxide portion of the flow choked within the regulator. This mean image is calculated via pixel by pixel averaging from 480 schlieren images for each trial since there were slight flow field differences related to unpredictable burst disk opening characteristics. This mean flow image was then subtracted from each transient test image to minimize the intensity of the schlieren effect caused by the gas flow. To be able to visualize these mean-subtracted images, pixel intensities were rescaled such that no change between the transient and mean images was represented a 50% gray. The darkest regions of these subtracted images were isolated as they represent the location of the liquid droplets. These liquid portions of the flow were then highlighted with red pixels. If the intensity difference between the mean schlieren gas venting and the transient spray image at a given pixel location was larger than 0.1, the flow was assumed to be liquid. The steps of this image processing routine are shown in Figure 6.4.

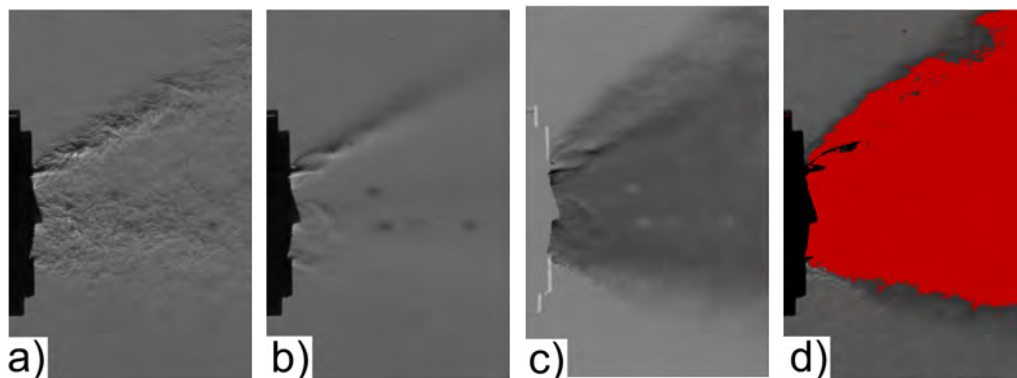


Figure 6.4: Liquid detection image processing steps including (a) raw steady-state schlieren images, (b) mean steady gas venting, (c) multiphase venting image with mean schlieren subtracted, and (d) liquid portions of the flow determined by thresholding (c) and highlighting in red. The raw droplet spray image processed in parts (c) and (d) is the low viscosity, $t = 5.0$ ms frame shown in Figure 6.3.

Streak images were created to analyze how the venting flow changed with time along one-dimensional axes within the recorded schlieren images. Streak images are compiled by removing the same row or column of interest (sometimes along with adjacent rows or columns to visually assist with distinguishing

flow features) from successive high speed images [93]. These one-dimensional image intensity vectors are then concatenated into a larger image which represents position on one axis and time on the other as shown in Figure 6.5.

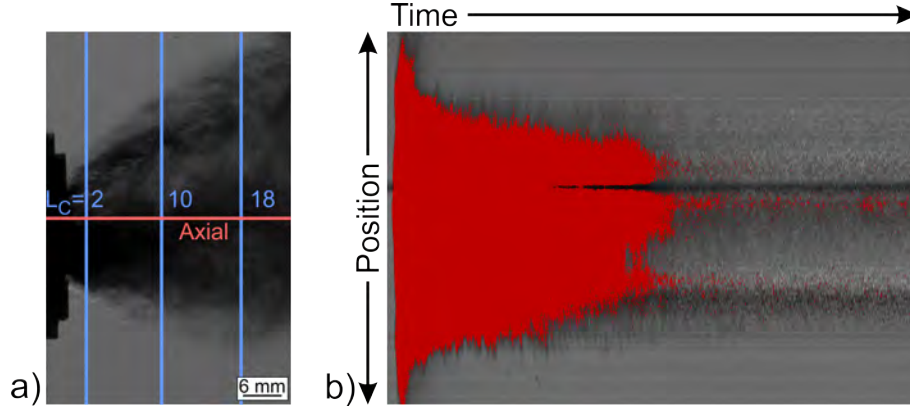


Figure 6.5: (a) Single high speed image of the flow identifying axial and radial locations where streak images are created, and (b) a radial streak image created from the column at $L_c = 10$.

Streak images were created from the high-speed schlieren images along the axial direction and radial direction, perpendicular to the vent exits. A characteristic length L_c scale has been defined:

$$L_c = \sqrt{\frac{\overline{A_e}}{n_{jets}}} \quad (6.1)$$

for the MTI brand vent caps tested. With an exit area ($\overline{A_e}$) of 8.967 mm^2 and number of jets (n_{jets}) of 4, the characteristic length is 1.497 mm . Relative locations for $2L_c$, $10L_c$, and $18L_c$ are shown in Figure 6.5(a).

Figure 6.6 compares the radial streak images created from the high speed schlieren images recorded in the three simulated vent burst trials. Gas jet projection and spreading angles were constant through time which was visualized as horizontal bands in the streak images. From further inspection, gas spreading and projection, when discernible from the liquid portion of the flow, were unaffected by the introduction of the droplet spray.

Projection and jet spreading angles are calculated by noting the vertical location of the center and edges of the jets within streak images in Figure 6.6 at different known distances from the vent cap. The gas experiment was used to determine the outward projection of the jets which was measured at 21° from the axial direction normal to the vent cap. The individual gas jet width spreading angle was measured as 12° . From this, the entire gas flow field spreads within a cone with a full angle of 66° .

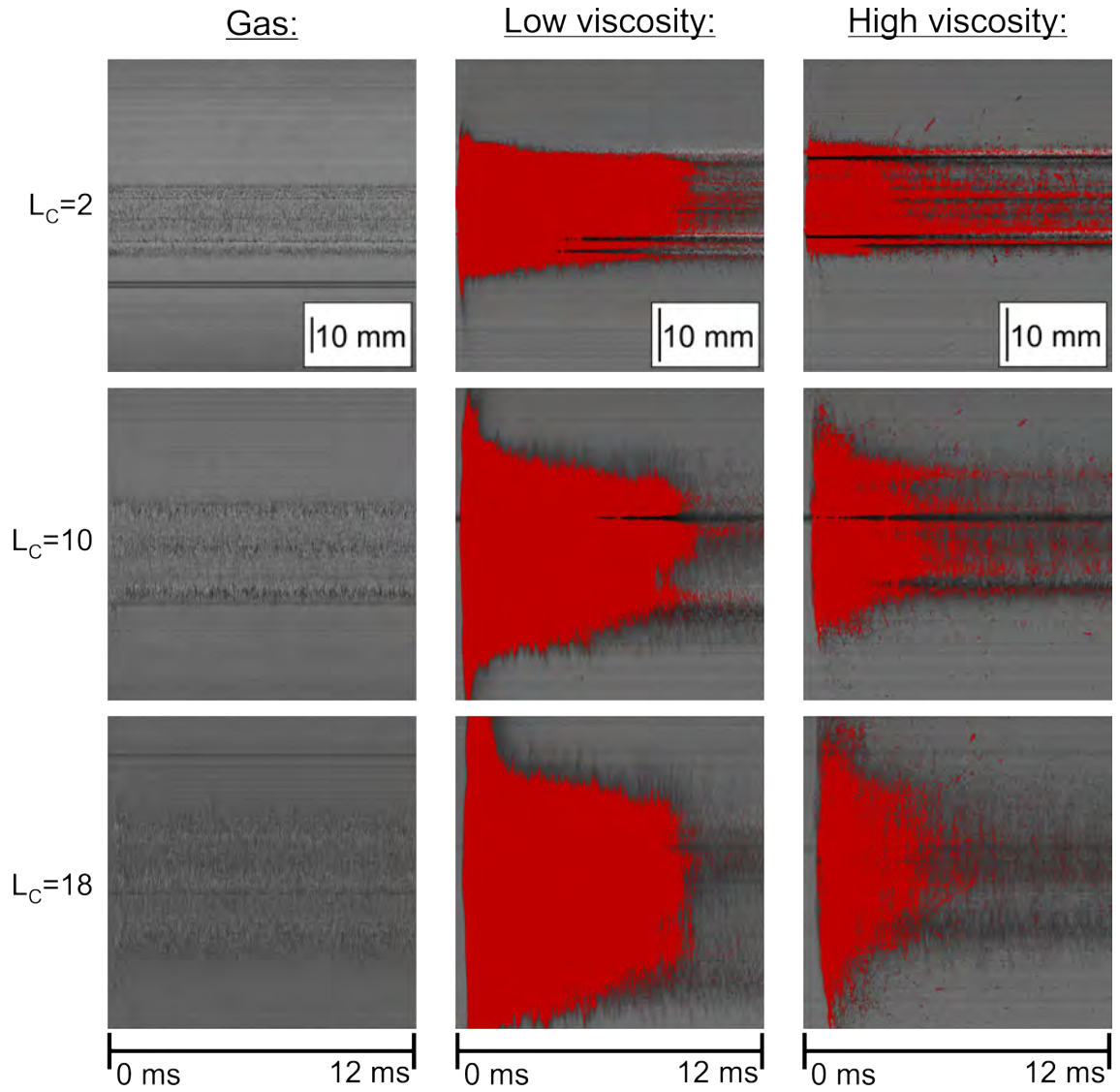


Figure 6.6: Streak images showing 12 ms of venting after burst for all three scenarios showing how the flow field evolves in the radial direction at distances of $2L_C$, $10L_C$, and $18L_C$.

For both trials with a liquid component to the venting flow, the streak images in Figure 6.6 demonstrate that droplet spray governed the extent of the flow field and initial penetration into the quiescent environment. Generally, the low viscosity, atomized spray was wider than the high viscosity, wind-blown spray. As time progressed and the amount of liquid remaining in the burst pressure test fixture decreased, the flow field became less densely populated by liquid droplets. Even though the total width of the initial droplet spray was greater than the gas venting radial width, the droplet spray narrowed with time, eventually tending to a spreading angle of zero as the liquid was exhausted. Since the liquid spray width was decreasing with time while the gas venting remained constant, the outer edge of the entire flow field transitioned from being comprised of droplets to gas at 2.5 ms and 5.0 ms after burst for the high viscosity and low viscosity trials, respectively. Qualitatively, the low viscosity, atomized spray occupied more of the flow field for longer than the high viscosity, wind-blown spray.

Unlike the gas venting case, the liquid spreading angle clearly varies significantly with time as seen in the streak images in Figure 6.6. Here liquid spreading angle (θ_L) was calculated as the tip angle of a cone enveloping the droplet spray at a distance of $10L_c$ and was calculated as:

$$\tan\left(\frac{\theta_L}{2}\right) = \frac{0.5 \cdot (\text{Droplet Spray Width})}{10L_c} \quad (6.2)$$

The distance of $10L_c$ was chosen because it was the furthest downstream location where both trials' droplet spray remained within the camera field-of-view. The droplet spray width is defined as the radial distance between the top and bottom edges of the detected liquid spray at a given time. The spreading angle of a cone bounding the entire flow is shown in Figure 6.7. The initial rise of spray angle was due to the fact that the spray angle measurement was taken at a distance of $10L_c$ from the vent cap. These values simply represent the center jet penetrating to this distance. Once the maximum spray angle measurement was reached, droplet spray angle steadily decreased with time until the liquid component of the venting was exhausted. Both sucrose solutions exhibited nearly identical total venting time suggesting that viscosity and density variation did not significantly affect the liquid flow rate. Throughout venting, the low viscosity solution demonstrated a wider spray than the high viscosity solution which is directly associated with the differences in the two demonstrated spray regimes. This was consistent with previous experimental work which noted higher concentrations of high Stokes number particles closer to the center of a jet while lower Stokes number particles spread further towards the edges of the jet [63]. The larger droplets from the high viscosity spray showed some spray angle oscillations later in the venting process while the atomized flow was more consistent in the spray angle decrease.

To evaluate spray penetration into the quiescent environment immediately after burst, the axial streak images created from the vent centerline row were used to track the flow front. Of note, the venting flow front is comprised entirely of

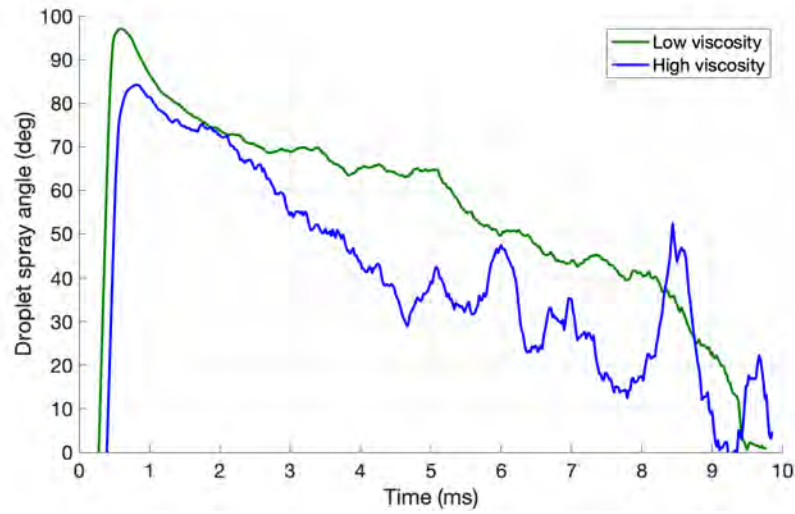


Figure 6.7: Droplet spray cone angle (θ_L) versus time for both high and low viscosity trials.

liquid for both high and low viscosity sucrose solution trials. The stages of an image processing routine to measure the position of the flow front are shown in Figure 6.8. The images to create the displayed streak image were recorded during the gas venting trial. The streak image was first binarized by thresholding pixels based on their intensity difference from the no-flow condition. Then image dilation and erosion steps were performed to fill in gaps along the flow front within the streak images.

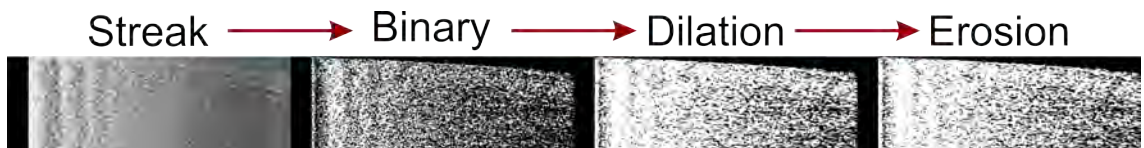


Figure 6.8: Flow front tracking image processing methodology.

From the above streak images, the spray tip arrival time at a given distance (column within the streak image) is simply the distance of the first white pixel from the top of the image. By applying a length to pixel scale and correlating frame numbers with time values since vent burst, spray tip penetration versus time was calculated and is shown in Figure 6.9. The addition of liquid slowed spray tip penetration. While the low viscosity solution was close to matching the gas flow, the high viscosity spray was significantly slower. All three flow fronts showed some degree of deceleration within the field of view, but the larger droplets from the high viscosity spray retained momentum the best.

Similar to tip penetration, the venting flow time-of-arrival was mapped within the domain of the camera's field of view as depicted in Figure 6.10. The

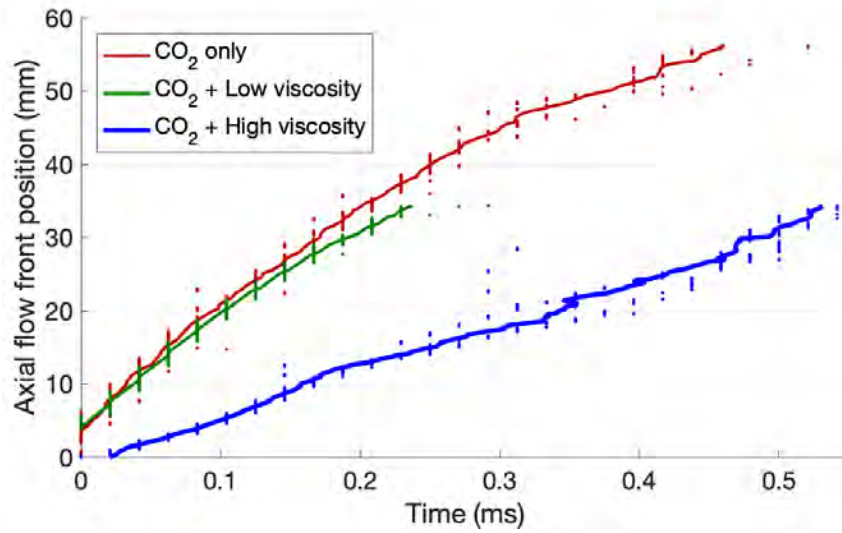


Figure 6.9: Flow front propagation through time for three burst scenarios.

same trends noted in the axial spray tip penetration measurements were noted for the full-field time-of-arrival plot. The gas and low viscosity venting flows were observed to establish the extent of their flow field within approximately 0.5 ms while the high viscosity flow took closer to 1 ms. Of note, the later time of arrival between and at the edges jets in the gas flow field was due to turbulent fluctuations in the flow field.

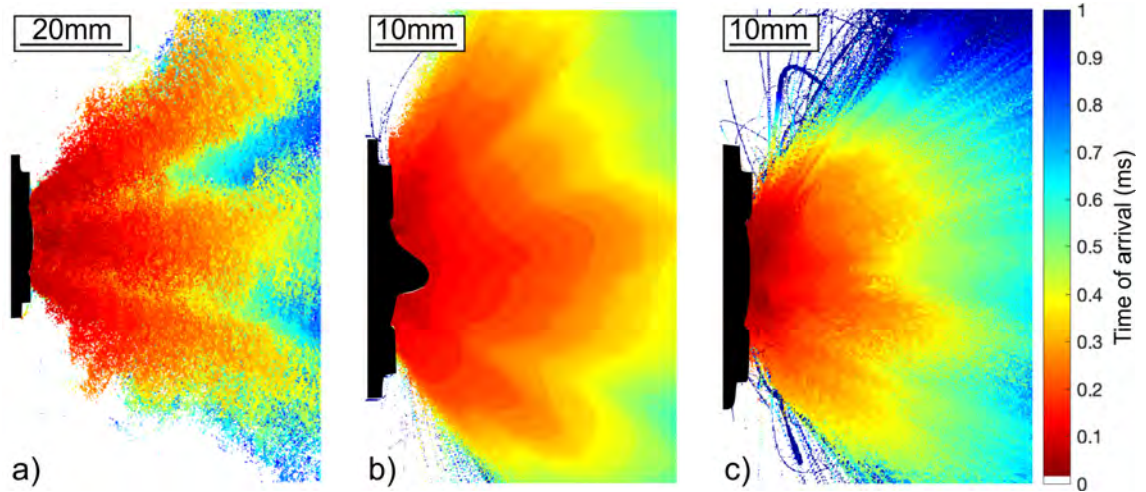


Figure 6.10: Time-of-arrival maps depicting when venting flow was first noted at a given location near the vent cap.

CHAPTER 7

PARTICLE IMAGE VELOCIMETRY (PIV) MEASUREMENT FOR STEADY MULTIPLE-JET VENTING FLOW

7.1 Steady state gas venting test apparatus

Steady state, simulated gas venting experiments are performed with a test apparatus specifically designed and fabricated for use with 18650 format vent caps and custom geometry orifice plates. While the experiments presented in Chapter 9 only utilize orifice plates, the laboratory system was designed with modularity and robust capabilities for future experiments beyond the scope of this body of work. The majority of the test apparatus and associated fixtures are constructed from off-the-shelf components, but custom-fabricated parts were made where necessary.

Major components of this fixture include the orifice plate or vent cap holder, stilling chamber, and two chamber inlet flow paths as identified in Figure 7.1. In one inlet, particle seeded air for PIV is supplied from compressed air which flows through an atomizer containing a reservoir of olive oil. The other inlet supplies dry compressed air from gas cylinders at the flow rates required to maintain steady venting. The test apparatus is centered around a 74.3 L stilling chamber which allows precise measurement of stagnation properties, mixing between both inlet flows, and allows for a simple and short flow path for the accelerated flow to pass through before exiting the fixture. Throughout the test apparatus, care is made to minimize the length of tubing to minimize frictional losses which allows the assumption of isentropic flow to remain accurate. The stilling chamber dry air inlet and venting outlet use high flow coefficient ball valves to minimize frictional losses as well. All cross sections are much larger than the opening area of a typical 18650 vent cap to ensure that flow is choked at the exit of the vent itself, and all orifice plates have opening areas smaller than the typical 18650 vent.

Dry air is supplied to the stilling chamber separately from the particle seeded flow because of the relatively high flow rates required for steady operation. Compressed air is used in testing to minimize cost and health considerations while still simulating the fluid dynamics of battery venting. A low humidity supply is used as initial testing with compressed, un-dried air showed a tendency for water to freeze at the vent cap openings due to the drop in temperature as the gas is accelerated. To achieve the desired flow rates through a single pressure regulator, high pressure gas cylinders are used. Supply pressure effect, where regulator

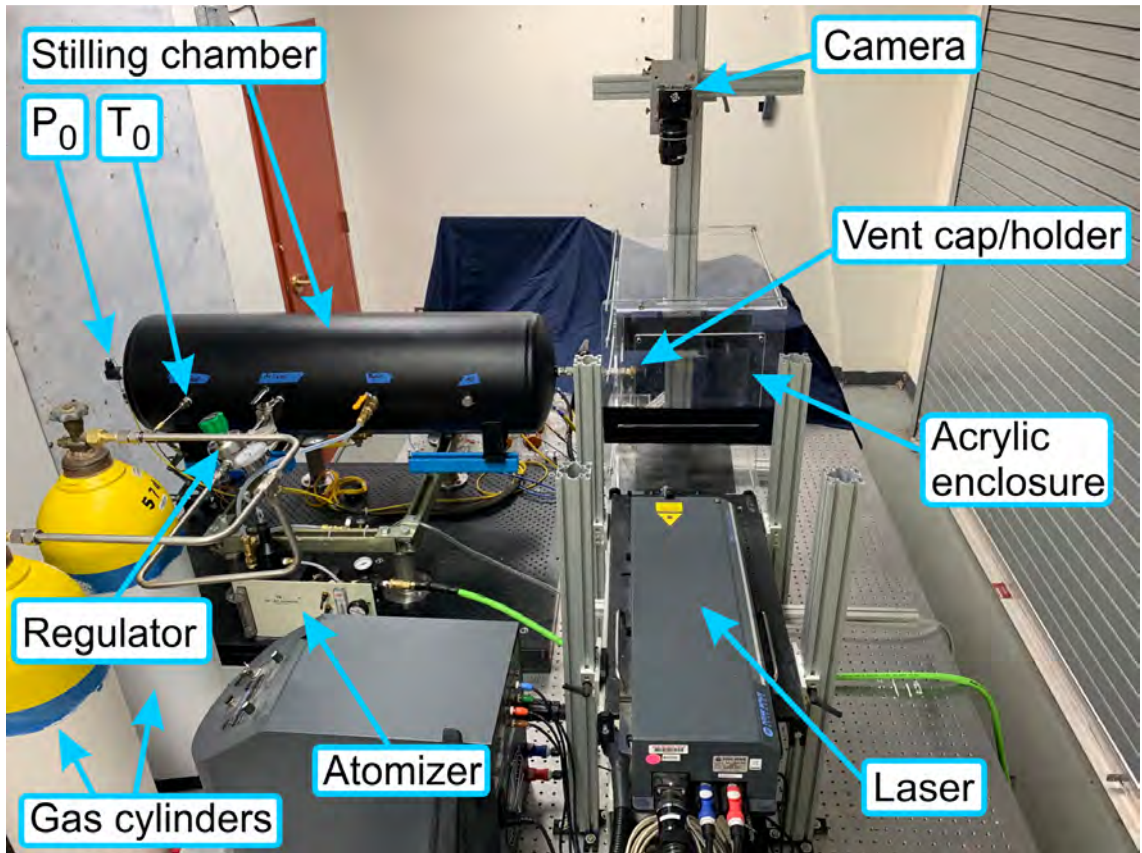


Figure 7.1: Annotated image of laboratory setup for steady state PIV measurement of venting flow.

output pressure increases as upstream pressure decreases, is reduced by using a manifold of two K-size gas cylinders each with an internal volume of 49.9 L.

Since gas flow must be able to be supplied at various pressures to accurately represent battery venting, a pressure regulator was specified to meet the flow rate requirements without itself choking the flow. An upper limit to system flow rate demands was calculated with isentropic flow relations. Opening areas considered include the mean, minimum, and maximum seen in previous Material Technology International Corporation (MTI) brand vent cap testing with values of 8.967 mm², 7.845 mm², and 9.773 mm² respectively. Stagnation temperature was 20 °C, and atmospheric pressure was 86 kPa measured at the laboratory located at a 1,400 m elevation. A Swagelok high sensitivity, high flow rate regulator (model KHF1FRF818A20000) with a 0 kPa to 689 kPa control range was used in these experiments. Figure 7.2 shows the system requirements at various stagnation pressure set points (within the stilling tank) compared to the maximum possible flow rate through the regulator with an upstream gas cylinder pressure of 3.45 MPa or higher. Per the manufacturer datasheet, maximum flow rates were interpolated between known points [94]. At stagnation pressure ratios greater than 1.2, the regulator will not choke the flow. However, lower stagnation pressures cause the regulator to choke before enough flow is supplied to the stilling chamber. At lower, unchoked stagnation pressures a different two-stage pressure regulator (Swagelok model KCY1DRF412A0000) was used for more precise control and to avoid lock up issues associated with the lower flow rates.

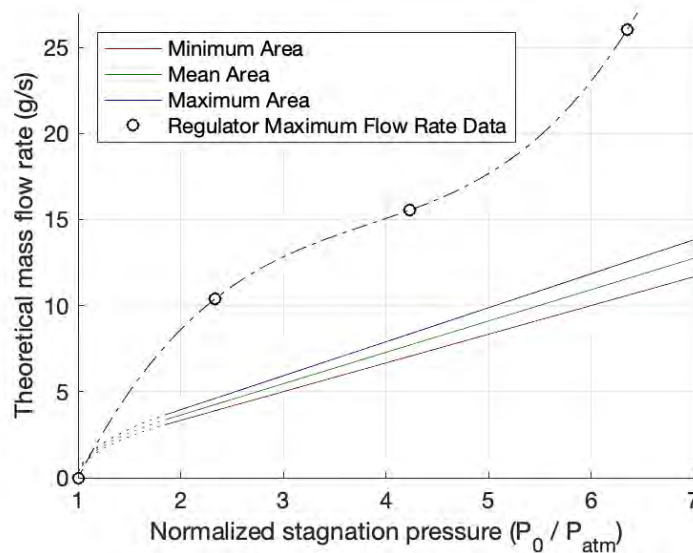


Figure 7.2: Flow rate requirements for steady state venting as a function of normalized stagnation pressure.

To demonstrate the steady state capability of the test apparatus, Figure 7.3 shows a plot of stagnation pressure versus time. Both dry air and particle laden

streams were simultaneously run through an MTI brand vent cap. After opening the outlet valve on the stilling tank, steady state venting was achieved after 35 s. Over the 35.8 s duration of the steady state venting, a mean absolute stagnation pressure of 261.6 kPa was recorded with a standard deviation of 0.20 kPa. Small steps in pressure of around 0.35 kPa, distinctly larger than the measurement resolution, are noticed to occur every 5 to 10 s, but these are negligible when compared to the standard deviation of the pressure measurements. Further, no pressure change from the initial 10.3 MPa was discernible on the analog pressure gauge attached to the compressed air cylinders. Due to supply pressure effect, the regulator outlet pressure increases as the upstream pressure reservoir in the compressed gas cylinders is depleted. This causes stagnation pressure to increase by approximately 1.75 Pa/s as determined by a linear regression fit to the pressure data. The rate of stagnation pressure increase is insignificant compared to the standard deviation in the data. Of note, this rate is ultimately a function of regulator set point, flow rate, and gas cylinder pressure.

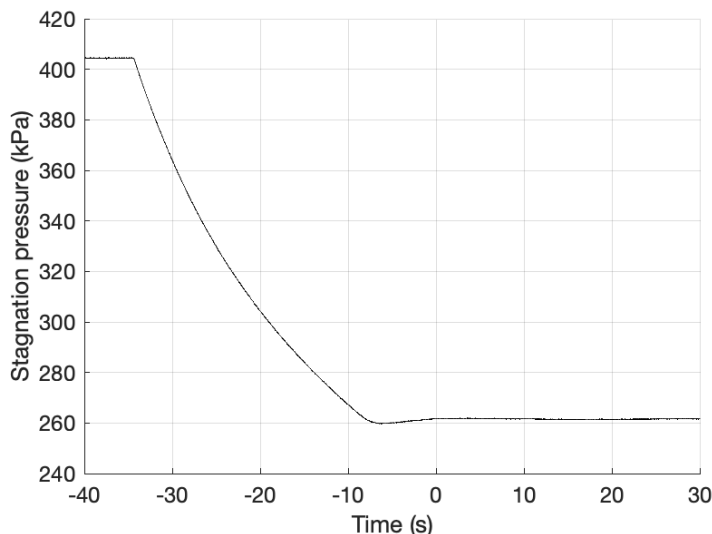


Figure 7.3: Stagnation pressure versus time from the experiment measuring the steady state gas venting. After $t = 0$ the flow was steady.

Ample particle seeding is necessary for PIV measurements. The stilling chamber is continuously supplied with particles during venting. The environment surrounding the vent cap was also seeded with tracer particles to aid velocity measurements near the periphery of the flow. Seeding in the environment prior to each trial allows for measurements of entrained flow and provides better visualization of the edges of the gas jets. Environment seeding is performed with a flexible tube connected off of a Tee fitting from the main droplet supply to the stilling chamber. This particle flow is selectable with a ball valve, and a needle valve allows variable flow rate.

Olive oil droplets are chosen as the seed particles for battery venting ex-

periments because of their low Stokes number, favorable light scattering, and lack of health hazards after test operator inhalation. The Stokes number for the particles in the flow is:

$$\text{Stk} = \frac{\rho_p d_p^2 U}{18\mu L} \quad (7.1)$$

The olive oil droplets have a density (ρ_p) of 0.911 g/mL and diameter (d_p) of approximately 1 μm , resulting in a Stokes number of 0.56 at the sonic vent cap exit which implies a velocity measurement uncertainty of approximately 6% [68]. As the flow decelerates further from the vent cap exit, the accuracy of this tracking is expected to increase significantly because the free-stream velocity decreases, thus decreasing the local Stokes number. The orifice Stokes number calculated here uses an opening diameter as the length scale to describe a turbulent jet. Since there are four openings in the positive terminal of an 18650 vent cap, the jet diameter is taken to be 1.69 mm, which is calculated for a circle with an area equivalent to one fourth of the mean opening (8.97 mm²) of an MTI brand vent.

Droplets are formed via atomization using a Thermo-Systems Engineering Co. (TSI) Model 9306 atomizer. This atomizer implements six selectable liquid jets which are impinged by a high velocity air jet. Droplets are formed when the liquid is then impacted against a spherical impactor [95]. This atomizer features air pressure regulation and dilution. Dilution is typically adjusted between 5 and 10 L/min. The pressure is regulated to a maximum gauge pressure of 320 kPa. This pressure setting provides the upper limit of the steady state venting experiments as stagnation pressure within the stilling tank must be lower than the atomizer outlet pressure to ensure continuous seeding. The atomizer has been modified here with a plug blocking the typical output in favor of using an adjacent fill port with NPT threading to simplify piping connections. This modification allows the atomizer to be used in this pressurized system which is not possible in the factory configuration.

An acrylic enclosure has been fabricated to contain the venting flow and the dispersal of the olive oil droplets. This enclosure also assists in minimizing unintended flow fields caused by drafts or heating, ventilation, and air conditioning flows in the laboratory. Shown in Figure 7.4(a), the acrylic PIV enclosure is 533 mm tall, 537 mm wide, and 349 mm in the vent's axial direction. The enclosure is sized specifically to not interfere with the venting flow using a 21° center-line projection angle and 12° spreading angle. These angles were measured with high speed schlieren imaging and are further discussed in the results portions of this document. A slit is incorporated into the side of the enclosure to allow the laser sheet illumination to pass into the enclosure with no distortion. Black velvet flocking material within the enclosure minimizes laser sheet reflections. Height and tilt adjustments are incorporated into the design of the enclosure for alignment with the vent cap and laser sheet. Both the anticipated venting regions and the location of the laser sheet are shown in Figure 7.4(b). On the far side of

the enclosure from the vent cap, a 457 mm duct directs vented air and droplets through an external door of the building.

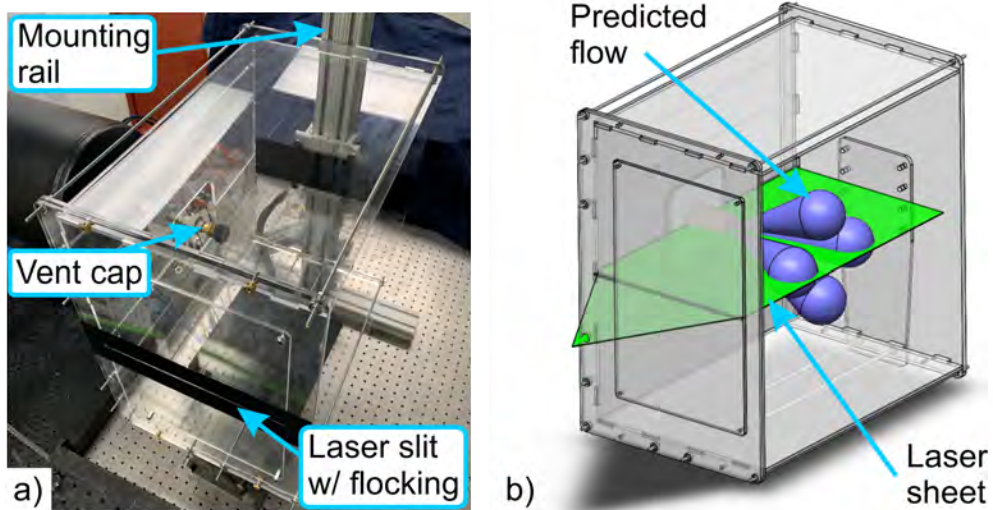


Figure 7.4: (a) Acrylic PIV enclosure installed in the laboratory, and (b) model of the enclosure showing anticipated cones of venting flow (blue) and laser sheet (green).

The vent cap holder from the aforementioned burst imaging experiments is designed to be installed on the steady flow test apparatus, and benefits from the minimally obstructed field of view from Figure 5.2 remain the same. The vent cap holder can be observed, installed on the steady state PIV fixture, in Figure 7.5. Unlike the burst tests, vent caps used in steady state PIV experiments are already burst. As such, care is taken to select vent caps with the desired combination of opening area and discharge coefficient values [78].

7.2 Modular orifice plate holder and series of two jet geometries

The PIV results presented in Chapter 9 implement a series of orifice plates to generate jet flow rather than a pre-burst battery vent mechanism to more generally characterize the combined flow field of two nearby angled jets. The orifice plate holder shown in Figure 7.6(a) is installed on the outlet of the stilling chamber in lieu of the vent holder seen in Figure 7.5. Each orifice plate has a unique geometry defined by the offset angle (θ) and orifice spacing to diameter ratio (D/a) with these dimensions shown on an orifice plate with twist drills inserted into each jet orifice in Figure 7.6(b). Orifice plates were machined in a series of offset angles and spacings listed in Table 7.1 which reports nominal values as well as measurements made on orifice plates after machining to demonstrate the

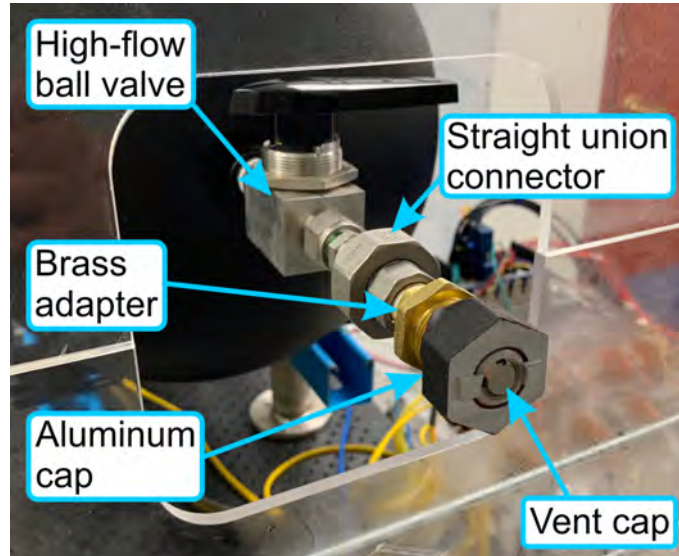


Figure 7.5: Vent cap holder installed on steady state PIV test fixture.

accuracy of the machining. With the exception of one 1.70 mm diameter single jet plate used as a baseline experiment, each orifice plate was machined with two circular orifices with diameters (a) of 1.70 mm. A three orifice diameter long circular flow path connects each orifice to an internal plenum which matches the cross section of the upstream orifice plate holder. A short internal flow path was chosen to minimize any boundary layer growth inside these internal channels while leaving enough thickness for the orifice plate to be mechanically robust. Each jet orifice and the corresponding interior flow path was machined with a Number 51 twist drill, and all sharp, machined edges were left intact. Orifice plates were attached to the test apparatus with four machine screws, and the system was sealed with a laser cut silicone gasket. Washers on each screw between the plate holder and the back side of the orifice plate provided a physical stop for consistent gasket compression and plate alignment with the remainder of the experimental setup. The jet interaction study was limited to two jet configurations rather than the four jets seen on battery vents to provide a more simplified scenario which is more appropriately captured with the light sheet illumination shown in Figure 7.4(b).

Of note, the orifice diameter was chosen to match the opening area of one of the four jets present on an 18650 format battery vent. Vent mechanisms from these batteries have a spacing of approximately six diameters ($D/a = 6$), and an offset angle close to 40° . The orifice plates listed in Table 7.1 explore the effect of increased or decreased spacing and the effect of smaller offset angles. Offset angles up to 40° are not reported because initial investigation showed no interaction at such a large offset angle, and no interaction is predicted at all of the 30° examples as explained in Chapter 8.

The orifice holder has a large flow path with gradual cross section changes

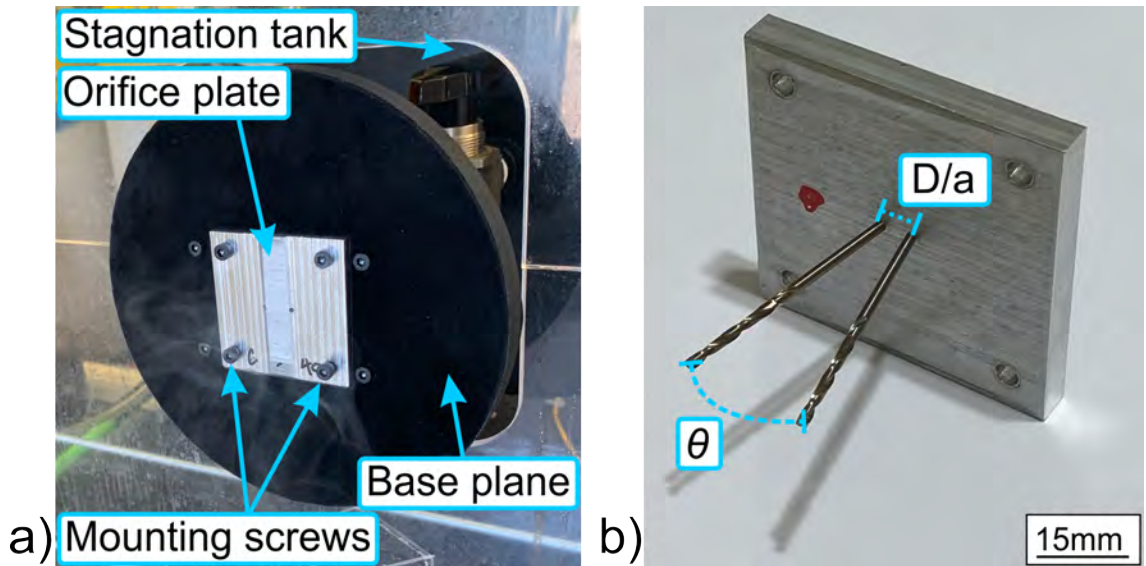


Figure 7.6: Annotated images of (a) the orifice plate holder installed in the laboratory and (b) an orifice plate with two twist drills inserted into the plate's openings to show the jet spacing (D/a) and offset angle (θ).

Table 7.1: Two jet orifice plate configurations

Nominal spacing D/a	Nominal offset angle θ	Measured spacing D/a	Measured offset angle θ
3	0	3.05	-0.02
3	10	3.06	10.4
3	20	3.01	19.8
3	30	2.99	29.7
6	0	6.05	-0.06
6	10	6.04	10.1
6	20	6.01	19.8
6	30	5.97	29.5
12	0	12.01	-0.22
12	10	12.00	9.91
12	20	12.04	20.0
12	30	12.04	Not measured

prior to the orifice plate exit to minimize losses. The base plane of the orifice plates were extended with a large, circular piece of laser cut acrylic covered in black velvet material to minimize laser reflection. The additional base plane is used to limit the effects of any entrainment through the back of the acrylic PIV enclosure near the jet orifices. Upstream, a reusable steel compression fitting allowed the holder to be mounted at any angle. This allowed the center of each jet to be aligned with the plane of the laser sheet illumination.

7.3 PIV imaging equipment and software

Particles were illuminated by a laser sheet to image an isolated plane within the flow. By imaging a single plane through the middle of the venting flow, a cross section of two of the four total jets can be measured, and the remainder of the flow field can be described through symmetry arguments. The laser sheet was created by optics incorporated into a New Wave Research Solo 200XT-15Hz neodymium-doped yttrium aluminum garnet (Nd:YAG) laser. This unit produces illumination in pulsed pairs from its two laser heads at 532 nm, with up to 15 Hz repetition rate for the pulse pairs. The laser beam has a diameter of 6 mm which is spread into a 6 mm thick sheet. Each laser pulse has duration between 3 ns and 5 ns with an energy up to 200 mJ. The two laser heads are set to separate powers to allow for equivalent intensity between images within a pair due to how the camera shuttering function. The laser unit was mounted on a height adjustable platform for alignment with the vent cap holder. The laser's power, control, and water cooling unit was placed adjacent to the platform.

All images were recorded with a TSI Powerview 690090 4MP-LS PIV camera with a resolution of 2,352 by 1,768 px. Images were recorded in 12-bit grayscale. While the cameras maximum frame rate was 126 Hz, the maximum realizable rate when connected to the other components in the system was approximately 11 Hz. A Nikon Micro-Nikkor 55 mm fixed focal length lens was used as it allowed an appropriate field of view with its ability to focus on objects as close as 0.25 m. This lens has aperture settings between $f/2.8$ and $f/32$, but most images were recorded at $f/4$. The camera was mounted on the same 80/20-brand aluminum extrusion as the acrylic enclosure with adjustments in three directions to give precise alignment with the vent cap. The camera itself was mounted on an aluminum plate connected to four optical rods which kept the camera square to the vent cap and acrylic enclosure.

All image recording and PIV processing was performed with TSI Insight 4G software. Images were recorded as a fixed sequence in a synchronized exposure mode. Sequences of one thousand pairs were recorded once steady state venting was confirmed via a stable stagnation pressure measurement. Increasing the number of frames recorded in a sequence uses a significant amount of compressed air, but also provides more confidence on mean velocity and turbulence calculations. Triggering was performed within the Insight 4G software. Image

pairs were recorded with laser pulses straddling the downtime between the exposures. Laser pulse time delay is used to set the time offset between frames rather than the camera because it allows more precise control. The time offsets between paired images was always 1 μ s.

Various processing methods were explored to minimize erroneous velocity measurements including varying the interrogation window size, pre-processing methods, and post-processing vector filling and conditioning. When processing images, a region of interest was defined to include the entire flow field as shown in Figure 7.7. The PIV region of interest used in all experiments was 1,728 px tall by 1,728 wide. A calibration image was taken with an orifice plate installed, and the jet orifices were used for alignment and as fiducial markings. The spatial relationship between pixels in the image and length was 20.3 px/mm, and the entire PIV region of interest was an 84.9 mm square. The darker region near the jet orifices is attributed to less effective environmental particle seeding and minor camera sensor damage. The pre-processing method used was a local median filter with a 3 px square filter to remove some image noise. PIV analysis was performed with a recursive Nyquist method which began with an interrogation window of 80 px by 80 px during the initial pass which was gradually decreased to a final window of 24 px by 124 px for the final pass. This recursive method generally provided less rejected velocity measurements than a single pass method. After iterating between various methods, a multi-step post-processing method consisting of an initial local vector validation followed by local median and local mean hole filling methods for locations in each image pair where a velocity vector could not be calculated during the PIV processing. After processing was completed, the analysis files saved by Insight 4G were imported into MATLAB for further analysis.

7.4 Stagnation pressure and temperature data acquisition

Figure 7.8 shows the National Instruments (NI) data acquisition system installed on a laser cut acrylic sheet located in close proximity to the PIV setup. Nearby DIN rails with Wago brand connectors are used for direct current power distribution, construction of the small current-to-voltage measurement circuits, and strain relief.

All reported stagnation pressure data was measured with a Wika model A10 pressure transducer with a measurement range of 0 MPa to 345 kPa. The pressure transducer was powered with a fixed 12 V_{DC} supply, and the nominal 4 mA to 20 mA output was converted to a voltage signal by measuring the voltage drop across a 468.5 Ω resistor. This allowed the voltage measurements to be scaled linearly between 1.87 V and 9.37 V. Voltage was measured by a NI 9205 card installed in an eight-slot 9188 cDAQ chassis located adjacent to the stilling chamber. This card was configured to measure analog voltages between -10 V and 10 V with 16-bit precision. The pressure-via-voltage measurement was made

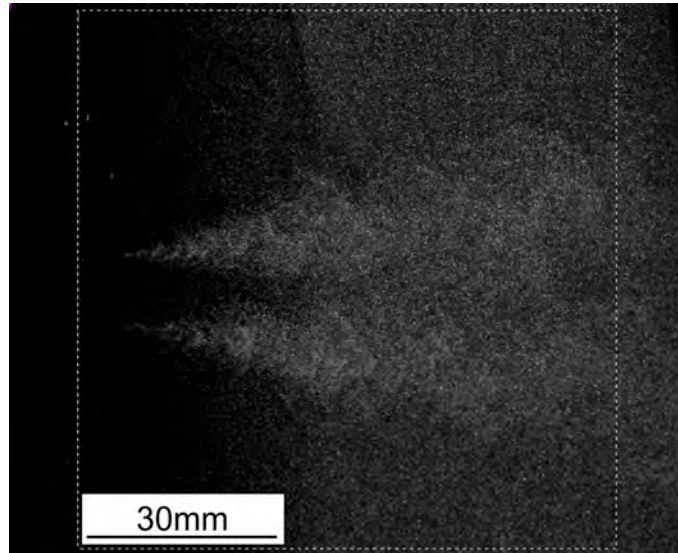


Figure 7.7: A sample PIV image of two jets interacting with the computational region of interest showed as a white dashed line.

at a rate of 100 Hz during all testing. Initiation of data acquisition and live monitoring of the pressure transducer reading was performed via a LabVIEW program run on a desktop computer and written specifically for the testing.

Current-to-gage-pressure calibrations were provided by the manufacturer at 0.000 MPa, 1.724 MPa, and 3.447 MPa with 7 Pa precision. A linear regression of these provided values was used in data processing. The resistance of the 468.5 Ω resistors used to convert between current output and an analog voltage measurement are measured with a Fluke 115 multimeter to 0.1 Ω resolution. Additionally, analog dial pressure gauges are installed on the upstream pressure regulator for test operator confirmation during testing. Utilizing factory calibrations allows a degree of confidence in measurement accuracy. Periodic reconfirmation of instrumentation calibration is necessary to avoid measurement bias.

Temperature is measured directly by a NI 9212 card with internal cold junction compensation, and the thermocouple lines have been shielded to minimize signal noise caused by nearby equipment. Data acquisition rates for temperature was 10 Hz. The NI thermocouple card uses the initial manufacturer calibration. Individual thermocouple calibration is not performed, but an additional exposed junction, K-type thermocouple probe is used to measure room temperature throughout testing and is confirmed against an Extech SD700 portable weather station.

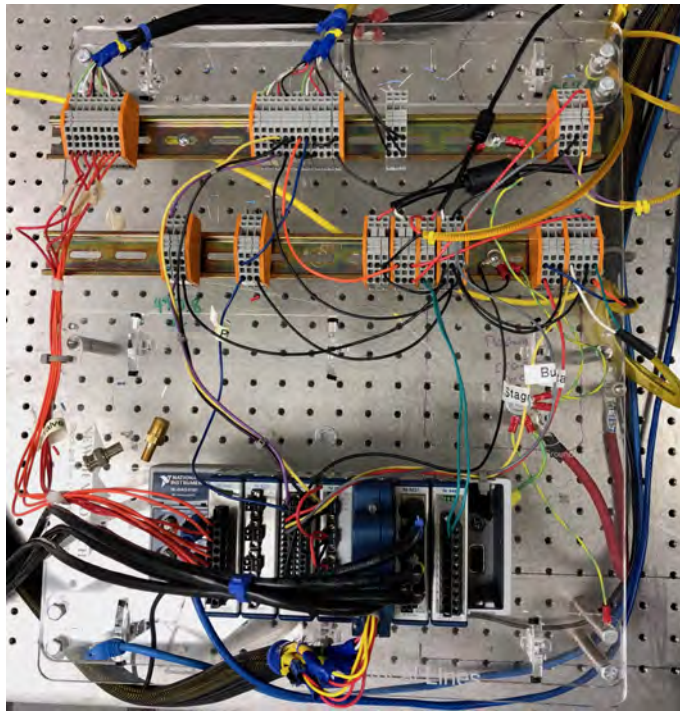


Figure 7.8: The National Instruments cDAQ 9188 installed in the laboratory.

CHAPTER 8

PREDICTING JET INTERACTION WITH A SEMI-ANALYTICAL MEAN VELOCITY FIELD MODEL

8.1 The single jet mean flow field

The mean streamwise velocity profile for an incompressible jet is self-similar where the maximum local velocity (u_{pj}) continuously varies towards zero symmetrically on either side. The mean jet velocity profile is defined as a function of a location parameter (η) as [1]:

$$\frac{u_j}{u_{pj}} = \left(C_0 + C_2\eta^2 + C_4\eta^4 \right) e^{-A\eta^2} \quad (8.1)$$

The velocity u_j is in the streamwise direction, and there is no velocity defined in the spanwise direction as it is assumed to be negligible. This velocity profile is plotted in Figure 8.1(a), and a schematic representation of jet geometry and important velocities is shown in Figure 8.1(c). The non-dimensional location parameter (η) is calculated from streamwise (s) and spanwise (r) coordinates as:

$$\eta = \frac{r}{s - s_0} \quad (8.2)$$

The parameter s_0 is referred to as the “virtual origin.” Equation 8.1 defines the velocity profile originating and spreading from a point, but the jet must have some width in the near field due to the geometric configuration of the jet orifice. The virtual origin parameter is thus used to tune the jet profile to match the flow configuration of interest.

The constants in Equation 8.1 were determined experimentally via laser doppler anemometry and are listed in Table 8.1 [1]. Slight changes in these constants exist when Hussein et. al. reexamined the same jet with hot wire anemometry and identified slightly different parameter values, demonstrating the experimental rather than analytical origin of these constants [1].

The local jet velocity (u_j) is defined in relation to a local peak velocity (u_{pj}) which itself decays downstream as a function of the streamwise coordinate (s) from the initial exit velocity of the jet (U_j) through the relationship:

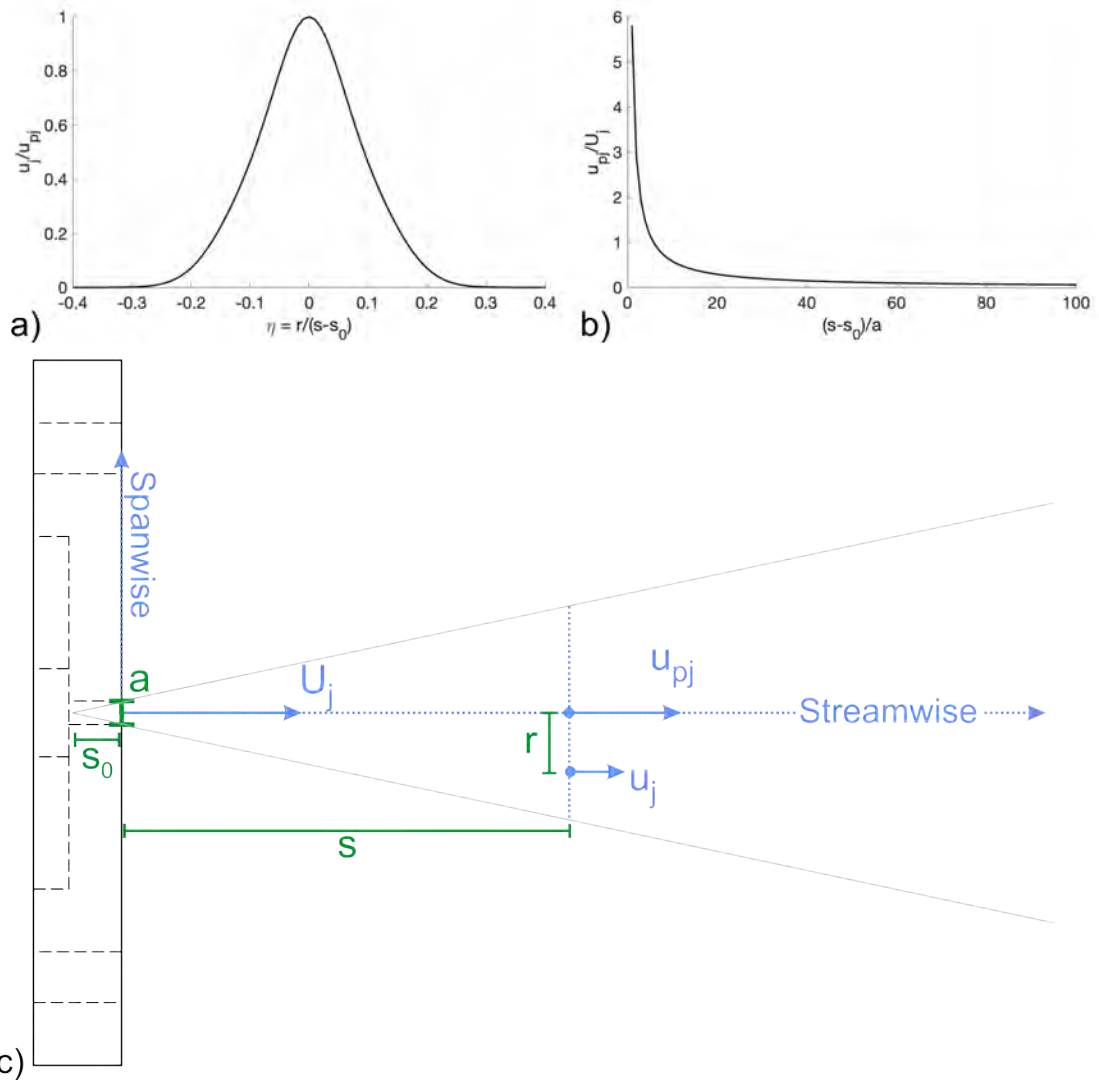


Figure 8.1: (a) Streamwise velocity normalized by the local peak velocity as a function of the location parameter (η) as calculated from Equation 8.1, (b) local peak velocity decay downstream normalized by exit velocity as calculated with Equation 8.3, and (c) a schematic representation of geometry and specifically named velocities.

Table 8.1: Experimentally determined constants used in Equation 8.1 [1]

Parameter	Value (unitless)
C_0	1.000
C_2	1.212×10^1
C_4	2.815×10^3
A	111

$$\frac{u_{pj}}{U_j} = \frac{B}{(s - s_0)/a} \quad (8.3)$$

From Equation 8.3, the magnitude of the local velocity peak is inversely proportional to the downstream distance. The constant B has been measured experimentally through multiple methods to an approximate value of 5.8, and this parameter has been noted to be independent of Reynolds number [52]. Therefore, the velocity decay and the shape of the spanwise velocity profile are independent of the fluid used and the velocity of the jet. The velocity decay quantified in Equation 8.3 can be represented graphically in Figure 8.1(b).

While the spanwise velocity profile is defined self-similarly for all downstream locations, the velocity profile does evolve from a near constant profile to the self-similar profile within a short region adjacent to the orifice. Notably, this model does not include compressibility effects which may be present in higher velocity gas jets as were generated in this study. To account for both compressibility and velocity profile evolution, the analysis of experimental results will be limited to downstream regions where the jet velocity profile is established which coincides with lower velocities not associated with compressibility effects. The exit velocity of jets (U_j) will be optimized along with the virtual origin location (s_0) to best match the experimentally observed velocity profiles.

8.2 Particle Image Velocimetry (PIV) results from a single jet to inform scenario-specific model constants

A PIV trial was performed with a single jet orifice plate which was fabricated in a similar manner to the angled jet pairs as described in Chapter 7. The single jet orifice plate was used to generate a jet through a 1.70 mm diameter circular opening and the stagnation pressure to atmospheric pressure ratio generating the flow had a measured value of 1.494 (to match the trials discussed in Chapter 9). From isentropic flow relationships, the jet exit velocity (U_j) was calculated to be 256 m/s. One thousand image pairs were recorded with a time delay of 1 μ s, and the mean velocity field in the axial direction (aligned with the streamwise coordinate in this circumstance) is mapped in Figure 8.2(a).

Virtual origin location (s_0) and velocity decay (B) constants were optimized to minimize the difference between the single jet baseline experiment PIV data and the corresponding predicted velocity field.

The predicted velocity field was calculated in the same domain as the PIV region of interest, and the difference between the two velocity fields was evaluated over a point grid in this domain with spacing of 0.1 orifice diameters. The difference between the experimental and predicted velocity was evaluated at each point on this grid, the difference was squared, and then each squared difference was summed to provide a single value to characterize how well the

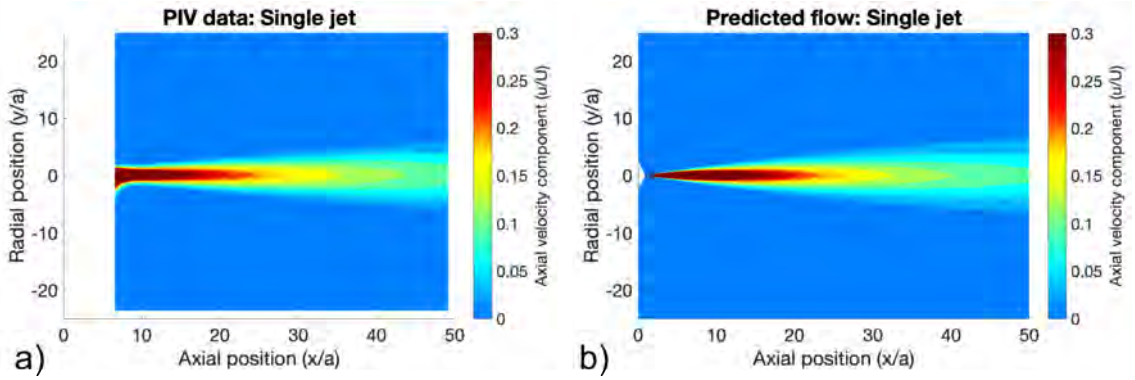


Figure 8.2: (a) Experimental velocity field PIV measurements for a single jet and (b) predicted velocity field for a single jet with optimized model constants.

prediction matched the experimental data. Squaring the velocity difference at individual points was performed to bias the optimization towards matching higher velocity regions of the flow. The virtual origin location (s_0/a) and velocity decay constant (B) were optimized to dimensionless values of 0.89 and 4.70 respectively. As shown in Figure 8.2(b), the predicted flow field contour resembles the measured flow field from Figure 8.2(a). Velocity profiles extracted at various downstream (x/a) locations in Figure 8.3 show close agreement. The somewhat counterintuitive values for these constants, particularly the virtual origin being downstream of the actual jet orifice, is attributed to the varying jet velocity profile and compressibility effects in the region of the flow closest to the orifice. The high velocity jet near the orifice retains its velocity better than a jet with a fully self similar velocity profile and does not begin to spread as quickly, which pushes the virtual origin downstream beyond the jet orifice. The velocity decay constant is slightly lower than the typical value of 5.8.

8.3 Combining multiple single jet profiles to predict multiple jet flow

Here, understanding of the single jet velocity profile as established in literature is utilized to extend basic science understanding of jet flows into a characterization of the combined flow and interaction of two, nearby jets. Considering jets without compressibility, interaction ultimately becomes a process where the local velocity in the region between the jets must increase to accommodate the necessary mass flow rate. The multiple jet flow field model developed here assumes superposition of the velocities from two independently defined jets. For outwardly oriented jets, the geometric parameters which characterize each unique scenario are the jet spacing (D) and the projection angle between the centerlines of the jets (θ). This is schematically represented in Figure 8.4. Parallel interacting jets are the case if the projection angle is zero which has been studied in the literature [53] [55]. All coordinate dimensions and the distance between

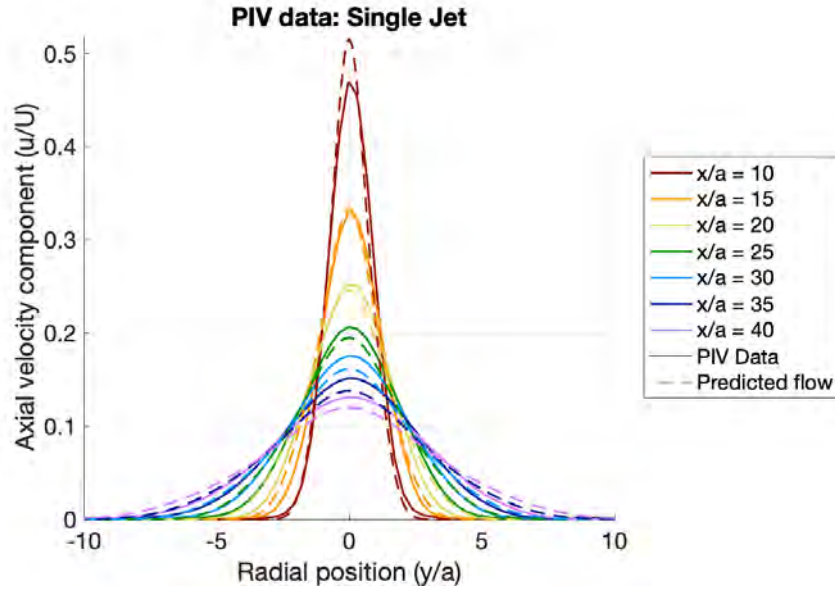


Figure 8.3: A comparison of experimental versus predicted flow at various downstream distances.

the jet orifices in this section are reported after non-dimensionalization by the jet orifice diameter a is conventional in the literature [52].

The two main coordinate systems of interest represented in this flow as represented in Figure 8.4 are the jet-centric and global axes. The jet-centric axes have previously been implemented in Section 8.1 which are referred to as stream-wise (s coordinate) and spanwise (r coordinate) where the former is in the direction of the flow. Velocities in the jet-centric coordinate system are given subscripts of j . The axes in the global coordinate system are referred to as axial (x coordinate) and radial (y coordinate) to align with tradition jet flow axes. Velocities in the global coordinate system are locally referred to as u and v in the axial and radial directions respectively. The jet-centric coordinates are important for defining each jet based on the mean velocity profile presented in the literature, and the global coordinates provide a means for evaluating the entire flow and align with the PIV measurements recorded in experiments.

Since each jet is defined independently when making the total flow field prediction, there must be a jet-centric set of axes defined for each jet to define its contribution to the combined velocity field. Referencing the angled jets issuing roughly from left to right in Figure 8.4, the upper jet will be given the subscript 1 while the lower jet will be given subscript 2. To arrive at the upper jet-centric coordinates from the global coordinates, a vertical transformation of $D/2a$ and a counterclockwise transformation through an angle of $\theta/2$ must be applied. This transformation may be written as:

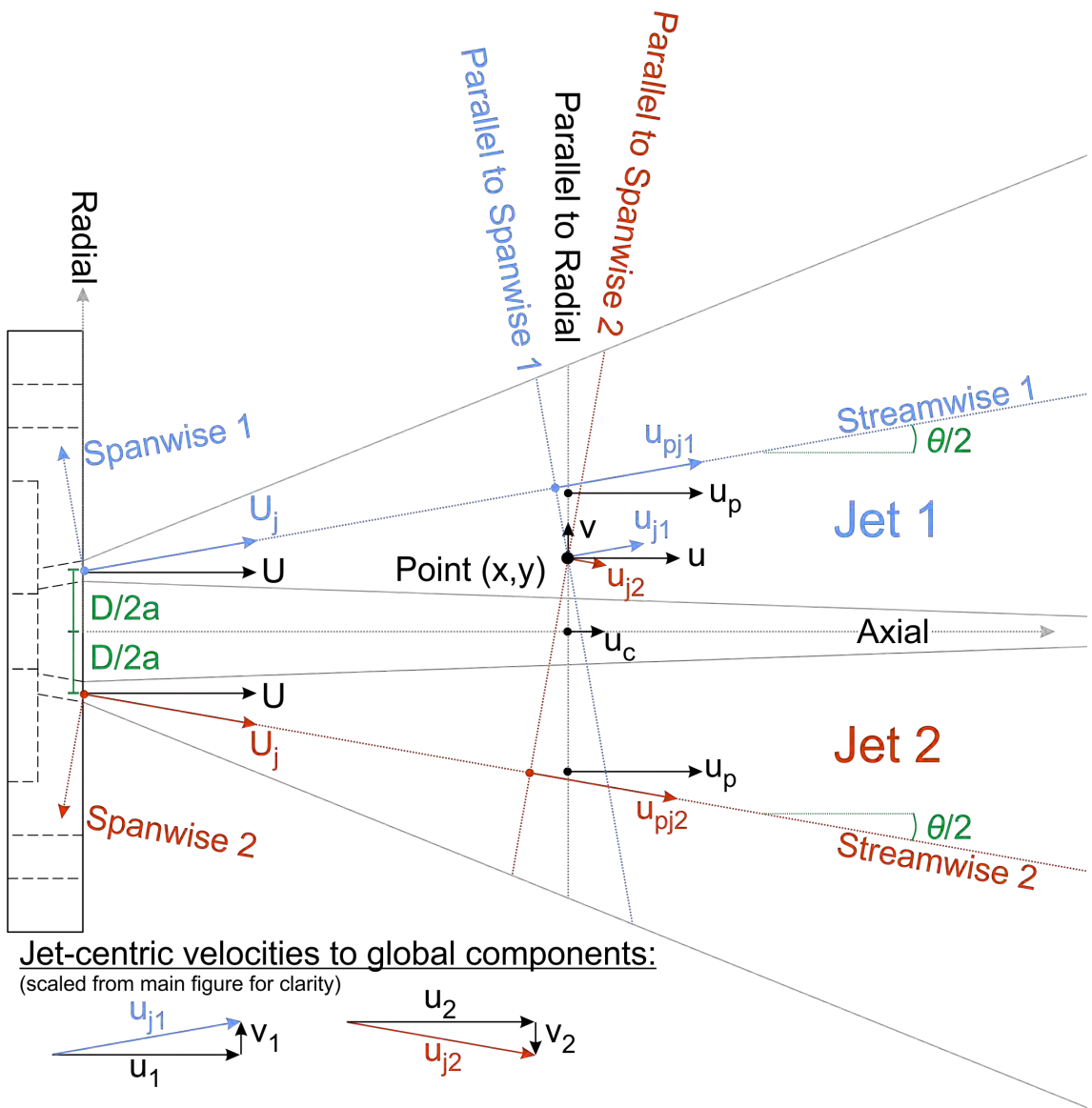


Figure 8.4: Annotated two jet flow field schematic with coordinate systems and applicable velocities.

$$\begin{aligned}
s_1 &= x \cos\left(\frac{\theta}{2}\right) - \left(y + \frac{D}{2a}\right) \sin\left(\frac{\theta}{2}\right) \\
r_1 &= x \sin\left(\frac{\theta}{2}\right) + \left(y + \frac{D}{2a}\right) \cos\left(\frac{\theta}{2}\right)
\end{aligned} \tag{8.4}$$

Similarly arriving at the lower jet-centric coordinates from the global coordinates, requires a vertical transformation of $-D/2a$ and a clockwise transformation through an angle of $\theta/2$. This transformation may be written as:

$$\begin{aligned}
s_2 &= x \cos\left(\frac{\theta}{2}\right) + \left(y - \frac{D}{2a}\right) \sin\left(\frac{\theta}{2}\right) \\
r_2 &= -x \sin\left(\frac{\theta}{2}\right) + \left(y - \frac{D}{2a}\right) \cos\left(\frac{\theta}{2}\right)
\end{aligned} \tag{8.5}$$

From the above coordinate transformations, any location within the global coordinate system (x, y) can be rewritten in the local coordinate systems as (s_1, r_1) or (s_2, r_2) . Using the mean velocity profile discussed in Section 8.1, these two jet-centric locations correspond to local velocities $u_{j,1}$ and $u_{j,2}$. These velocities remain in the direction of their respective jet.

To combine the flow field into a single flow containing both jets, the effects from jets 1 and 2 are combined via superposition of the velocities $u_{j,1}$ and $u_{j,2}$. This approach attempts broadly to approximate conservation of mass by allowing the flow from both jets to pass through each point in the flow field, and jet interaction is manifested as the superposition between the flows. For simplicity, these two values are broken into components aligned with the global coordinate system:

$$u_1 = u_{j,1} \cos\left(\frac{\theta}{2}\right) \quad \text{and} \quad v_1 = u_{j,1} \sin\left(\frac{\theta}{2}\right) \tag{8.6}$$

$$u_2 = u_{j,2} \cos\left(\frac{\theta}{2}\right) \quad \text{and} \quad v_2 = -u_{j,2} \sin\left(\frac{\theta}{2}\right) \tag{8.7}$$

Then the jet specific components $u_1, v_1, u_2,$ and $v_2,$ are summed to form the combined flow velocity components u in the axial direction and v in the radial direction:

$$u = u_1 + u_2 = u_{j,1} \cos\left(\frac{\theta}{2}\right) + u_{j,2} \cos\left(\frac{\theta}{2}\right) \tag{8.8}$$

$$v = v_1 + v_2 = u_{j,1} \sin\left(\frac{\theta}{2}\right) - u_{j,2} \sin\left(\frac{\theta}{2}\right) \quad (8.9)$$

In summation, the combined flow at any given point of two nearby jets at some spacing and outward offset angle is calculated by:

1. Defining the point in global coordinates (x, y)
2. Translating the point into both jet-centric coordinate systems as (s_1, r_1) and (s_2, r_2)
3. Using Equations 8.1, 8.2, and 8.3 to calculate $u_{j,1}$ and $u_{j,2}$
4. Using Equation 8.8 and 8.9 to combine the individual jet contributions into the axial (u) and radial (v) velocity components of the combined field in global coordinates.

8.4 Describing metrics to characterize the intensity of jet interaction in the mean velocity field

Jet interactions can be broadly characterized by the velocity in the center of the combined flow field and the location of the peak velocities when examined on a line parallel to the radial axis as shown in Figure 8.4. The line parallel to the radial axis can be given the equation $x = c$ and can be evaluated for any constant value $c > 0$. The first characteristic is amplified centerline velocity (u_c), and the second characteristic is an inward shift of local peak velocity locations. The local peak velocity (u_p) is defined as the maximum axial velocity along any given line parallel to the radial axis. This peak velocity occurs equally at two locations due to flow field symmetry. Both u_c and u_p are shown in their respective locations in Figure 8.4. The strength of interactions rely on the relative effects of the constructive interference of the two jet velocity profiles against their outward orientation and dissipation of the entire flow field as expressed through velocity decay. The degree to which jet interactions occur are defined by the offset angle ($\theta/2$) and jet spacing (D/a). Jet interactions are only examined here prior to the axial (x) location where $u_p/U > 0.02$. This location corresponds to a local peak axial velocity of approximately 1 m/s in the performed PIV experiments. While some significant interactions may be predicted at very far distances, these predictions hold little applicability in most practical flows.

The first characteristic of interacting jets is an amplified centerline velocity (u_c) due to the superposition of the two jet flows. The centerline velocity is horizontally directed due to the symmetric nature of the jet arrangement, and is defined at a radial location of $y = 0$. While the majority of the flow field decelerates as the jets spread and dissipate, the centerline velocity actually increases for

some values of x/a along the axial axis before decreasing in the far field. Figure 8.5 shows predicted centerline velocity normalized by the axial exit velocity (U) for various jet arrangements.

To characterize relative magnitude of u_c to the flow's cross-section at any axial location, the ratio u_c/u_p is implemented. The centerline to local peak velocity ratio allows for a simple definition of when jet combination occurs. Jet combination is the phenomenon which occurs when interaction is so strong that there are no longer individual local velocity peaks associated with each of the two original jets. When jets combine, the new combined peak velocity exists along the flow's axial centerline. As such, jet combination is noted when $u_c = u_p$, and this can be expressed as the ratio u_c/u_p reaching unity.

While some jet pairs are predicted to combine, this only occurs for jets with a small spacing and limited outward projection angle. To describe if the interaction between the two jets is relatively significant, a threshold value of $u_c/u_p \geq 0.1$ is identified. This threshold value was chosen because it reflects the centerline velocity reaching a magnitude within one order of magnitude of the local peak velocity.

The second characteristic of interacting jets is the tendency for the locations (y_p) where the local peak velocity (u_p) occurs to move closer to the center of the flow rather than maintain trajectories along the streamwise axes. To describe the mechanism behind why the locations of local peak axial velocity are closer than the streamwise axis trajectory, it is useful to consider the contribution of each jet to the combined flow field individually. Considering a single jet, the local peak velocity will always coincide with the jet's own streamwise axis. This trajectory will be maintained throughout the domain. When considering the velocity profile of the second jet near the streamwise axis belonging to the first jet, the second jet's local velocities will always be decreasing away from the second jets streamwise axis. Therefore, the velocity contribution from the second jet will be greater on the side of the first jet's streamwise axis which is closer to the center of the flow (near the axial axis). As shown in Figure 8.6, this unequal contribution must shift the peak inwards. The example shown the Figure 8.6 represents significant peak shift, but the shift is more likely less noticeable and even imperceivable in circumstances with large jet offsets.

As previously described, jet combination occurs when two peaks corresponding to the individual jets are no longer perceivable ($y_p = 0$). When u_c/u_p reaches unity, the distance from both local peaks to the central axis (y_p) simultaneously reaches zero. This leads to an appearance that the jets are turning towards each other, but the peak shift and jet merger is truly caused by increasing velocity in the center of the flow due to the velocity superposition. Velocity is directed away from the center of the flow in all locations except the axial axis.

Using the combined flow field approximation developed in Section 8.3, examples of various scenarios which lead to combination, significant interaction, and no appreciable interaction can be demonstrated. Shown in Figure 8.7, combined flow fields were calculated for jets with various offset angles at jet spacings

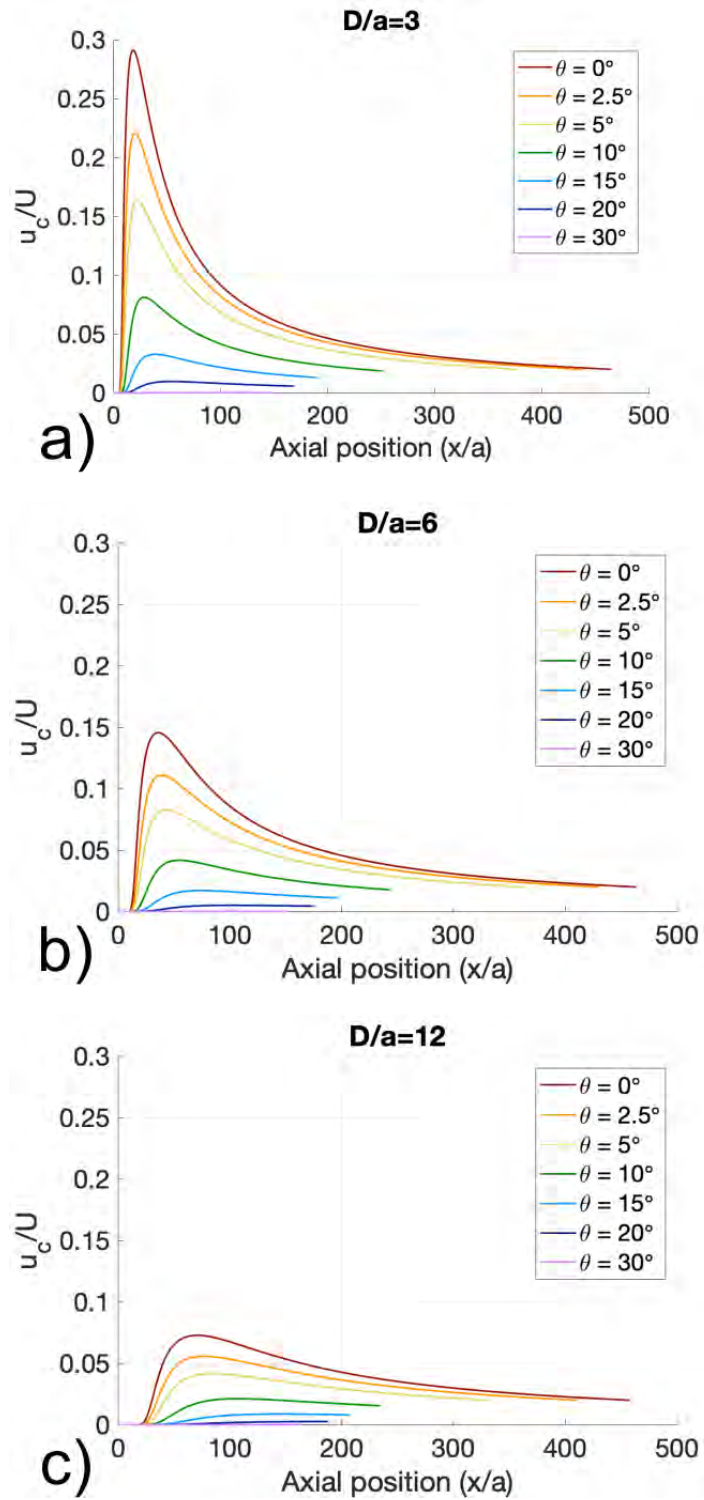


Figure 8.5: (a-c) Centerline velocity versus axial position in combined flow field at various spacings and angles.

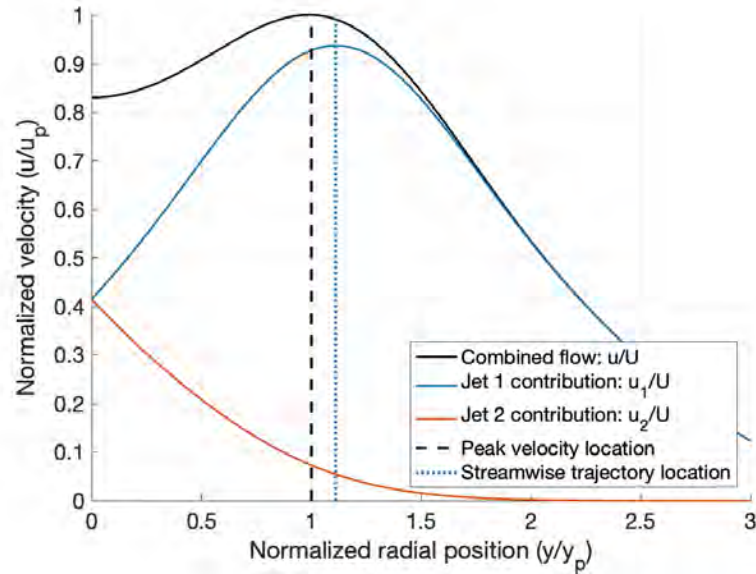


Figure 8.6: Inward shift of peak velocity in combined flow field.

of $D/a = 3, 6,$ and 12 . The plots of centerline to local peak velocity ratio versus axial position demonstrate how increased offset angle at a given spacing always leads to a lower predicted interaction. The plots of the location of the local velocity peak also show how the local velocity peak will pull towards the flow centerline in higher interaction and combination scenarios, but can often follow very closely to the initial streamwise trajectory. In general, less spacing and angle leads to more interaction and likelihood for combination.

8.5 Outwardly oriented gas jet interaction predictions for fabricated orifice plates

As described in Chapter 7, a series of two jet orifice plates were fabricated at spacings of $D/a = 3, 6,$ and 12 and at offset angles of $\theta = 0^\circ, 10^\circ, 20^\circ, 30^\circ,$ and 40° . To predict the expected interaction intensity along with the possibility of jet combination, combined flow fields were computed through a range of jet offsets and separation angles as shown in Figure 8.8, and the location of the fabricated orifice plates are marked with white stars. The axial location (x/a) where significant interaction ($u_c/u_p \geq 0.1$) was first predicted is shown throughout the D/a versus θ parameter space. If the interaction threshold was not reached before the local peak velocity diminished to 2% of the axial component of the exit velocity, then no interaction is reported. Additionally, jet combination is predicted to occur on any geometric configuration in the region below the dashed line near the smallest jet separation and offset values.

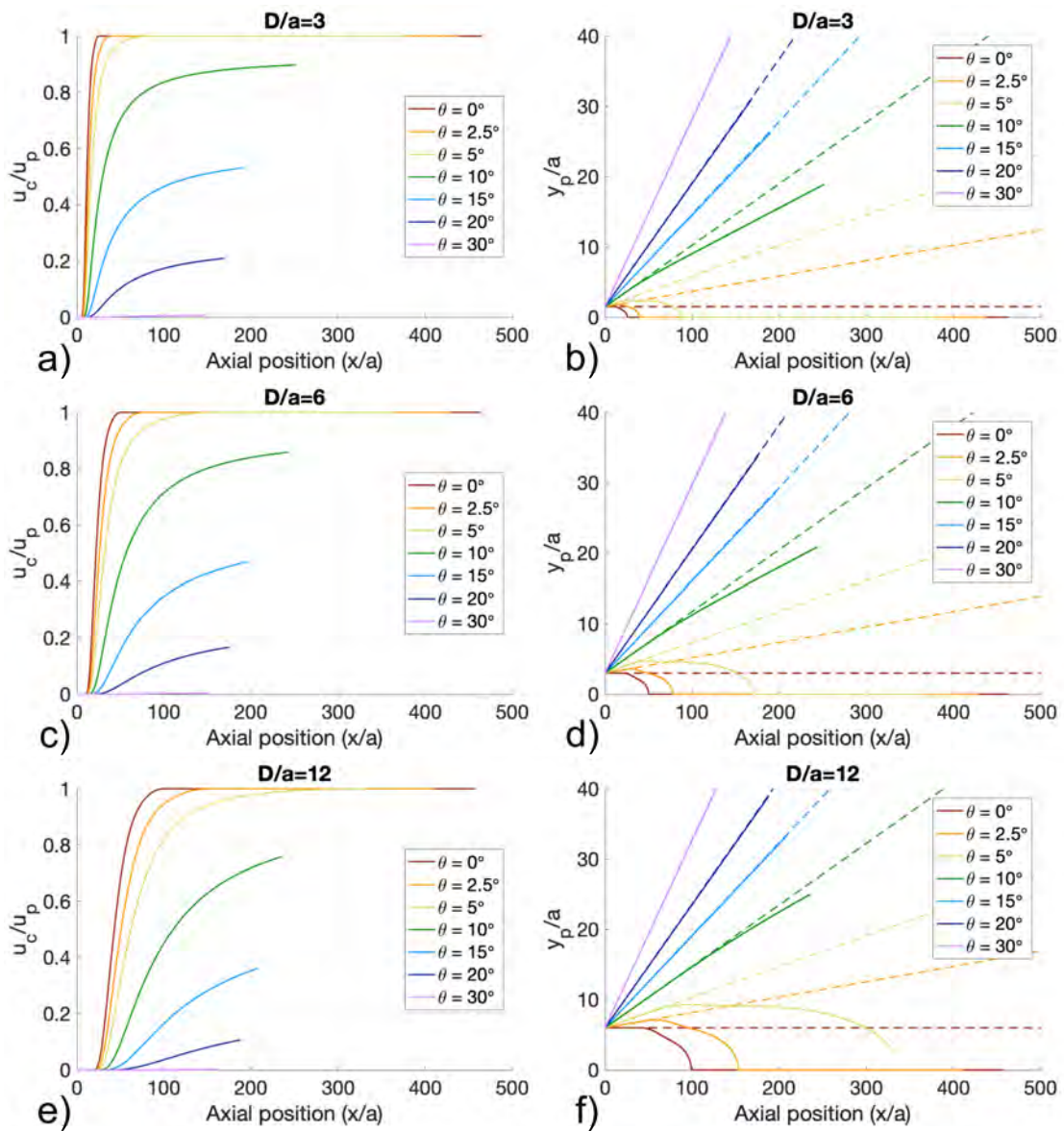


Figure 8.7: (a, c, e) Centerline to local peak velocity ratio versus axial position in combined flow field for various jet spacings and offset angles, and (b, d, f) local peak velocity location (solid lines) versus axial position compared to the streamwise axis trajectory (dashed lines) demonstrating inward peak shift and jet combination.

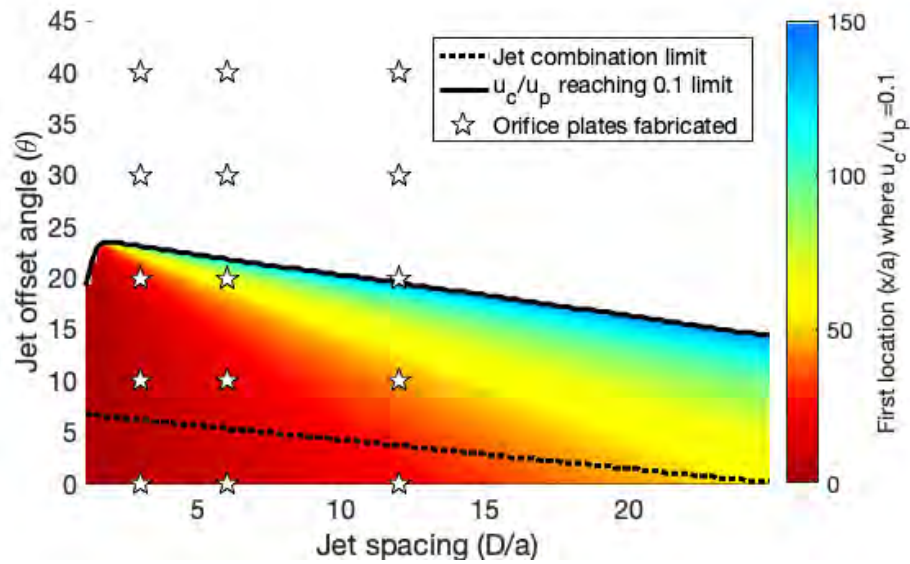


Figure 8.8: Jet interaction map depicting the location of first significant interaction and predicted jet combination region at various combinations of jet spacing and offset angle.

In Figure 8.8, it is clear that jet interaction should increase with decreased jet spacing and offset angle. The axial distance needed for significant jet interaction to occur increases more rapidly with increasing offset angle than increasing orifice separation. Significant interaction is not predicted to exist at offset angles above 23° . Similarly, jet combination appears to only occur at relatively small offset angles below 6.8° . In general, jet interactions are predicted to be more sensitive to changes in offset angle than spacing.

CHAPTER 9

EXPERIMENTAL RESULTS AND DATA ANALYSIS OF STEADY STATE TWO JET VELOCITY FIELDS

Using the previously described steady state venting apparatus with interchangeable orifice plates and the Particle Image Velocimetry (PIV) measurement technique technique was used to conduct experiments to quantify:

- The velocity field for steady-state gas venting flow from multiple outwardly directed gas jets.

Time resolved measurements of two jet configurations of various spacings and offset angles were made to develop a foundational understanding of the jet interactions.

9.1 Steady state PIV test series

Each individual trial was performed with a unique jet configuration, but the jet exit velocity was maintained constant throughout the test series. The stagnation pressure in the upstream stilling chamber was set to 129 kPa for each trial. This gave a stagnation to atmospheric pressure ratio of 1.50. Since the stagnation pressure was not sufficiently large to choke the flow, the jets exited the orifice plate subsonically at atmospheric pressure. The jet exit velocity was calculated as Mach 0.784 or 256 m/s using isentropic flow relationships. The jets were compressible in the region immediately adjacent to the orifice exit. Mean stagnation pressure and temperature measurements were recorded during each trial as recorded in Table 9.1.

One thousand image pairs were recorded during each trial. PIV processing in Insight 4G software calculated instantaneous velocity fields as shown in Figure 9.1 for each frame pair. Due to a lack of sufficient environmental particle seeding and high deformation between particle groups, PIV processing reliability was limited in the region nearest the orifice plate. Velocity fields reported here have been limited to the region beyond 10 diameters from the orifice exit in the axial direction. By limiting the domain of reported data, non-physical velocities associated with poor PIV correlations have been removed. Additionally, limiting the domain of the velocity field analysis limited any complexities associated

Table 9.1: Exit velocities for PIV trials calculated from stagnation property measurements

Test geometry	Stagnation pressure (kPa, abs)	Stagnation temperature (°C)	Exit Mach number	Exit velocity (U_j) (m/s)
Nominal set point	129	25.0	0.784	256
$D/a = 3, \theta = 0^\circ$	129	24.2	0.781	255
$D/a = 3, \theta = 10^\circ$	129	24.8	0.782	256
$D/a = 3, \theta = 20^\circ$	129	25.5	0.783	256
$D/a = 3, \theta = 30^\circ$	129	24.9	0.782	256
$D/a = 6, \theta = 0^\circ$	128	24.6	0.775	253
$D/a = 6, \theta = 10^\circ$	129	24.3	0.784	256
$D/a = 6, \theta = 20^\circ$	128	23.9	0.778	254
$D/a = 6, \theta = 30^\circ$	129	24.7	0.783	256
$D/a = 12, \theta = 0^\circ$	129	25.1	0.780	255
$D/a = 12, \theta = 10^\circ$	129	24.8	0.781	255
$D/a = 12, \theta = 20^\circ$	128	23.7	0.779	254
Test average	129	24.6	0.781	255

with compressibility near the jet exit. Considering the average Mach number of 0.781 at the jet exit, u/U values of 0.384, 0.386, 0.390, and 0.398 corresponded to local Mach numbers of 0.3 at offset spacings of 0° , 10° , 20° , and 30° respectively. U varies between test geometries as this velocity is in the global axial direction. A Mach number of 0.3 is a typical threshold below which flows are considered incompressible [67]. Velocities higher than this threshold were only observed and predicted in a small region near the jet local peaks between $x/a = 10$ and $x/a = 12$. Limiting the analysis to the incompressible portion of the jet flow allows for better comparison to the predicted flow model which is based on previous experimentation on incompressible jets.

The instantaneous velocity fields were used to calculate mean velocity and turbulence statistics. Since the flow was sufficiently fast compared to the 84.9 mm PIV field of view and 15 Hz laser repetition rate, individual turbulent structures could not be tracked between successive frame pairs.

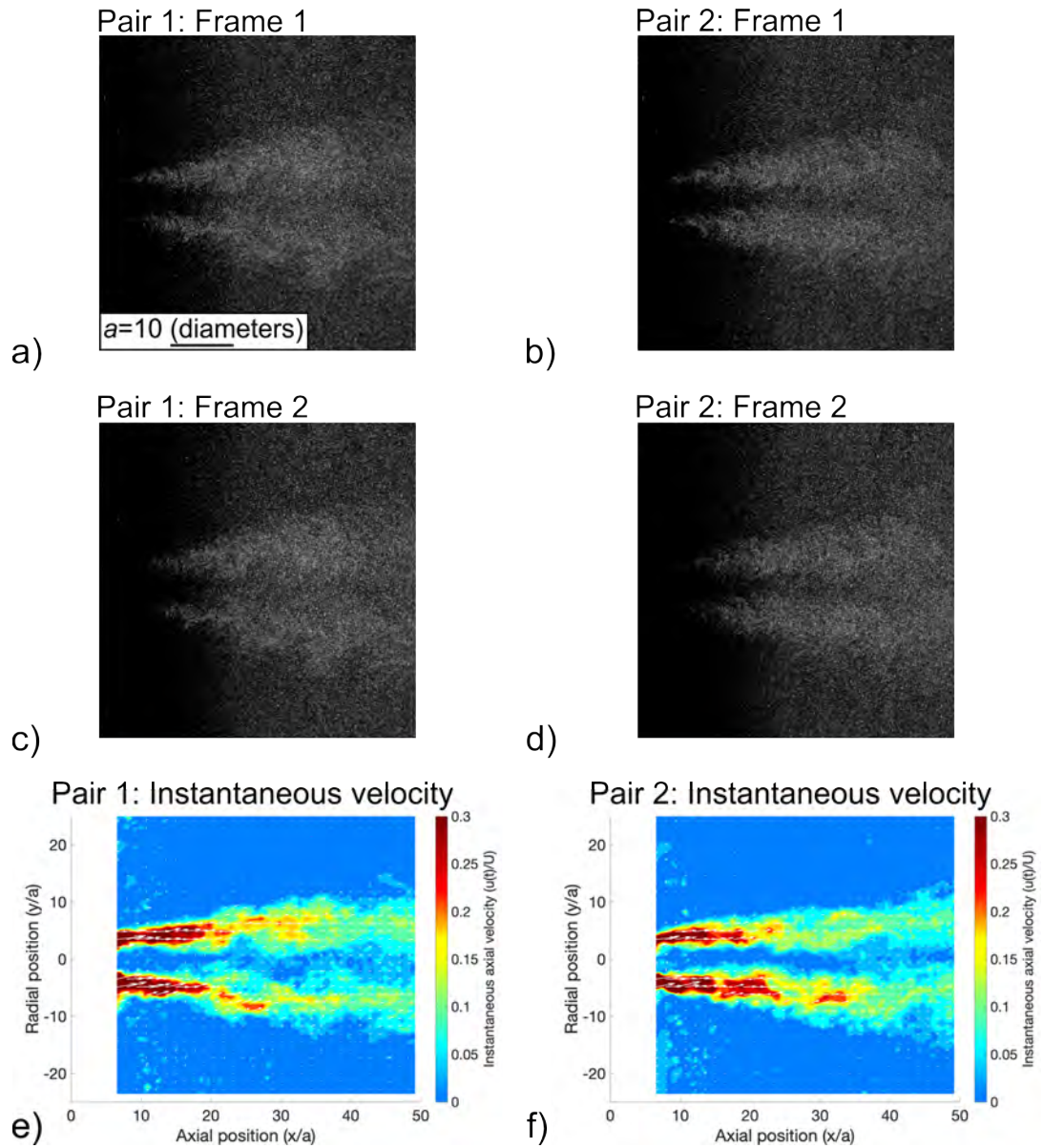


Figure 9.1: (a-d) Still frames recorded during a PIV trial which were processed to create (e, f) instantaneous velocity fields.

9.2 Mean velocity field measurements

Instantaneous velocity field measurements were used to calculate the mean velocity field for each two jet geometry tested. Figures 9.2 through 9.6 show axial velocity distributions throughout the measured flow field as contour plots for the $D/a = 3$, $D/a = 6$, and $D/a = 12$ geometries at various angles (θ), respectively. These contours are compared against the predicted velocity field calculated from the method described in Chapter 8. In all contour plots, the axial component of the mean velocity (u) is normalized by the axial component (U) of the jet exit velocity (U_j).

Jets pairs with the closest spacings and offset angles typically demonstrated more interaction than those with either a wider spacing or offset angle. The analytical model prediction and experimental results flow field characteristics compared well in all trials. In all three spacings, the parallel jets tended to pull together towards combining into a single velocity profile. Within the experimental region of interest, the 3 and 6 diameter cases did combine such that there was only a single resolved velocity peak. Jet combination in these two cases also led to higher retained velocity for further distances in the axial direction. Jets with offset angles of 10° consistently demonstrated the highest mean velocities in the region between the two jets, but less interaction was present for the $D/a = 12$, $\theta = 10^\circ$ trial. Much less interaction was predicted and observed at angles of 20° or 30° .

In addition to the velocities, radial cross sections of the mean axial velocity field were plotted at various axial (x/a) locations as shown in Figures 9.8, 9.9, and 9.10. The predicted flow and experimental results captured the same velocity profile trends in all cases. The differences between predicted and experimental velocity profiles were similar to the precision of the optimized single jet profile in Chapter 8. Initially, all flow fields showed two distinct velocity peaks associated with each individual jet. All velocity profiles decayed and spread at cross sections further downstream. In cases with little or no interaction, the individual jet profiles closely resemble single jets, and jet peaks moved away from the flow field centerline.

When interaction between the two jets was observed, the outer side of each jet velocity profile appeared relatively unaffected. However, the constructive interference of the two jets near the center of the flow caused increasing centerline velocities downstream and less steep velocity gradients in the area near the center of the flow. Though less steep than the outside of the jet, the velocity profile from either jet's local peak to the centerline velocity qualitatively appeared similar to the Gaussian-like profile of a single jet.

Parallel jets which combined into a single profile, or likely would have if measurements extended further downstream, demonstrated interaction in the mean velocity profile similar to angled jets. Combination occurred rapidly after the centerline velocity was similar to the peak velocity such as the $x/a = 25$ or $x/a = 35$ profiles for the 3 and 6 diameter spacing trials, respectively. The velocity profile between the two peaks began to level after these profiles, and the

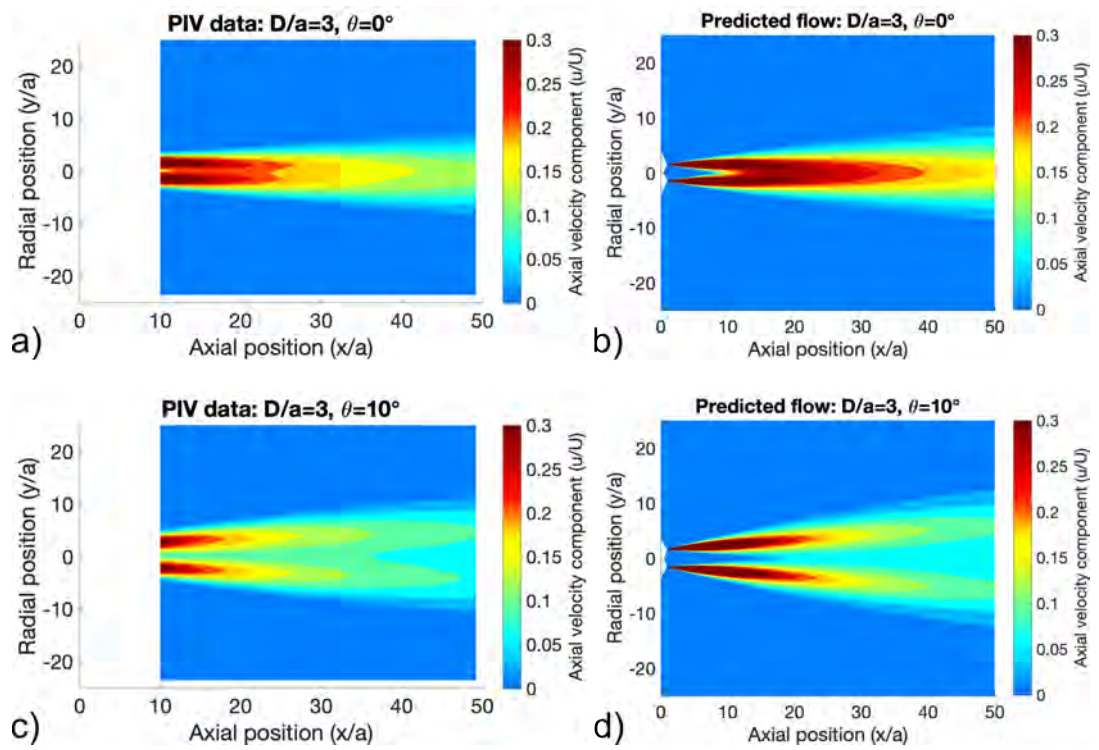


Figure 9.2: Contour plot comparison between (a and c) experimentally recorded and (b and d) predicted mean velocity fields for jets with an orifice spacing or $D/a = 3$ and offset angles of 0° and 10° .

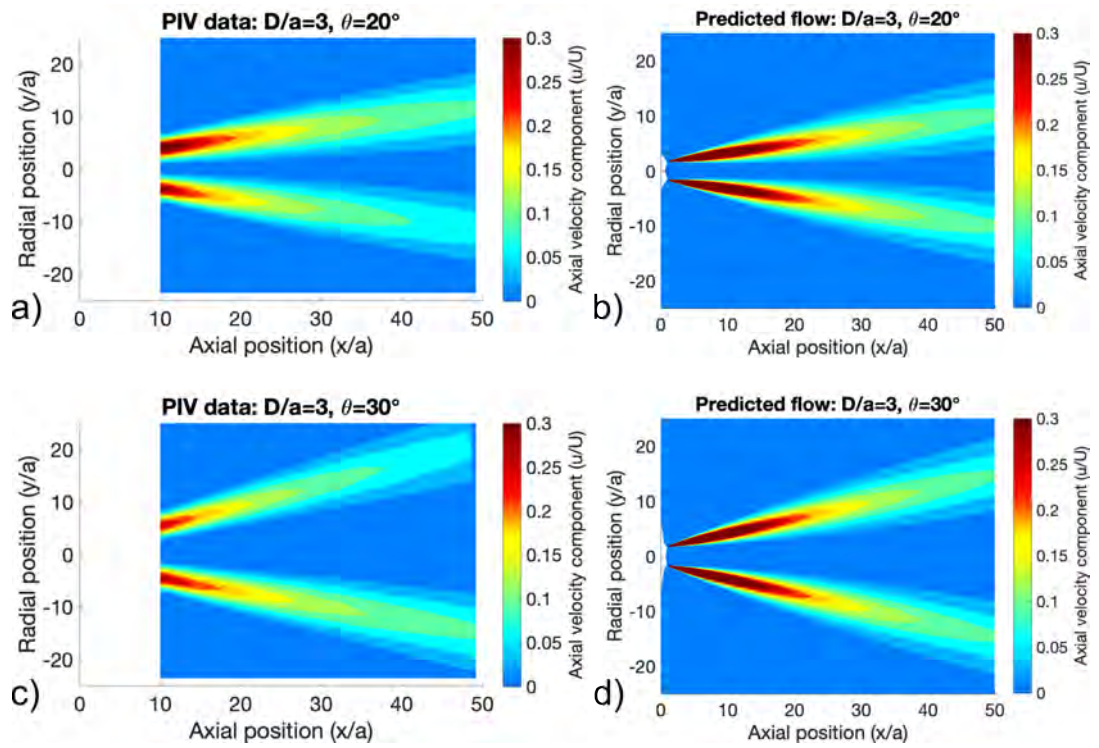


Figure 9.3: Contour plot comparison between (a and c) experimentally recorded and (b and d) predicted mean velocity fields for jets with an orifice spacing or $D/a = 3$ and offset angles of 20° and 30° .

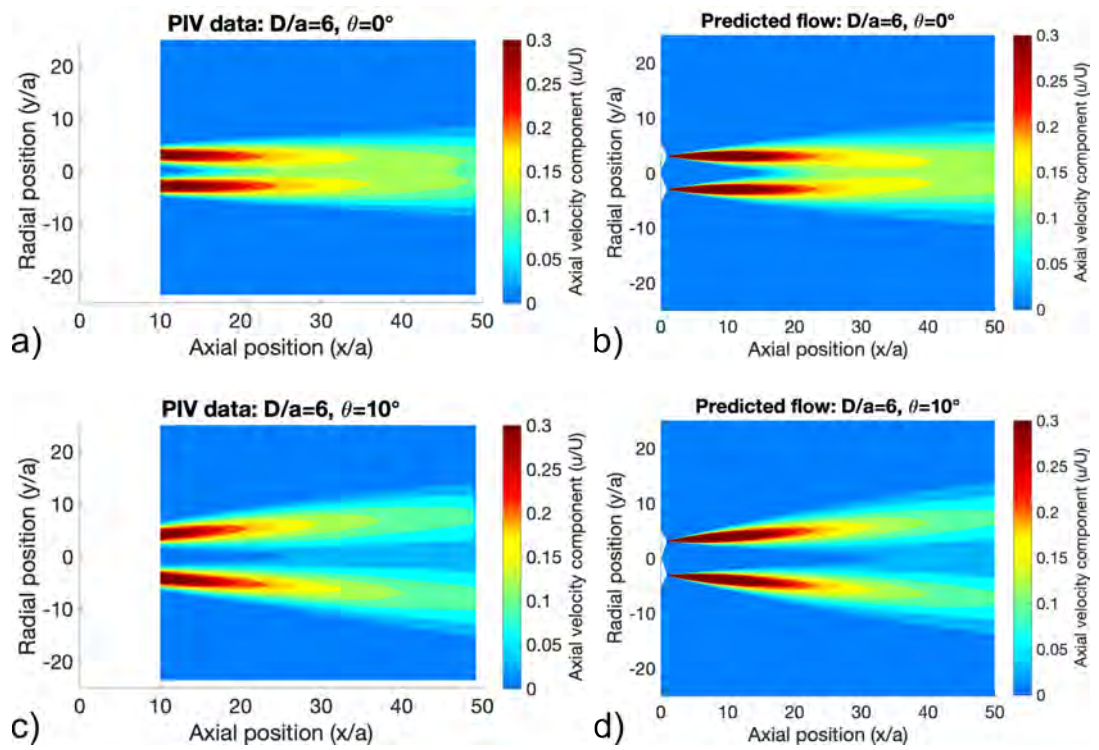


Figure 9.4: Contour plot comparison between (a and c) experimentally recorded and (b and d) predicted mean velocity fields for jets with an orifice spacing or $D/a = 6$ and offset angles of 0° and 10° .

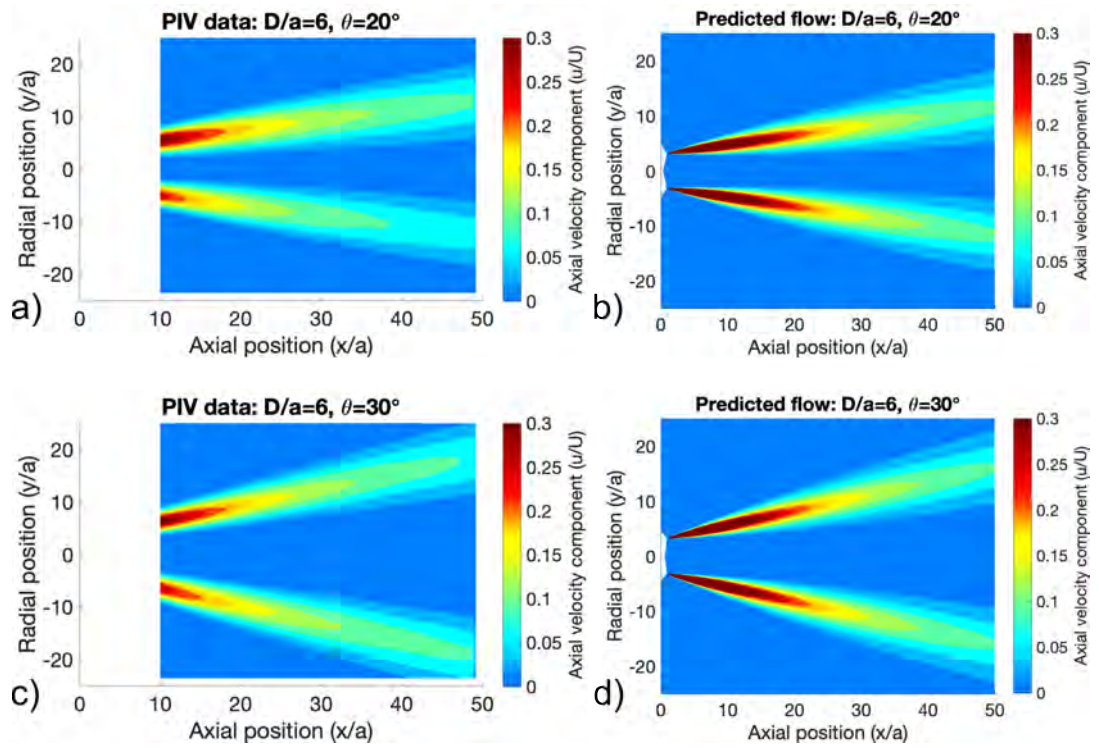


Figure 9.5: Contour plot comparison between (a and c) experimentally recorded and (b and d) predicted mean velocity fields for jets with an orifice spacing or $D/a = 6$ and offset angles of 20° and 30° .

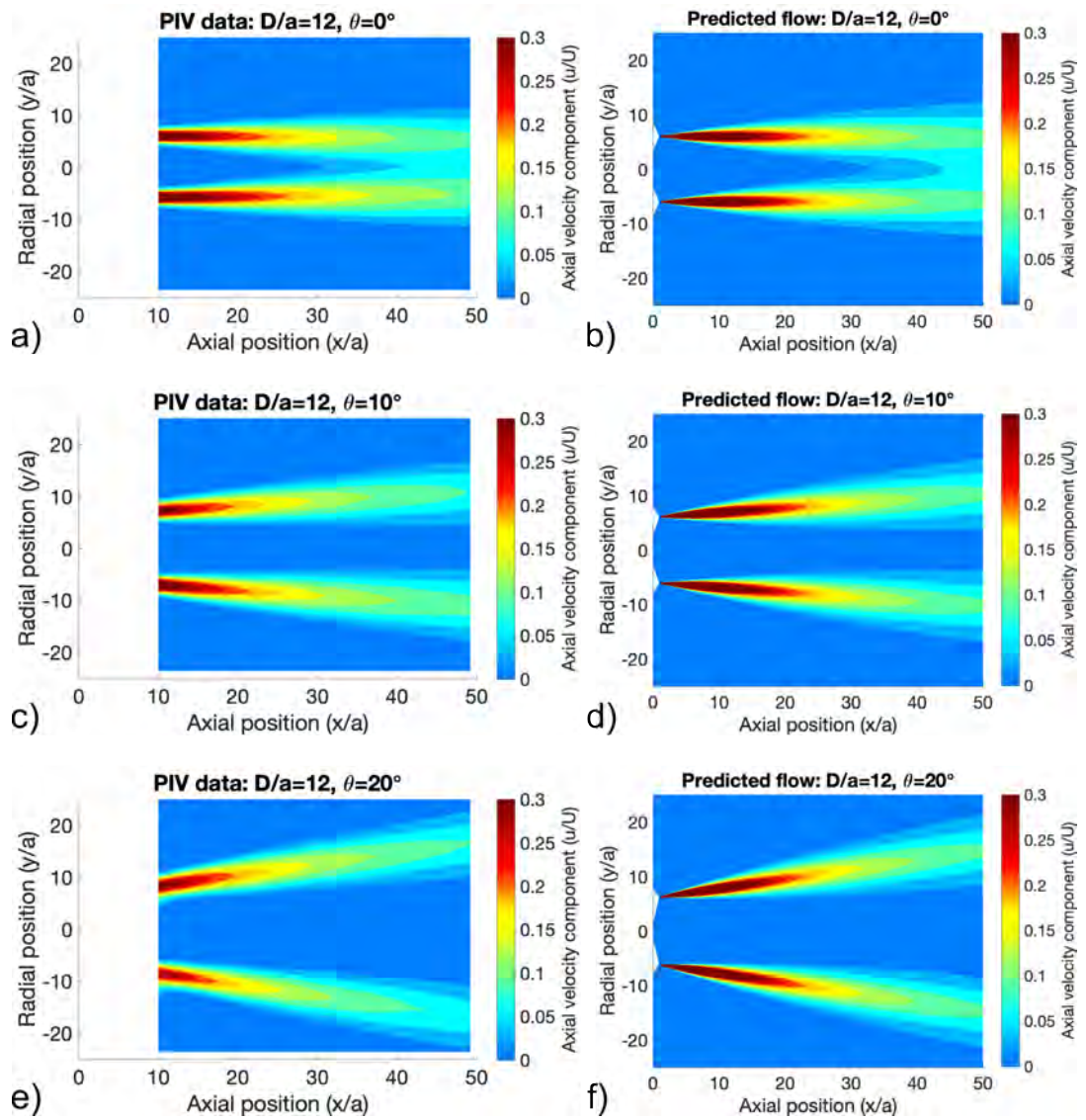


Figure 9.6: Contour plot comparison between (a, c, e, g) experimentally recorded and (b, d, f, h) predicted mean velocity fields for jets with an orifice spacing or $D/a = 12$ and offset angles of 0° , 10° , and 20° .

velocity peaks rapidly pulled to the center of the flow field. After jet combination, only a single velocity peak was able to be resolved.

In some trials, the relative strength of the two jets appeared uneven though the predicted velocity field is symmetric. An example of this is the $D/a = 6$, $\theta = 20^\circ$ trial. This is attributed to a slight imprecision in the alignment of the orifice plate during mounting. The clearance between the mounting screws and their associated holes in the orifice plates allowed for a small rotation of the plate. As such, the laser sheet did not illuminate the exact center of either jet causing the measured velocities to be lower than expected.

Various uncertainty quantification methods have been developed and compared for evaluating PIV datasets, and more sophisticated methods have incorporated evaluation of cross correlation performance [96, 97]. Here, a conservative uncertainty propagation is implemented which relies on calculating mean axial velocity uncertainty (U_u) as:

$$U_u = \frac{\sigma_{u(t)}}{\sqrt{N}} \quad (9.1)$$

where $\sigma_{u(t)}$ is the standard deviation of instantaneous velocity measurements ($u(t)$) and N is the number of frame pairs recorded ($N = 1,000$ for all tests here) [98]. By using the standard deviation of instantaneous velocity measurements, this method accounts for, but does not differentiate between, uncertainty associated with the actual turbulent nature of the measurement and measurement errors in data collection and processing [98]. Since axial velocity is a function of the position within the field of view, velocity uncertainty is variable throughout the measurement domain. This is represented for the $D/a = 6$ and $\theta = 0^\circ$ trial in Figure 9.7. Of note, mean axial velocity uncertainty calculated similarly to and is directly proportional to the turbulence strength discussed in Section 9.3. Spatial trends in mean velocity uncertainty can thus be inferred from Figures 9.13 through 9.15. The maximum mean axial velocity uncertainty recorded from all trials was 2 m/s which occurred near the orifices of the jets for the $D/a = 6$, $\theta = 0^\circ$ trial. This is a conservative estimation for uncertainty in the region of the flow near the jet orifices at axial distances below approximately $x/a = 10$. Mean axial velocity uncertainty further downstream is below approximately 0.7 m/s.

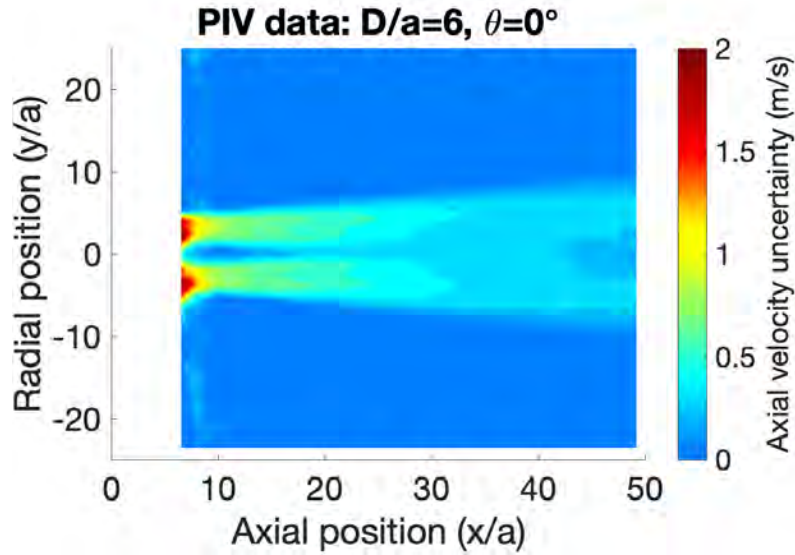


Figure 9.7: Local mean axial velocity uncertainty contour for the $D/a = 6, \theta = 0^\circ$ trial which has the largest uncertainty value observed here.

9.2.1 Centerline velocity changes in the axial direction

The ratio of centerline velocity to the local peak velocity (u_c/u_p) can be a quantification for describing the level of interaction between two jets at some axial location (x/a). Shown in Figure 9.11, the centerline to local peak velocity ratio increases throughout the PIV measurement region of interest. This ratio reached unity for the 3 and 6 diameter parallel jet cases as these jets were observed to combine prior to 50 diameters downstream in the axial direction. Additionally, all 10° jets and the $D/a = 3, \theta = 20^\circ$ trials showed significant interaction as previously defined of the u_c/u_p ratio reaching a value of 0.1. It is likely that the $D/a = 6, \theta = 20^\circ$ trial would have also interacted before the flow dissipated, but the maximum u_c/u_p value observed within the measurement domain was 0.066. The remaining trials showed little increase in centerline velocity, so the jets did not interact.

In all test geometries represented in Figure 9.11, the PIV results showed interaction occurring before the predicted flow field. This was particularly apparent at the smallest spacings and offset angles and in the region of the flow field closest to the jet orifices. This is likely related to the prediction underestimating the width of the jets at given locations, because the prediction and PIV measurements both showed u_c/u_p ratios tenting towards similar values further in the flow field.

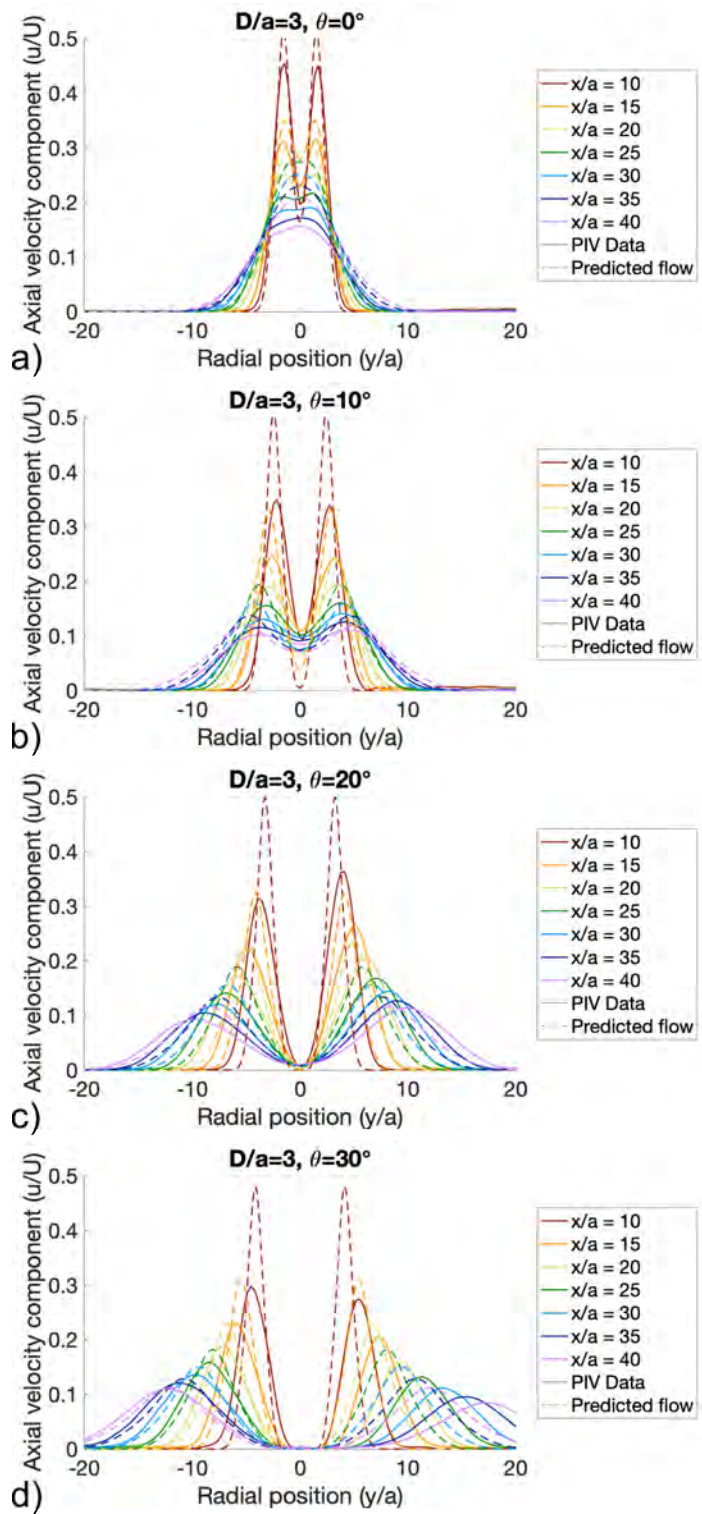


Figure 9.8: Axial velocity profile comparison between PIV measurements and model predictions at various axial locations for jets with orifice spacing of $D/a = 3$.

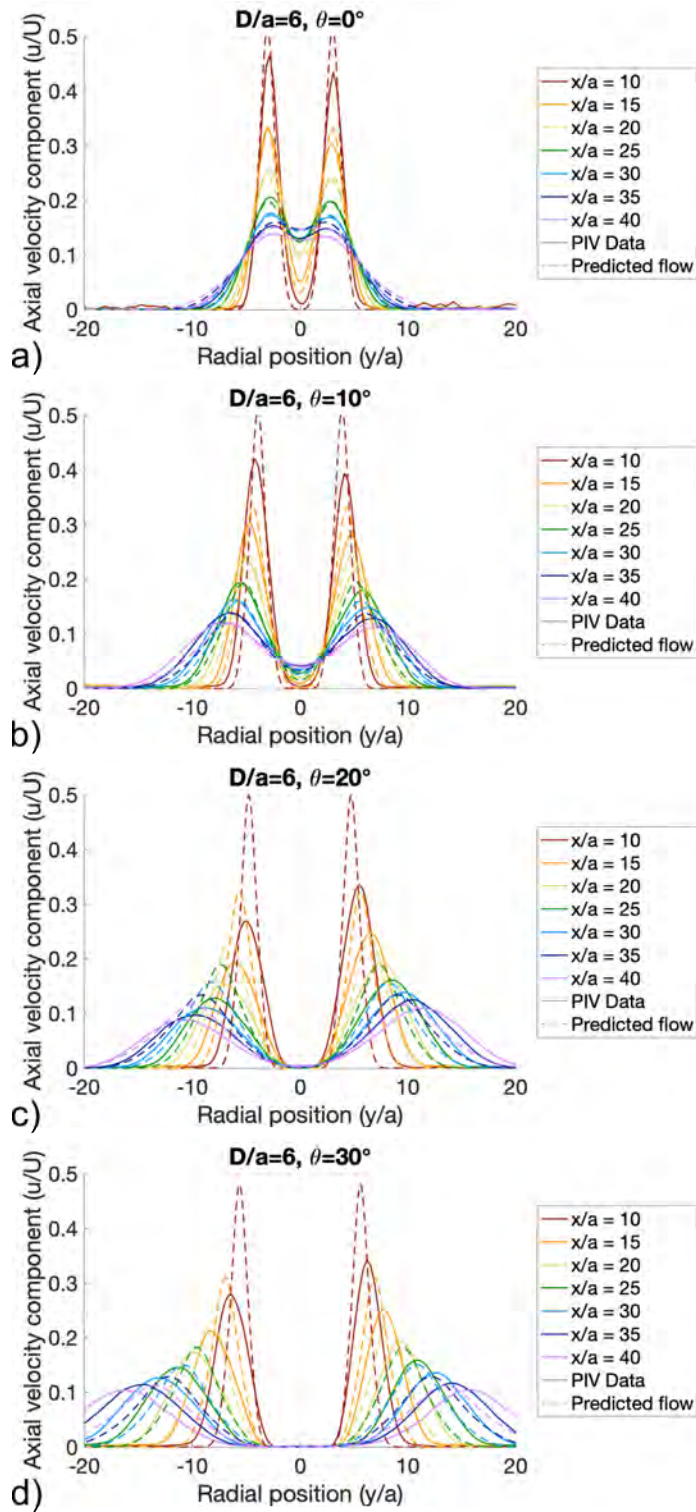


Figure 9.9: Axial velocity profile comparison between PIV measurements and model predictions at various axial locations for jets with orifice spacing of $D/a = 6$.

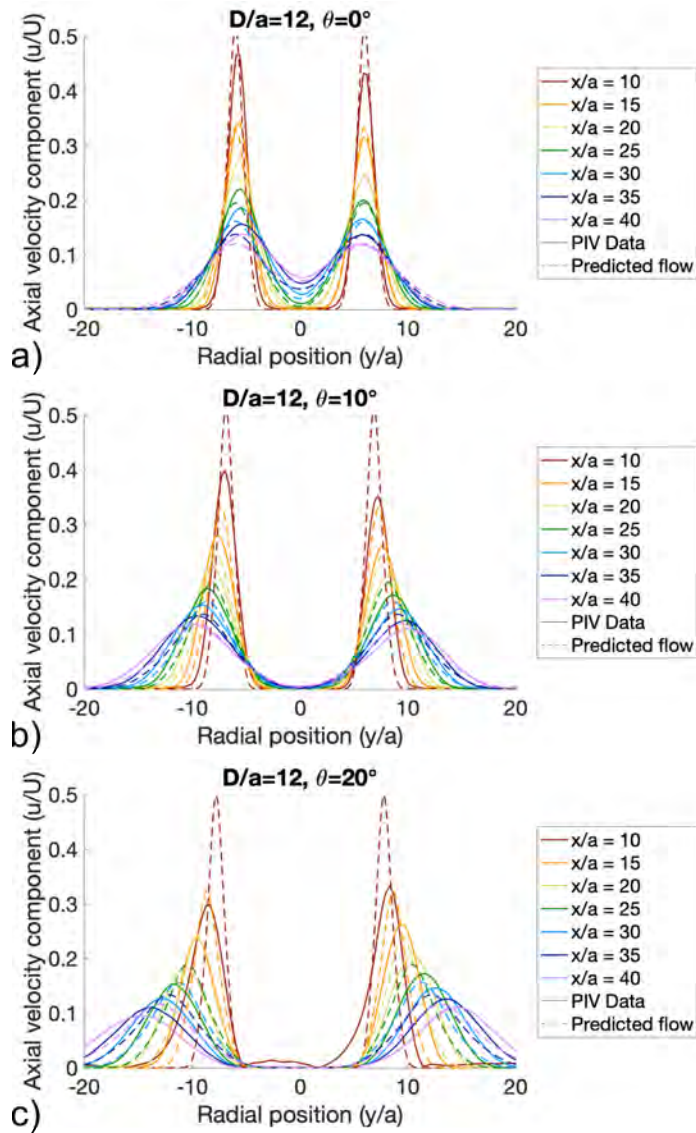


Figure 9.10: Axial velocity profile comparison between PIV measurements and model predictions at various axial locations for jets with orifice spacing of $D/a = 12$.

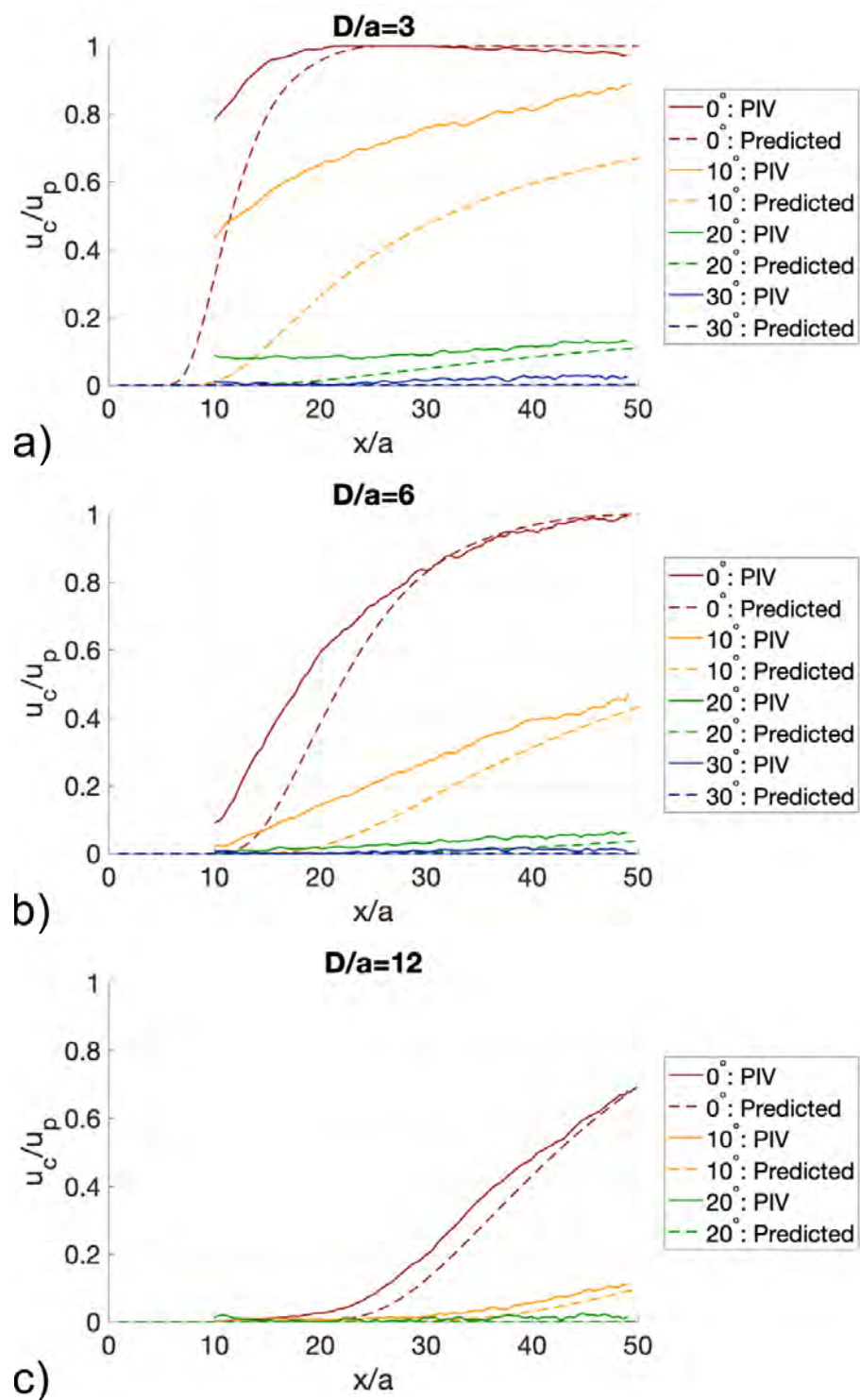


Figure 9.11: Measured and predicted centerline to local peak velocity ratio progression for spacings of (a) $D/a = 3$, (b) $D/a = 6$, and (c) $D/a = 12$.

9.2.2 Tracking local peak velocity in the mean flow field

During the discussion of the predicted two jet flow field, an inward shift in local peak velocity associated with the superposition of the two jets' contributions to the combined field was discussed. The observed location of the local peak velocities associated with the top and bottom jets was tracked throughout the PIV region of interest and compared to the predicted flow field in Figure 9.12. Top and bottom jet nomenclature refers to the location of the jet in the positive or negative y/a half of the PIV region of interest respectively as visualized in Figures 9.2(a and c), 9.3(a and c), 9.4(a and c), 9.5(a and c), and 9.6(a, c, and e). Generally, prediction captured the progression of the local peak velocity locations well including the distinct, inward curving path for the parallel jets. The accuracy of the prediction was greater for narrower jets. The inaccuracies at the 30° offset angle trials were likely associated with orifice plate machining imprecision particularly regarding the internal and external surface qualities of the orifice plates.

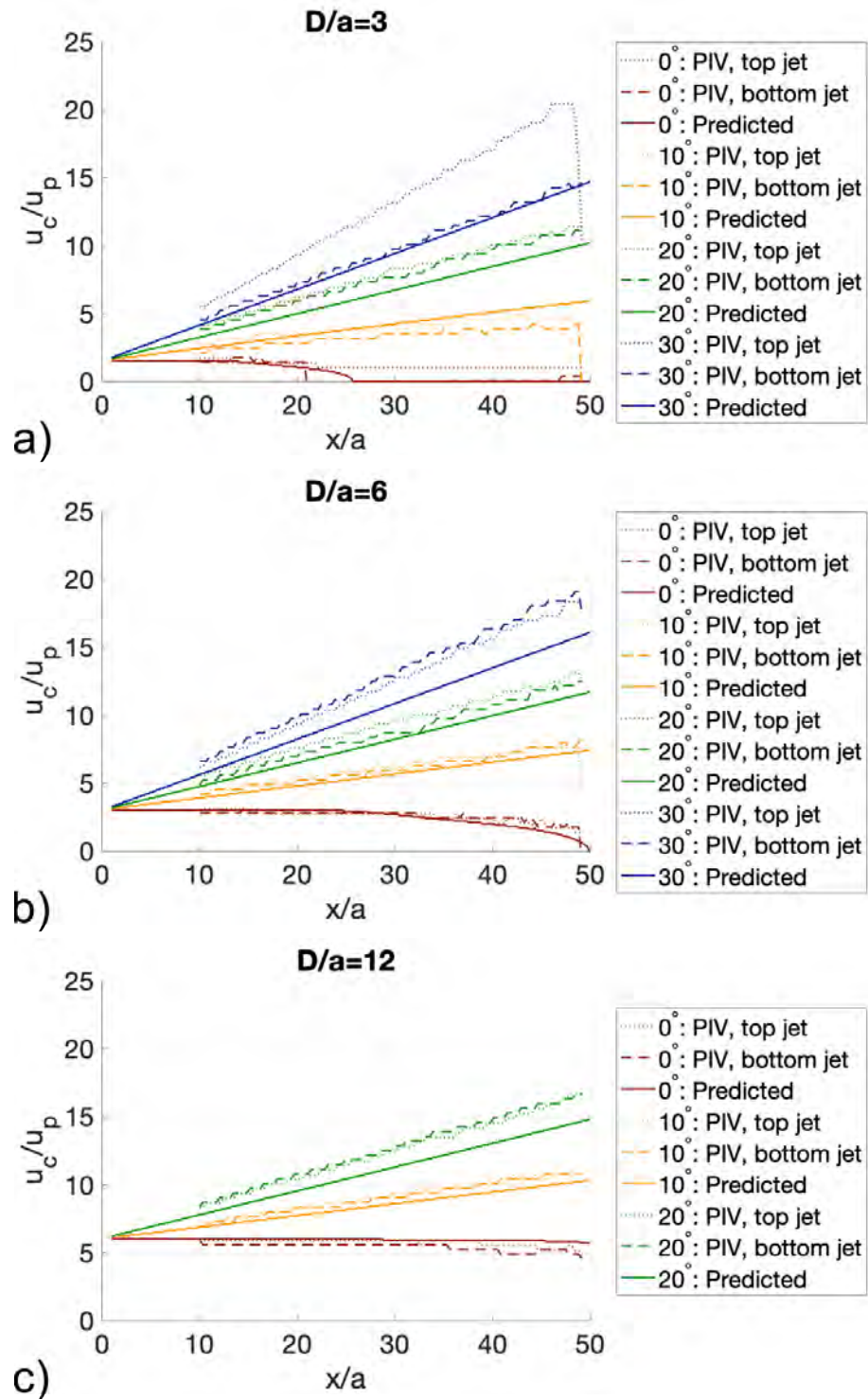


Figure 9.12: Measured and predicted local peak velocity location progression for spacings of (a) $D/a = 3$, (b) $D/a = 6$, and (c) $D/a = 12$.

9.3 Turbulence strength observations

Turbulence strength fields were calculated for each of the trials in this test series as another method to characterize the jet interactions. The turbulence strength is calculated as the root-mean-square of the turbulent velocity and is used to describe much turbulence varies the velocity at a given location from the mean flow. Turbulent velocity ($u'(t)$) is calculated as the difference between the instantaneous velocity ($u(t)$) at some point and the corresponding mean velocity (u) at that location as:

$$u'(t) = u(t) - u \quad (9.2)$$

Turbulent strength (u'_{rms}) was calculated for each point in the flow field as:

$$u'_{rms} = \sqrt{\frac{1}{N} \sum_{n=1}^N [u'(t_n)]^2} \quad (9.3)$$

where N represents the number of PIV frame pairs in the dataset. Like mean velocity previously reported, turbulent strength calculations are reported here focus on the axial component of the flow and were normalized by the axial component of the jet exit velocity (U).

Figures 9.13, 9.14, and 9.15 show the contour maps and radial cross sections of the turbulent strength fields for each of the trials at 3, 6, and 12 diameter spacings respectively. Jet pairs with smaller spacings and offset angles had increased levels of turbulence in the region between the two jets than the outer periphery of the flow. The jet pairs with the highest levels of interaction based on the mean velocity field also had the most notable increase in turbulence in the central region of the flow.

In all scenarios, the turbulence cross sections initially captured two main peaks associated with the each jet in the pair. Smaller local peaks were associated with the maximum shear stress in each jet, and the local mean peak velocity coincided with the valley in the middle of these two locations. These profiles decayed, spread, and appeared to constructively interfere similarly to the mean velocity profiles in Section 9.2. The turbulence strength profiles began to combine into a single profile where the initial effects of either jet were no longer able to be resolved similar to the mean velocity field measurements. However, unlike the mean velocity field which combined and resembled a single jet, the combined turbulence fields resemble a broad plateau of fairly consistent turbulence strength. Additionally, turbulence combination was seen before jet combination and even in scenarios such as $D/a = 3$, $\theta = 10^\circ$ where jet combination was not predicted before the jets were dissipated (per Figure 8.8). In scenarios where the turbulence strength profiles did not fully combine, the turbulence profiles became largely broad plateaus with only small peaks associated with the initial jet profiles and a small valley along the flow centerline. Generally, the turbulence strength profiles

follow demonstrated greatest interaction at closely spaced and narrowly offset or parallel jet configurations, and the distinction in the turbulence profile between the two jets became minimal relatively early in the flow field.

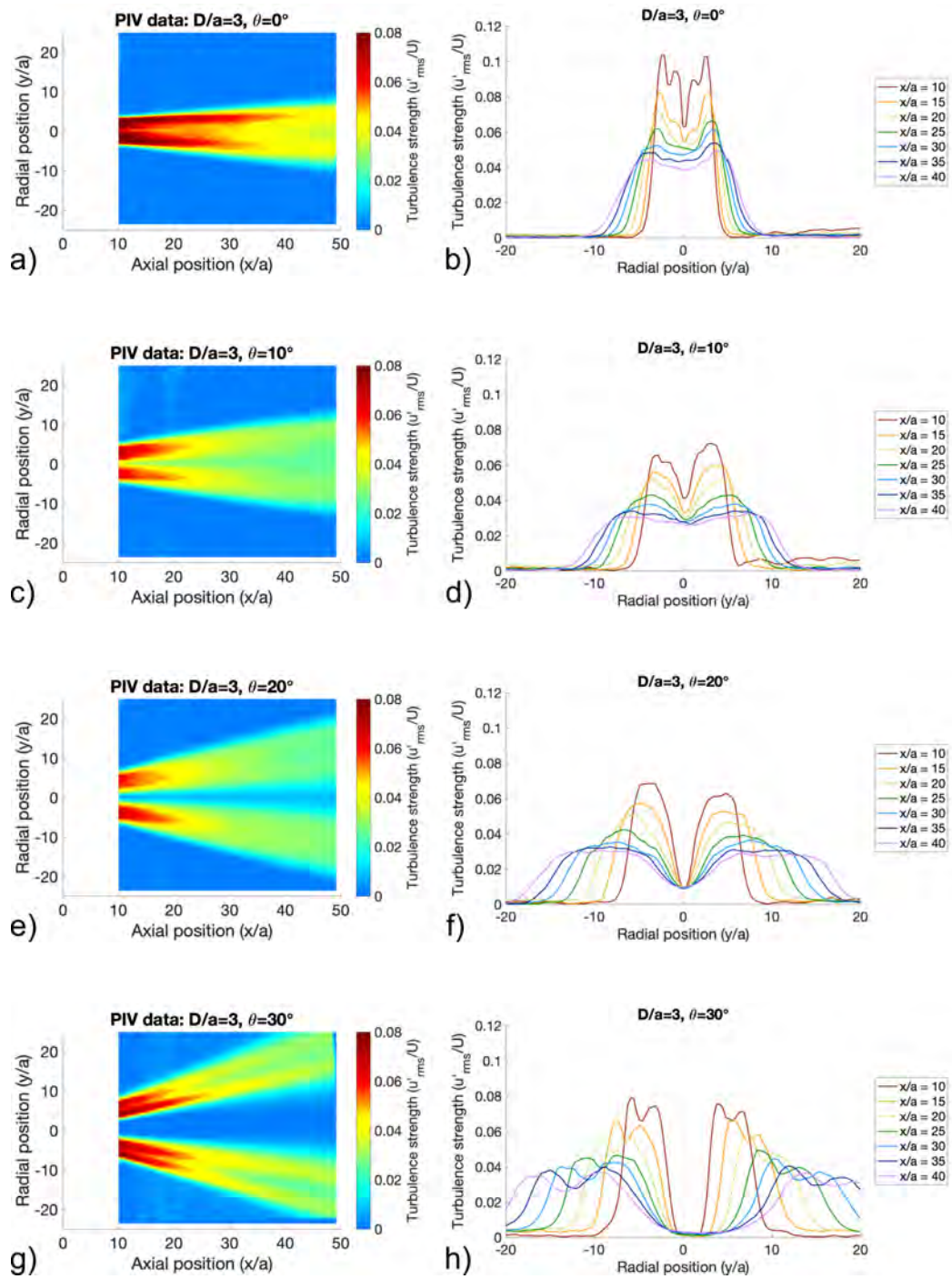


Figure 9.13: (a, c, e, g) Turbulence strength contours and (b, d, f, h) profiles for PIV trials with orifice spacing of $D/a = 3$.

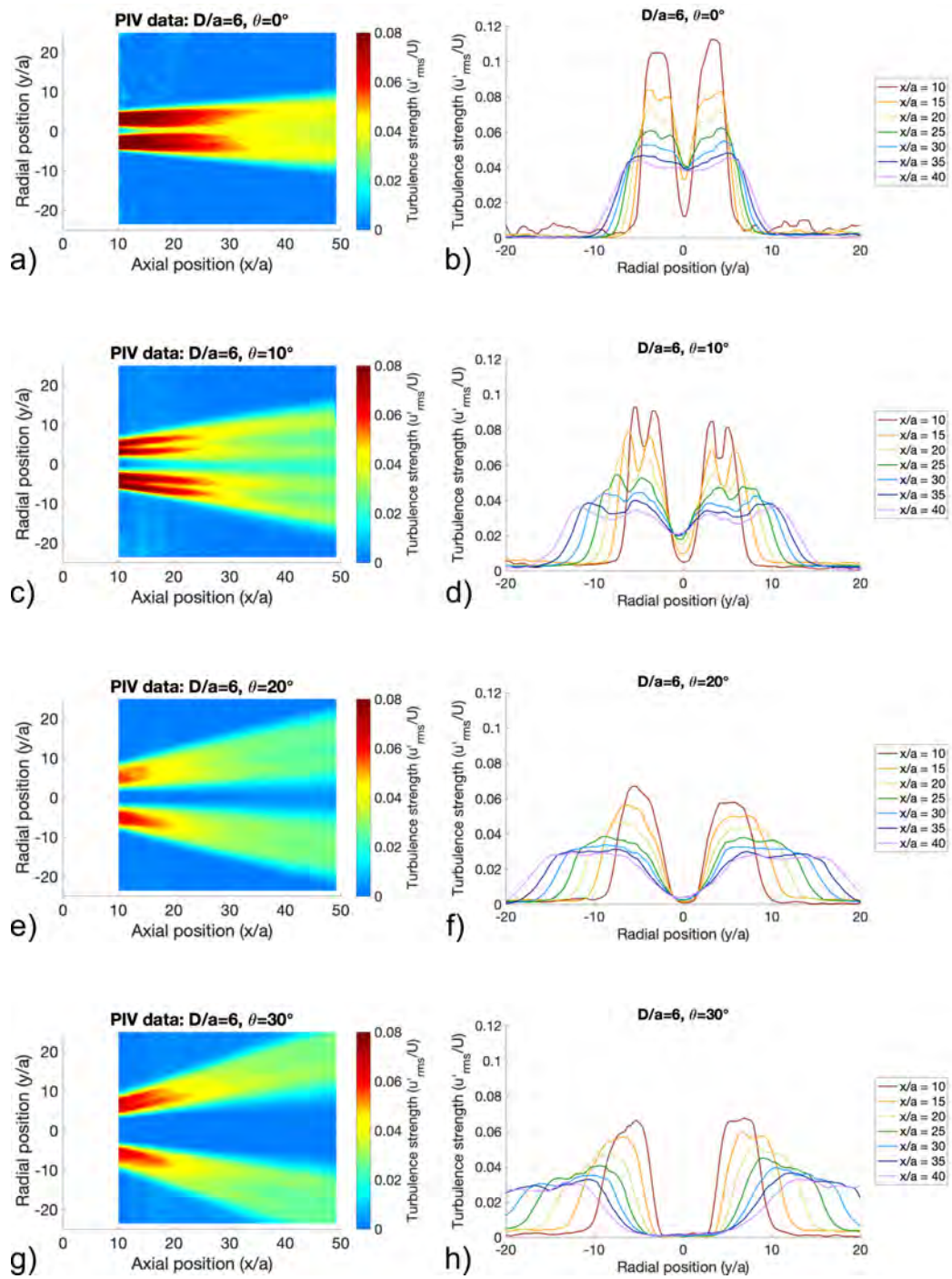


Figure 9.14: (a, c, e, g) Turbulence strength contours and (b, d, f, h) profiles for PIV trials with orifice spacing of $D/a = 6$.

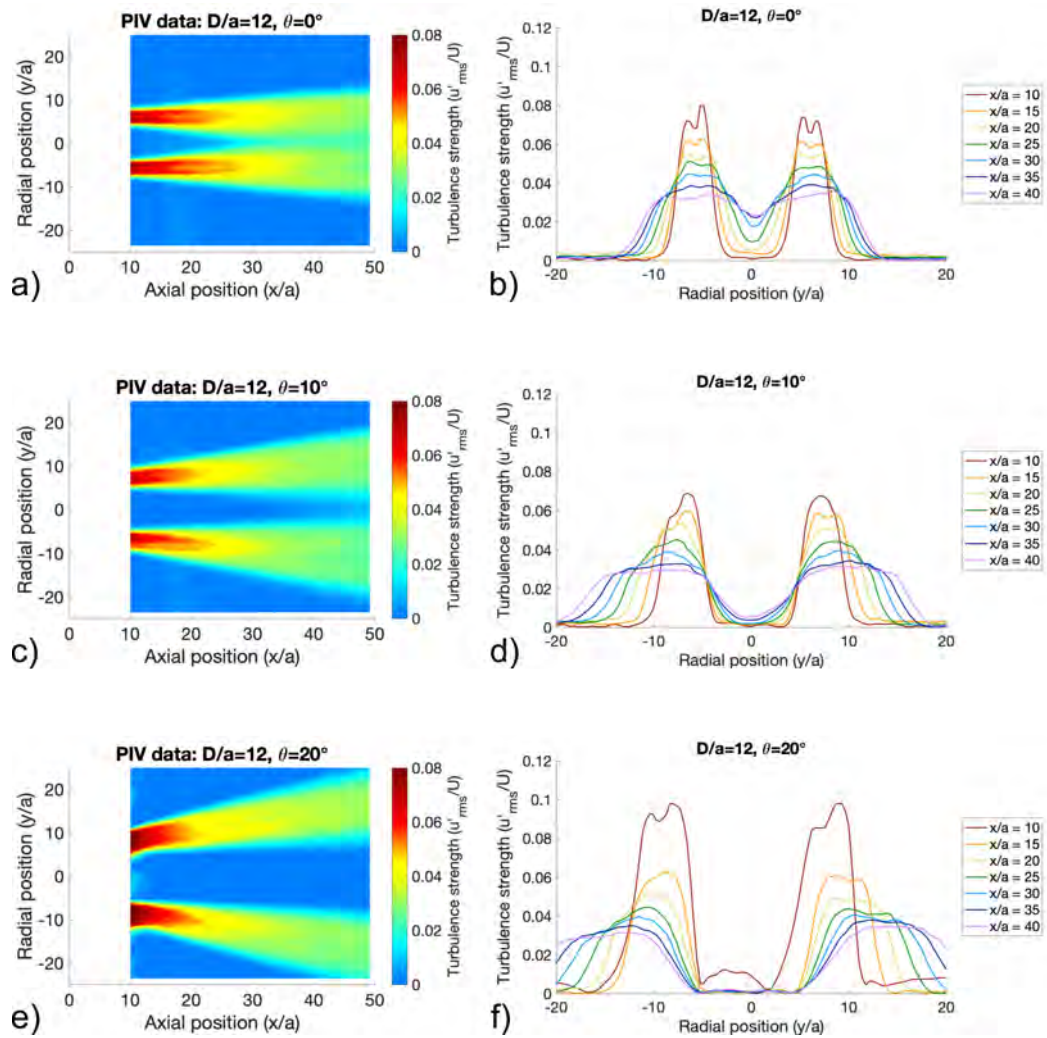


Figure 9.15: (a, c, e) Turbulence strength contours and (b, d, f) profiles for PIV trials with orifice spacing of $D/a = 12$.

9.4 Estimated mass flow entrainment from experimentally observed flow fields

9.4.1 Estimating three-dimensional flow field from two-dimensional PIV data

To describe how mass flow was entrained as jet flows evolved in the global axial (x) direction, mass flow rate \dot{m} is defined as:

$$\dot{m} = \rho \int u dA \quad (9.4)$$

where the jets were evaluated as incompressible such that trends in mass flow rate were solely attributed to changes in the velocity field. Additionally, the axial velocity component u was used, and the surface through which the integral was evaluated (dA) was perpendicular to this velocity component. A limitation to the ability to directly quantify mass flow rate from the experiments performed here is the two-dimensional nature of the PIV data recorded while information about the full three-dimensional velocity fields was required to evaluate the integral in Equation 9.4. Accordingly, assumptions were made to expand PIV measurements into approximated three-dimensional velocity fields to complete the mass flow rate calculation.

A typical and logical assumption for jet flows would be assuming radial symmetry and reforming Equation 9.4 in cylindrical coordinates. Shown in Figure 9.16, performing this calculation on the baseline single jet experiment captured the linear mass flow entrainment trend as the mean velocity profile model described in Section 8.1. Entrainment rate here refers to the rate of change of the quantified mass flow rate in Equation 9.4 with respect to changes in axial position. The mass flow rate calculation based on the mean velocity profile model is predicted to be inaccurate at values of $x/a < 10$ due to compressibility effects and the downstream location of the virtual origin. Offset in the slopes of these lines was attributed to different jet velocity profile shapes as reported in Figure 8.3. Reported mass flow rates have been normalized by the flow rate at the orifice plate as calculated from isentropic flow relations and stagnation property measurements. The predicted flow field had a wider jet profile than the PIV data which caused an increase in the mass flow rate integral. Jet prediction model constants optimization was biased to capture local velocity peaks rather than the lower velocity tails of the jet profile which comprised the majority of the mass flow rate. Assuming radial symmetry captured the entrainment characteristics of a single jet. However, a radial symmetry approximation does not work for the two jet configurations as these flows were not rotationally symmetric.

From observations reported in literature on rows of parallel jets at various spacings, the velocity profile in the out-of-plane direction (not measured here) is self similar to the single jet profile [99]. It is assumed that this observation would extend to outwardly angled jets as the flow field similarities between parallel and angled jets have been demonstrated here. Here, the third axis to complete the full

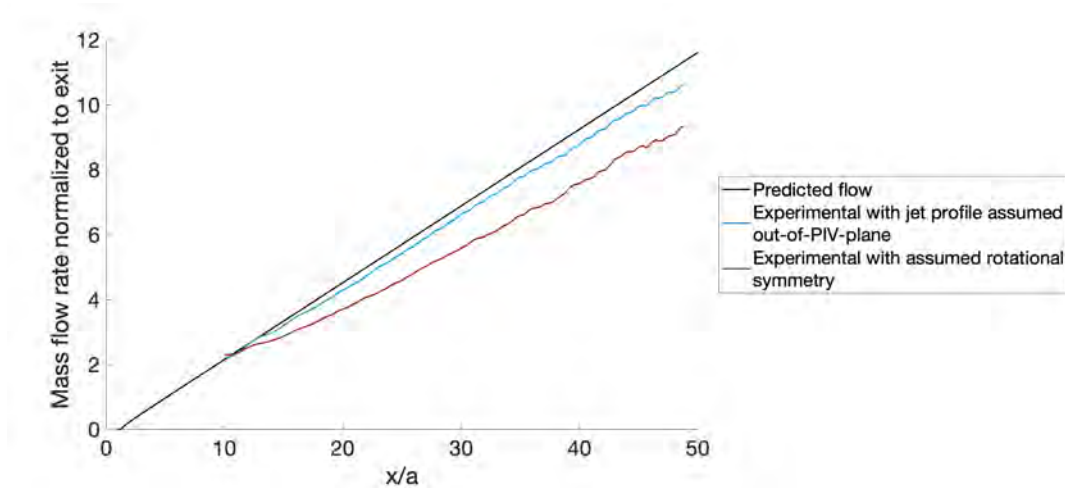


Figure 9.16: Comparing predicted mass flow rate from the single jet velocity field model to approximations based on the measured PIV velocity field.

flow field is referred to as “out-of-PIV-plane” and its coordinate location is given the variable z . The local peak to the jet profile in the out-of-PIV-plane direction occurs at $z = 0$ in the xy -plane which contains both orifices and the trajectory of each jet. Since the PIV data recorded here was taken in this xy -plane, the measured velocity fields reported in Figures 9.2 through 9.6 were used as the basis to estimate the entire three-dimensional flow field. Shown in Figure 9.17(a) and (b), the full three-dimensional velocity field of a flow was reconstructed by using rows of data from the PIV measured xy -plane to approximate the remainder of the yz -plane velocity field at various axial (x/a) positions. Within an approximated yz -plane velocity field, the only directly measured data was at $z = 0$. Moving away from the data at $z = 0$, the approximated local velocities follow a jet profile (represented in Figure 9.17(c)) which is defined for each radial position (y/a) in the plane. Advantages of this flow field approximation method include the ability account for the interacting region between jets and no need for prior knowledge about the flow field such as an axis of symmetry or any jet configuration geometry. Additionally, mass flow rate can be easily calculated by numerically integrating the approximated yz -plane velocity fields at any axial location.

This flow field reconstruction technique was also compared to the mass flow rate entrainment estimation calculated from the mean velocity profile model in Figure 9.16. Similar to the model prediction and the previous rotational symmetry calculation, mass flow rate increased linearly with axial position. The slope discrepancy between assuming the z -direction profile and the model was smaller than when rotational symmetry was evaluated because the jet profile in the assumed z -direction technique matched the shape of the model more closely. Since the three-dimensional flow field constructed by assuming a jet velocity profile in the z -direction captures similar mass flow rate trends to model prediction and

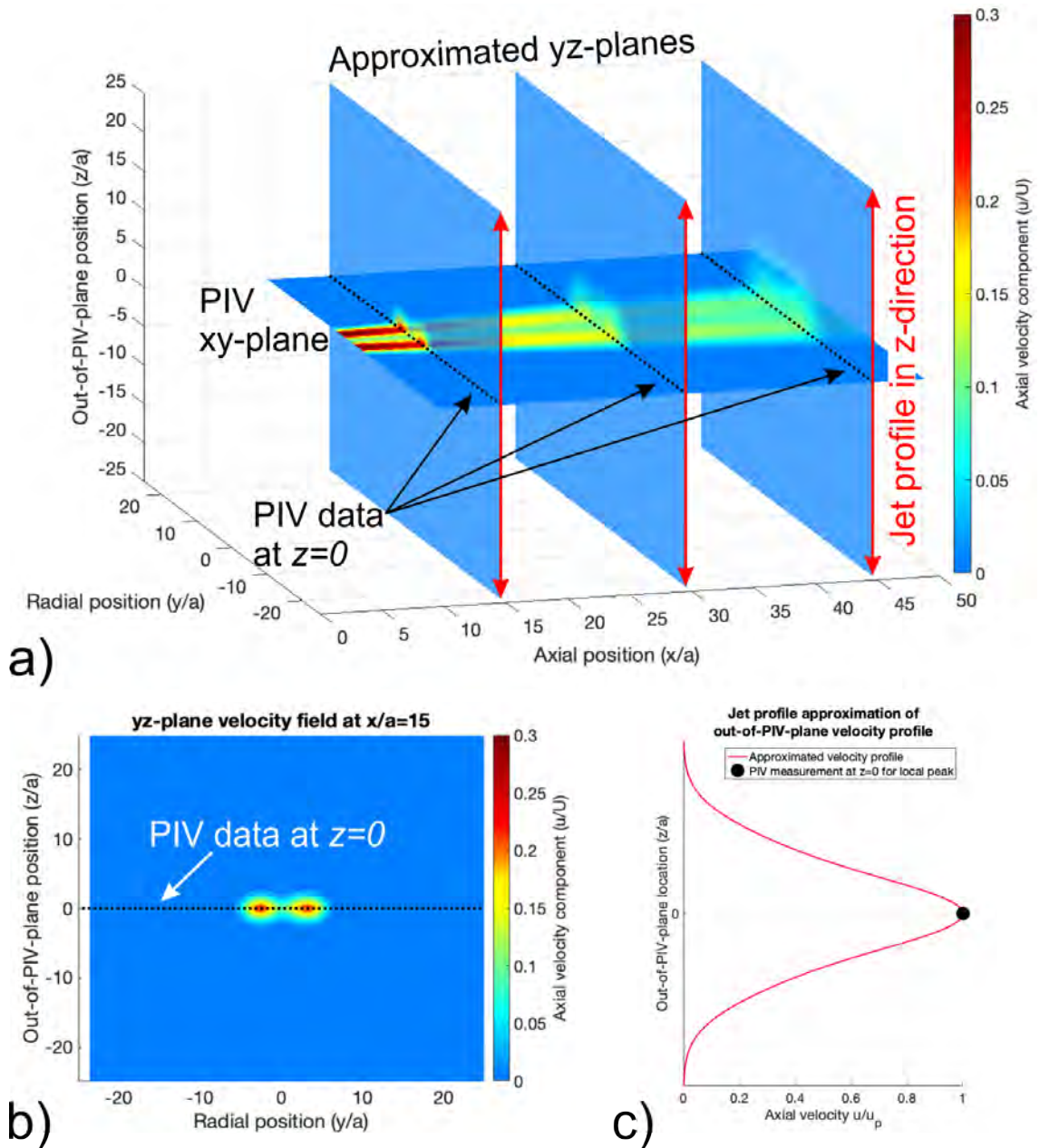


Figure 9.17: (a) Schematic representation demonstrating how two dimensional PIV data is used to reconstruct and approximate the full three dimensional flow field. (b) Velocity is approximated in the yz -plane at each axial (x/a) location using using PIV data at $z = 0$ in the plane and a (c) jet profile to approximate the velocity field variation in the z -direction

the typical rotational symmetry argument for a single jet, this method was used to evaluate mass flow rate for the two jet configurations.

9.4.2 Mass flow entrainment observations for pairs of outwardly angled jet pairs

Using the three-dimensional flow field reconstruction method which assumes a jet profile in the out-of-PIV-plane z -direction, mass flow rate was calculated versus axial position for the parallel and angled jet pairs at normalized orifice spacings of $D/a = 3$ and $D/a = 6$. The $D/a = 12$ trials were excluded from this analysis because their spacing resulted in clipping of the flow field at the edge of the PIV field of view. Further, due to the superposition method for modeling of the two jet configurations, mass flow rate entrainment was predicted to be equal for all test geometries. For this reason, this analysis focuses on the results obtained through the approximated three-dimensional flow fields generated from experimental data.

Shown in Figure 9.18, all jet configurations demonstrated an increasing mass flow rate as a function of axial position as the jet pairs spread and interacted with each other. Here, mass flow rate is reported as a ratio of the mass flow rate estimated at a specific x/a location to the mass flow rate at the orifice plate which was calculated from stagnation properties. The outwardly oriented jet pairs of all angles demonstrated similar, consistent entrainment rates throughout the region of interest.

The $D/a = 6, \theta = 10^\circ$ example has a higher than typical mass flow rate associated with relatively higher and more symmetric jet velocity profiles than the $\theta = 20^\circ$ and $\theta = 30^\circ$ examples which can be observed in Figure 9.9. This example still demonstrated a similar mass entrainment rate to the other angled jet configurations which was noted by the slope of the mass flow rate trend. To demonstrate the similarity in entrainment rates between trials without the offset seen in the $D/a = 6, \theta = 10^\circ$ example in Figure 9.18, the mass flow rate trends were re-normalized by the observed flow rate at $x/a = 10$ at the beginning of the PIV quantification region as shown in Figure 9.18. In these plots, the angled jets mass flow rate trends more closely coalesced along a consistent entrainment rate.

While angled jets appeared to demonstrate similar mass flow rate changes as a function of axial position, the parallel jets scenarios showed an entrainment rate which decreased at further locations. Particularly noticeable in the $D/a = 6$ parallel jet example, the mass flow rate trend compared similarly to the angled jets at first, but significant divergence was noted after approximately $x/a = 25$. This divergence occurred while interaction between the two jets was significant as demonstrated with a u_c/u_p ratio of nearly 0.75. Similar interaction was observed earlier in the parallel $D/a = 3$ trial which was likely the cause of the mass flow rate divergence from the angled jet cases sooner in the axial direction. These observations were also made by E. B. Gordon and I. Greber for experiments on rows of parallel jets where mass flow rate increased similarly for all jet

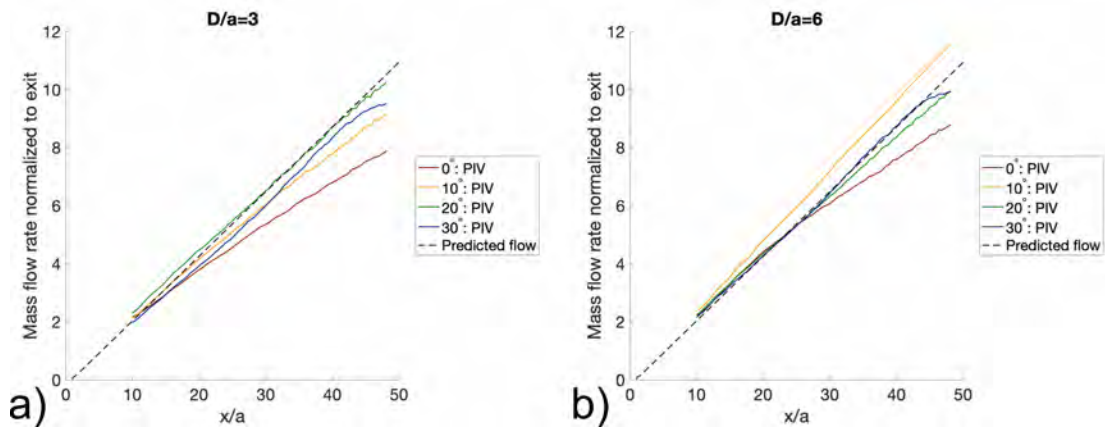


Figure 9.18: Mass flow rate versus axial position approximated from PIV measured velocity fields for the (a) $D/a = 3$ and (b) $D/a = 6$ test geometries. Mass flow rate is normalized by the flow rate at the jet orifices as determined from stagnation pressure and temperature.

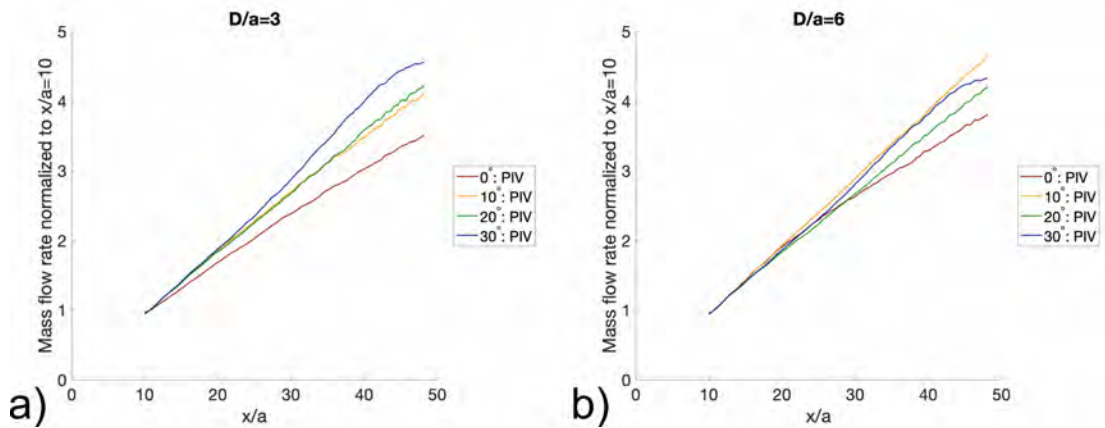


Figure 9.19: Mass flow rate versus axial position approximated from PIV measured velocity fields for the (a) $D/a = 3$ and (b) $D/a = 6$ test geometries. Mass flow rate is normalized by the flow rate at the $x/a = 10$ flow cross section to minimize vertical deviations between tests.

spacings for some distance downstream until entrainment rate slowed [99]. The location where entrainment rate began to slow increased with increasing initial orifice spacing. Here, an outward offset angle had a similar effect to increased orifice spacing because both of these geometric changes minimized the interaction between jets thus allowing each individual jet more space to freely spread and, importantly, interact with and ultimately entrain fluid from the quiescent environment. Since it was observed that increased offset angle has a more prominent effect on minimizing the intensity of jet interactions than increased orifice spacing, variations in entrainment rate were only observed in the trials without any outward jet orientation.

CHAPTER 10

CONCLUSIONS

The battery venting process under abuse conditions was investigated by developing a new technique for pre-burst pressure measurement and characterizations of the subsequent venting flow. The implementation of case strain was unique among battery abuse experiments. The optical flow measurements provided a more thorough characterization of the fluid dynamics of battery venting than previously attained. A greater scientific knowledge of lithium ion battery safety was developed as the physical mechanism contributing to their greatest hazards has been uniquely characterized.

The body of work presented here provides unique and useful quantifications and deeper understanding of the dynamics of pressure driven venting flows comprised of multiple jets into a quiescent environment. While an application of interest during these experiments was lithium ion battery venting failures, the methods and analysis performed here were conducted such that the findings are not limited to this specific application.

10.1 General remarks on non-invasive pressure monitoring and the subsequent venting dynamics

A methodology for strain based internal pressure measurement on both thin and thick walled cylinders was developed. A test apparatus was constructed allowing the non-invasive measurement of pressure build up during heating of a test specimen. Validation experiments were performed which demonstrated the capabilities and repeatability of the developed experimental method. Repeated trials measured the predictable pressure response of carbon dioxide in a sealed cylinder during constant volume heating.

High speed schlieren imaging measured transient single-phase and multi-phase venting into the environment immediately after burst and its evolution with time. Two different concentrations of sucrose solutions were tested and exhibited different droplet breakup regimes. The lower viscosity solution was atomized while the higher viscosity solution exhibited a second wind-induced breakup regime. Droplet spray angle was initially much wider than gas jet spreading and tended to zero as the liquid was expelled, but gas projection and spreading was consistent throughout the simulated burst event. The low viscosity, at-

omized flow was wider than the high viscosity, wind-blown spray. The outer edges of multiphase transient venting flow was initially populated with particles but was eventually bounded by gas. Since initial droplet spray angle was, wider than the offset angle between the jets in the vent cap tested, nearby multiphase venting flow characterization should consider spray interactions between jets in the entire combined flow field.

Tip penetration and time-of-arrival measurements demonstrated that the inclusion of liquid decreases the rate of flow front penetration into the environment. The flow front of small atomized particles from the low viscosity sucrose solution were much closer to matching the gas-only trial than the high viscosity, wind-induced flow. While the high viscosity droplets were slower, they decelerate less quickly than the gas or atomized droplets which may lead to greater total penetration into the surroundings.

The combined flow field from two nearby, outwardly angled jets was investigated in order to increase the basic, scientific understanding of jet interactions common in venting scenarios. To predict how jet interactions would occur, a simple model based on superposition of a single jet velocity profile was developed to make a priori predictions of the combined mean velocity field created by the two nearby jets. Model constants were optimized for the specific orifice shape and testing conditions by optimizing velocity decay and virtual origin location for a single jet baseline experiment. This model was used to develop useful metrics and predict the range of spacings and offset angles where jet combination or significant interaction was expected to occur. By predicting the combined flow for a broad range of angled jet geometries, it was observed that the strength of jet interactions is more easily diminished by increasing offset angle rather than orifice spacing. In contrast, jets with significantly large spacing or offset angle larger than approximately 23° may be considered independent.

PIV experiments were performed at jet orifice spacings of 3, 6, and 12 diameters with offset angles of 0° , 10° , 20° , and 30° . Velocity profiles from PIV measurements compared similarly to model predictions. The intensity of jet interaction was quantified by both following the evolution of the centerline velocity between the jets as a percentage of the local peak velocity along with tracking the inward shift of the local peak velocity caused by the superposition of the jet flows. Mean axial velocity measurements demonstrated increased interaction between the jets at smaller offset angles and closer orifice spacings. Combination of the jets was observed for parallel jet examples at 3 and 6 diameter orifice spacings. As predicted by the model, interaction between the two jets appeared more sensitive to changes in offset angle than initial spacing. Similar to the mean velocity profiles, turbulence was amplified in the region between the two jets, and increased turbulence was noticed closer to the orifices in the flow field than increases in mean velocity. An approximation of mass flow entrainment was developed from the recorded PIV velocity fields which demonstrated that mass flow rate increased with further axial distance from jet orifices. The two jet geometries which combined in the PIV field of view demonstrated relatively decreased entrainment at downstream axial positions.

10.2 Findings specific to lithium ion battery safety

Using the non-invasive pressure measurement methodology, a series of experiments on live 18650 format batteries was performed at heating rates of 2.4°C/min, 3.6°C/min, and 4.8°C/min. The highest rate test was performed in duplicate. All tests captured a final pressure rise before venting onset beginning between battery surface temperatures of 138°C and 151°C. The observed final pressure rise in all trials had magnitudes comparable to the known burst pressure of the vent caps installed on the brand of battery tested. The rate of pressure build up within each battery increased before venting onset. By examining surface temperature measurements made throughout these abuse experiments, it was observed that the internal pressure build up before venting corresponds to the onset of battery self-heating which indicates thermal runaway. Erroneous indicated internal pressure measurements before the final pressure build up were attributed to interactions between internal battery components and the case including the possibility of localized component failures within the cell.

The novel ability to monitor the final pressure rise indicative of an imminent venting failure provides a useful, noninvasive diagnostic technique for battery abuse testing. However, battery self heating was also observed as an indicator of imminent venting failure. Temperature measurement was more simple to implement than strain regarding the complexity of the experimental hardware, data acquisition needs, and data processing. Strain measurement corrections relied on knowing the battery case temperature throughout each trial, so strain can only be realistically implemented in conjunction with temperature measurements. Strain based internal pressure measurement was effective for observing thermal runaway and gas generation prior to venting onset, but this method should not be considered a replacement for temperature measurement as a means of state-of-health monitoring.

Venting experiments performed here demonstrated that gas jet pairs show increased interaction at low orifice spacings and offset angles. Given the approximate orifice spacing of $D/a = 6$ for an 18650 format battery and an observed offset angle of 42°, the significantly wide offset angle would prevent any significant jet interactions from occurring even at this moderate diameter spacing. Gas venting from a typical 18650 format battery may be considered as four independent jets. However, the initial droplet spray cone angle of 97° and the significant concentration of atomized particles during the low viscosity sucrose solution burst test indicates that spray patterns within the entire droplet field must be considered as a whole to characterize multiphase battery venting.

10.3 Future work

One main limitation to the strain based internal pressure build up measurement methodology developed here is the potential for interactions between

the tightly wound electrochemical components and the outer case of a cylindrical battery causing erroneous strain measurements. Refocusing investigation on more deformable battery construction styles, such as pouch cells, may be an alternative path to studying gas generation throughout the thermal runaway process. Pouch style batteries typically swell during failure. Methods could be developed to correlate the deformation of an unconstrained cell to internal pressure. Alternatively, these cells could be constrained during failure, and the load exerted by on a hypothetical test fixture would correspond to the gas generation within the battery. By advancing the understanding of pressure build up in cells of different construction but identical chemistries, inferences could be made on the internal state of cylindrical cells during thermal runaway.

Future investigation into the interaction of nearby gas jets can advance understanding of venting flows in multiple useful ways. An important investigation would be evaluating the accuracy and limitations of the velocity superposition modeling method in other configurations such as inwardly angled jets or flows caused by more than two equal strength jets. Superposition of other flow properties which have been characterized for single jets, such as turbulence strength, may yield useful predictions as well. Another consideration for evaluating the hazards of venting flows, including from failing batteries, is the surrounding into which venting occurs. Here the environment adjacent the venting flow was both quiescent and unobstructed, but many real-world scenarios may include unrelated flows (e.g. heating, ventilation, and air conditioning) and additional structures or enclosures. Investigating the effect of atmospheric pressure on multiple jet flow interaction may also be of interest for aviation or space flight applications. The presence of unique complexities would alter characteristics of venting flows.

Additional research should be performed to quantify flammability of transient, multiphase venting. Both gas mixing and droplet spray will have important contributions to the overall combustibility of flammable vented material. These experiments should be complimented by further testing on live batteries to quantify parameters such as droplet size and velocity to understand propagation into the environment.

BIBLIOGRAPHY

- [1] H. J. Hussein, S. P. Capp, and W. K. George. Velocity measurements in a high-reynolds-number, momentum-conserving, axisymmetric, turbulent jet. *Journal of Fluid Mechanics*, 258:31–75, 1994.
- [2] B. Scrosati and J. Garche. Lithium batteries: Status, prospects and future. *Journal of Power Sources*, 195:2419–2430, 2010.
- [3] J. Boyes and I. Gyuk. Electrical energy storage for utility scale applications. In *Electric Power*, 2007.
- [4] K. Lynn et al. US battery storage market trends. Technical report, Energy Information Administration, 2018.
- [5] C. Kang. Galaxy Note 7 owners are urged to stop using their phones. *New York Times*, 9 September 2016.
- [6] U. Irfan. How lithium ion batteries grounded the Dreamliner: Official report on Boeing 787 fires tells a cautionary tale about advanced batteries. *Scientific American*, 18 December 2014.
- [7] S Abada et al. Safety focused modeling of lithium-ion batteries: A review. *Journal of Power Sources*, 306:178–192, 2016.
- [8] L. A. McKenna. Electronic cigarette fires and explosions in the United States 2009 - 2016. Technical report, FEMA, 2017.
- [9] F. A. Mier. Measurement of 18650 format lithium ion battery vent mechanism flow parameters. Masters Thesis, 2018.
- [10] V. Muenzel et al. A comparative testing study of commercial 18650-format lithium-ion battery cells. *Journal of The Electrochemical Society*, 162(8):A1592–A1600, May 2015.
- [11] Phillip Weicker. *A Systems Approach to Lithium-Ion Battery Management*. Artech House, 2014.
- [12] Q. Wang et al. Thermal runaway caused fire and explosion of lithium ion battery. *Journal of Power Sources*, 208:210:224, 2012.
- [13] E. P. Roth et al. Advanced technology development program for lithium-ion batteries: Thermal abuse performance of 18650 li-ion cells. Technical Report SAND2004-0584, Sandia National Laboratories, 2004.

- [14] S. S. Zhang. Insight into the gassing problem of Li-ion battery. *Frontiers in Energy Research*, 2:1–4, 2014.
- [15] C. Mikolajczak et al. *Lithium-Ion Batteries Hazard and Use Assessment*. Springer, 2011.
- [16] MTI Corp. 18650 cylinder cell case with anti-explosive cap and insulation o-ring - 100 pcs/package - eq-lib-18650, 2013.
- [17] Engineering and safety center technical bulletin. Technical Report No. 09-02, NASA, 2009.
- [18] P. G. Balakrishnan, R. Ramesh, and T. Prem Kumar. Safety mechanisms in lithium-ion batteries. *Journal of Power Sources*, 155:401–414, 2006.
- [19] T. Unkelhaeuser and D. Smallwood. United States Advanced Battery Consortium electrochemical storage system abuse test procedure manual. Technical Report SAND99-0497, Sandia National Laboratories, 1999.
- [20] W. C. Chen et al. Effects of thermal hazard on 18650 lithium-ion battery under different states of charge. *J Therm Anal Calorim*, 121:525–531, 2015.
- [21] R. E. Lyon and R. N. Walters. Energetics of lithium ion battery failure. *Journal of Hazardous Materials*, 318:164–172, 2016.
- [22] Y Fu et al. An experimental study on burning behaviors of 18650 lithium ion batteries using a cone calorimeter. *Journal of Power Sources*, 273:216–222, 2015.
- [23] D. P. Finegan et al. In-operando high-speed tomography of lithium-ion batteries during thermal runaway. *Nature Communications*, 2015.
- [24] J. Lamb and C. J. Orendorff. Evaluation of mechanical abuse techniques in lithium ion batteries. *Journal of Power Sources*, 247:189–196, 2014.
- [25] H. Wang et al. Mechanical abuse simulation and thermal runaway risks of large-format Li-ion batteries. *Journal of Power Sources*, 342:913–920, 2017.
- [26] H. Huang et al. Lithium metal phosphates, power and automotive applications. *Journal of Power Sources*, 189:748–751, 2009.
- [27] X. Liu et al. Heat release during thermally-induced failure of a lithium ion battery: Impact of cathode composition. *Fire Safety Journal*, 85:10–22, 2016.
- [28] A. W. Golubkov et al. Thermal-runaway experiments on consumer Li-ion batteries with metal-oxide and olivin-type cathodes. *RSC Advances*, 4:3633–3642, 2014.
- [29] Q. Wang et al. Combustion behavior of lithium iron phosphate battery induced by external heat radiation. *Journal of Loss Prevention in the Process Industries*, 49:961–969, 2017.

- [30] F. Larsson et al. Characteristics of lithium-ion batteries during fire tests. *Journal of Power Sources*, 271:414–420, 2014.
- [31] B. L. Ellis et al. A multifunctional 3.5 V iron-based phosphate cathode for rechargeable batteries. *Nature Materials*, 6:749–753, 2007.
- [32] P. Ping et al. Study of the fire behavior of high-energy lithium-ion batteries with full-scale burning test. *Journal of Power Sources*, 285:80–89, 2015.
- [33] N. S. Spinner et al. Physical and chemical analysis of lithium-ion battery cell-to-cell failure events inside custom fire chamber. *Journal of Power Sources*, 279:713–721, 2015.
- [34] P. T. Coman et al. Numerical analysis of heat propagation in a battery pack using a novel technology for triggering thermal runaway. *Applied Energy*, 203:189–200, 2017.
- [35] J. Lamb et al. Failure propagation in multi-cell lithium ion batteries. *Journal of Power Sources*, 283:517–523, 2015.
- [36] S. Hong et al. Design of flow configuration for parallel air-cooled battery thermal management system with secondary vent. *International Journal of Heat and Mass Transfer*, 116:1204–1212, 2018.
- [37] J. Xu et al. Prevent thermal runaway of lithium-ion batteries with minichannel cooling. *Applied Thermal Engineering*, 110:883–890, 2017.
- [38] S. Wilke et al. Preventing thermal runaway propagation in lithium ion battery packs using a phase change composite material: An experimental study. *Journal of Power Sources*, 340:51–59, 2017.
- [39] A. Jossen, V. Spath, H. Doring, and J. Garche. Reliable battery operation — a challenge for the battery management system. *Journal of Power Sources*, 84:283–286, 1999.
- [40] Y. Xing, E. W. M. Ma, K. L. Tsui, and M. Pecht. Battery management systems in electric and hybrid vehicles. *Energies*, 4:1840–1857, 2011.
- [41] M. Keyser et al. Enabling fast charging - battery thermal considerations. *Journal of Power Sources*, 367:228–236, 2017.
- [42] X. Lin et al. Online parameterization of lumped thermal dynamics in cylindrical lithium ion batteries for core temperature estimation and health monitoring. *IEEE Transactions on Control Systems Technology*, 21(5):1745–1755, 2013.
- [43] F. A. Mier and D. Rosewater. Modeling lithium-ion battery internal temperature under load with convective cooling. In *DOE Office of Electricity Annual Peer Review*, 2018.

- [44] S. J. Drake, D. A. Wetz, J. K. Ostanek, S. P. Miller, J. M. Heinzl, and A. Jain. Measurement of anisotropic thermophysical properties of cylindrical Li-ion cells. *Journal of Power Sources*, 252:298–304, 2014.
- [45] F. A. Mier et al. Overcharge and thermal destructive testing of lithium metal oxide and lithium metal phosphate batteries incorporating optical diagnostics. *Journal of Energy Storage*, 13:378–386, 2017.
- [46] I. Buchmann. *Batteries in a Portable World a Handbook on Rechargeable Batteries for Non-Engineers*. Cadex Electronics Inc, 2001.
- [47] P. T. Coman, S. Rayman, and R. E. White. A lumped model of venting during thermal runaway in a cylindrical lithium cobalt oxide lithium-ion cell. *Journal of Power Sources*, 307:56–62, 2016.
- [48] C. G. Ball, H. Fellouah, and A. Pollard. The flow field in turbulent round free jets. *Progress in Aerospace Sciences*, 50:1–26, 2012.
- [49] G. Horn and M. W. Thring. Angle of spread of free jets. *Nature*, (4526):205–206, 1956.
- [50] Walter Tollmien. Calculation of turbulent expansion processes. Technical Report 1085, NACA, 1945.
- [51] A. Cenedese et al. LDA and PIV velocity measurements in free jets. *Experimental Thermal and Fluid Science*, 9(2):125–134, 1994.
- [52] Stephen B. Pope. *Turbulent Flows*. Cambridge University Press, 2000.
- [53] T. Tanaka and E. Tanaka. Experimental study of a radial turbulent jet (1st report, effect of nozzle shape on a free jet). *Bulletin of the JSME*, 19(133):792–799, 1976.
- [54] J. Mi et al. Piv measurements of a turbulent jet issuing from round sharp-edged plate. *Experiments in Fluids*, 42(4):625–637, 2007.
- [55] T. Tanaka and E. Tanaka. Experimental study of a radial turbulent jet (2nd report, wall jet on a flat smooth plate). *Bulletin of the JSME*, 20(140):209–215, 1977.
- [56] S. Ghahremanian. *A Near-Field Study of Multiple Interacting Jets: Confluent Jets*. PhD thesis, Linkoping University, 2014.
- [57] D. Duke, D. Honnery, and J. Soria. Experimental investigation of nonlinear instabilities in annular liquid sheets. *Journal of Fluid Mechanics*, 691:594–604, 2012.
- [58] R. D. Reitz and F. V. Bracco. *Encyclopedia of Fluid Mechanics*, chapter 10: Mechanisms of Breakup of Round Liquid Jets. Gulf Publishing Company, 1986.

- [59] S. P. Lin and R. D. Reitz. Drop and spray formation from a liquid jet. *Annual Review of Fluid Mechanics*, 30:85–105, 1998.
- [60] W. E. Ranz. Some experiments on orifice sprays. *Canadian Journal of Chemical Engineering*, 36:175, 1958.
- [61] R. D. Reitz and F. V. Bracco. Mechanism of atomization of a liquid jet. *The Physics of Fluids*, 25:1730, 1982.
- [62] N. Leboucher, F. Roger, and J. L. Carreau. Atomization characteristics of an annular liquid sheet with inner and outer gas flows. *Atomization and Sprays*, 24(12):1065–1088, 2014.
- [63] T. C. W. Lau and G. J. Nathan. Influence of stokes number on the velocity and concentration distributions in particle-laden jets. *Journal of Fluid Mechanics*, 757:432–457, 2014.
- [64] C. S. Lee, S. W. Park, and S. I. Kwon. An experimental study on the atomization and combustion characteristics of biodiesel-blended fuels. *Energy and Fuels*, 19:2201–2208, 2005.
- [65] L. Guan, C. Tang, K. Yang, J. Mo, and Z. Huang. Effect of di-n-butyl ether blending with soybean-biodiesel on spray and atomization characteristics in a common-rail fuel injection system. *Fuel*, 140:116–125, 2015.
- [66] M. Raffel, C. E. Willert, S. T. Werely, and J. Kompenhans. *Particle Image Velocimetry: A Practical Guide*. Springer, 2nd edition, 2007.
- [67] Y. A. Cengel and J. M. Cimbala. *Fluid Mechanics Fundamentals and Applications*. McGraw Hill, 2 edition, 2010.
- [68] M. Samimy and S. K. Lele. Motion of particles with inertia in a compressible free shear layer. *Physics of Fluids*, 3:1915, 1991.
- [69] A. Melling. Tracer particles and seeding for particle image velocimetry. *Measurement Science and Technology*, 8:1406–1416, 1997.
- [70] A. Krothapalli, E. Rajkuperan, F. Alvi, and L. Lourenco. Flow field and noise characteristics of a supersonic impinging jet. *Journal of Fluid Mechanics*, 392:155–181, 1999.
- [71] J. Kompenhans, A. Arnott, A. Agocs, A. Gilliot, and J. C. Monnier. Application of particle image velocimetry for the investigation of high speed flow fields. *West East High Speed Flow Fields*, 2002.
- [72] R. A. Humble, F. Scarano, and B. W. von Oudheusden. Particle image velocimetry measurements of a shock wave/turbulent boundary layer interaction. *Experiments in Fluids*, 43:173–183, 2007.

- [73] A. Lecuona, P. A. Sosa, P. A. Rodriguez, and R. I Zequeira. Volumetric characterization of dispersed two-phase flows by digital image analysis. *Measurement Science and Technology*, 11:1152–1161, 2000.
- [74] A. P. Boresi and R. J. Schmidt. *Advanced Mechanics of Materials*. Wiley, 6th edition, 2003.
- [75] F. P. Beer, E. R. Johnston Jr., J. T. DeWolf, and D. F. Mazurek. *Mechanics of Materials*. McGraw Hill, 5th edition, 2006.
- [76] J. R. Barber. *Intermediate Mechanics of Materials*. Springer, 2011.
- [77] N. E. Dowling. *Mechanical Behavior of Materials*. Prentice Hall, 3rd edition, 2006.
- [78] F. A. Mier, M. J. Hargather, and S. R. Ferreira. Experimental quantification of vent mechanism flow parameters in 18650 format lithium ion batteries. *Journal of Fluids Engineering*, 2019.
- [79] AZoM. A3 tool steel (UNS T30103) - air-hardening, medium-alloy, cold-work steels) - air-hardening, medium-alloy, cold-work steelst30103) - air-hardening, medium-alloy, cold-work steels.
- [80] AZoM. A2 tool steel (UNS T30102) - air-hardening, medium-alloy, cold-work steels.
- [81] Strain gage thermal output and gage factor variation with temperature. Technical Report TN504, VPG Micromasurements, 2014.
- [82] F. F. Hines. In *Proceedings, Western Regional Strain Gage Committee*, pages 39–44, 1960.
- [83] Errors due to transverse sensitivity in strain gages. Technical Report TN509TN5, VPG Micromasurements, 2011.
- [84] Strain gauge measurement - a tutorial. Technical Report Application Note 78, National Instruments, 1998.
- [85] J. R. Taylor. *An introduction to error analysis*. University Science Books, 1997.
- [86] M. Mahendran. The modulus of elasticity of steel - is it 200 GPa? In *International Specialty Conference on Cold-Formed Steel Structures*, 1996.
- [87] Engineering ToolBox. Poisson’s ratio.
- [88] E. Lemmon. Reference fluid thermodynamic and transport properties database (REFPROP). Technical report, NIST.
- [89] G.S. Settles. *Schlieren and Shadowgraph Techniques*. Springer Berlin Heidelberg, 1st edition, 2001.

- [90] JEFFSOL alkylene carbonates. Technical report, Huntsman Corporation, 2001.
- [91] Sucrose conversion table. Technical Report 135-A-50, Agricultural Marketing Service, Fruit and Vegetable Division, USDA, 1981.
- [92] J. F. Swindells, C. F. Snyder, R. C Hardy, and P. E. Golden. Viscosities of sucrose solutions at various temperatures: Tables of recalculated values. Technical Report NBS Circular 440, National Bureau of Standards, 1958.
- [93] G.S. Settles and M. J. Hargather. A review of recent developments in schlieren and shadowgraph techniques. *Measurement Science and Technology*, 28(042001), 2017.
- [94] Pressure regulator flow curves. Technical Report MS-06-114, Swagelok Company, 2017.
- [95] Model 9306A six-jet atomizer instruction manual. Technical report, TSI Incorporated, 2003.
- [96] A. Sciacchitano, D. R. Neal, B. L. Smith, S. O. Warner, P. P. Vlachos, B. Wieneke, and F. Scarano. Collaborative framework for PIV uncertainty quantification: comparative assessment of methods. *Measurement Science and Technology*, 26(074004), 2015.
- [97] W. Bernhard. Piv uncertainty quantification from correlation statistics. *Measurement Science and Technology*, 26(074002), 2015.
- [98] A. Sciacchitano and B. Wieneke. PIV uncertainty propagation. *Measurement Science and Technology*, 27(084006), 2016.
- [99] E. B. Gordon and Greber I. The entrainment rate for a row of turbulent jets. Technical Report Contractor Report 185278, Case Western Reserve University and NASA Lewis Research Center, 1990.

FLUID DYNAMICS OF LITHIUM ION BATTERY VENTING FAILURES

by

FRANK AUSTIN MIER

Permission to make digital or hard copies of all or part of this work for personal or classroom use is granted without fee provided that copies are not made or distributed for profit or commercial advantage and that copies bear this notice and the full citation on the last page. To copy otherwise, to republish, to post on servers or to redistribute to lists, requires prior specific permission and may require a fee.

